

Optical Spectroscopy of an Erbium-Doped Crystal

Optische Spektroskopie
eines Erbium-dotierten Kristalls

Diploma Thesis of

Daniel Rieger

Fakultät für Physik
Physikalisches Institut (PI)
Karlsruher Institut für Technologie (KIT)

Reviewer:	Prof. Dr. A. V. Ustinov
Second reviewer:	Prof. Dr. M. Wegener
Advisor:	Prof. Dr. P. A. Bushev
Second advisor:	Dr. W. Pernice

05. November 2012 – 04. November 2013

God does not play dice with the universe;

He plays an ineffable game of his own devising,
which might be compared, from the perspective of
any of the other players, to being involved in an
obscure and complex version of poker
in a pitch dark room,
with blank cards,
for infinite stakes,
with a dealer who won't tell you the rules, and
who smiles all the time.

Sir Terry Pratchett

Erklärung

Ich versichere wahrheitsgemäß, die Arbeit selbstständig angefertigt, keine anderen als die angegebenen Quellen und Hilfsmittel benutzt zu haben, die wörtlich oder inhaltlich übernommenen Stellen als solche kenntlich gemacht zu haben und die Satzung des Karlsruher Instituts für Technologie (KIT) zur Sicherung guter wissenschaftlicher Praxis beachtet zu haben.

Karlsruhe, den 04. November 2013

.....
(Daniel Rieger)

Contents

Abstract	1
Zusammenfassung	3
1 Introduction	7
2 Theory	9
2.1 Rare Earth Doped Crystals	9
2.1.1 Energy Level Structure	9
2.1.2 $\text{Er}^{3+}:\text{Y}_2\text{SiO}_5$	10
2.1.3 Homogeneous and Inhomogeneous Broadening	11
2.1.4 The Milli-Kelvin Regime	13
2.1.5 The Zeeman Effect	14
2.2 Time Resolved Spectroscopy	16
2.2.1 Two Level Systems	17
2.2.2 Interaction of an External Field with a TLS	18
2.2.3 T_2 , T_2^* and 2PE	19
2.2.4 T_1 and 3PE	23
3 Experimental Setup	27
3.1 Optical Setup and Experimental Procedures	27
3.1.1 Zeeman Splitting	27
3.1.2 Photon Echo	30
3.1.3 Integrated Solution	34
3.2 Integrated Optics	35
3.2.1 Substrate	35
3.2.2 Mode Simulation	36
3.2.3 Design	36
3.2.4 Fabrication	37
3.2.5 Measuring the Devices	39
3.2.6 Grating Coupler	40
3.2.7 Parameter Optimization	41
3.2.8 Ring Resonators	43
3.2.9 Evanescent Field Coupling	45
3.2.10 Gluing Single Fibers onto the Chip	46
3.2.11 Gluing a Fiber Array onto the Chip	47
3.2.12 Sample Holder	48

4	Results, Evaluation & Discussion	51
4.1	Zeeman Splitting	51
4.1.1	Crystallographic Site 1 (1536.48 nm)	51
4.1.2	Crystallographic Site 2 (1538.90 nm)	55
4.2	Photon Echo	58
4.2.1	T_1 at 25 mK	58
4.2.2	T_2 at 25 mK	61
4.2.3	Oscillations in the T_2 Dephasing at 25 mK	62
4.2.4	T_1 versus Temperature	64
4.2.5	T_2 versus Temperature	65
5	Summary	69
6	Conclusions	71
	Bibliography	73

Abstract

Quantum computation can only be effectively used in collaboration with long distance quantum networks which makes a coherent quantum converter between microwave and near-infrared photons necessary. This thesis covers the measurements of the optical decoherence times and the Zeeman splitting in Y_2SiO_5 , which could be used as such a quantum converter. We found the g-factors for the first magnetic subclass to be $g_{ground} = 1.79$, $g_{excited} = 0.69$ for the crystallographic site 1 (1536.48 nm) and $g_{ground} = 1.13$, $g_{excited} = 0.57$ for site 2 (1538.90 nm). At 25 mK and 280 mT the decoherence times, as measured by photon echo, are $T_1 = 0.836$ ms, $T_2 = 12.10$ μ s for site 1 and $T_1 = 0.755$ ms, $T_2 = 8.71$ μ s for site 2, hence limiting the pulse sequence time for coherent conversion. These decoherence times decrease for higher temperatures and start to drop very fast at around 600 mK for T_1 due to phonon coupling. T_2 at low temperatures is limited by spin-spin interaction while for higher temperatures it is T_1 -limited. Hence, it starts to drop quickly at 3 K. We also attempt an integrated solution with an on-chip waveguide in Si_3N_4 on which the crystal is placed. The coupling to the integrated waveguide is a challenge that could not be satisfactorily solved up to now.

Zusammenfassung

Quantencomputer sind derzeit ein äußerst beliebtes Forschungsfeld auf der ganzen Welt. Mit dieser Technologie wäre es möglich die Eigenschaften eines quantenmechanischen Zwei-Niveau-Systems auszunutzen, nämlich dass ein solches System jeglichen Überlagerungszustand der zwei reinen Zustände annehmen kann. Dies bringt erhebliche Vorteile bezüglich Rechengeschwindigkeit mit sich, insbesondere bei Algorithmen wie Datenbanksuche und Faktorisierung ganzer Zahlen. Außerdem erlaubt es die Simulation von quantenmechanischen Vielteilchensystemen, was bisher an der Rechenleistung von klassischen Systemen scheitert.

Jedoch kann solch eine Technologie nur in Verbindung mit einem Quantennetzwerk effektiv genutzt werden, das in der Lage ist einen Zwei-Niveau-Quantenzustand über weite Strecken zu übertragen. Dabei funktionieren die meisten Ansätze zum Bau eines Quantencomputers mithilfe von sogenannten Qubits als Zwei-Niveau-Systemen, die über Mikrowellen angesprochen werden. Mikrowellen eignen sich nicht zur langreichweitigen Übertragung in Glasfaserkabeln aufgrund der hohen Verluste. Stattdessen wäre eine solche Kommunikation mit Nahinfrarotphotonen wünschenswert, da diese deutlich weniger Verluste erleiden. Dennoch sind sogenannte Quantenwiederholer nötig, die ein Photon im infraroten Bereich kopieren können und somit die Reichweite erhöhen würden. Zusätzlich ist ein kohärenter Quantenwandler erforderlich, der Photonen vom Mikrowellenbereich in den nahinfraroten Bereich und umgekehrt übertragen kann und dabei die Quantenzustände erhält. Einen Quantenwandler zu entwickeln ist die Motivation für diese Arbeit.

Für einen solchen Quantenwandler ist ein physikalisches System, das an beide Energiebereiche koppelt, notwendig. Ein mit Erbium dotierter Kristall ist eine mögliche Lösung hierfür, da der erste Elektronenübergang von Erbium im nahinfraroten Bereich liegt. Durch Anlegen eines Magnetfeldes wird eine Aufspaltung der einzelnen Elektronenenergieniveaus erreicht. Je nach Stärke des Feldes kann das Grundniveau dann auf eine beliebige Mikrowellenfrequenz eingestellt werden.

Als Grundkristall für die Erbiumdotierung verwenden wir Y_2SiO_5 , da es nur sehr schwach mit Erbium interagiert und deshalb sehr hohe Kohärenzzeiten und sehr kleine Linienbreiten zur Folge hat. Es gibt in diesem Kristallgitter zwei verschiedene Stellen (sites) an denen sich das Yttrium befindet, welches durch Erbium ersetzt werden kann. An der einen Stelle hat das Yttriumatom sieben Sauerstoffatome als Nachbarn während es an der anderen Stelle nur sechs hat. Dies hat verschiedene Elektronenübergangsenergien zur Folge, 1536.48 nm an der ersten und 1538.90 nm an der zweiten Stelle. Außerdem gibt es zwei verschiedene magnetische Klassen, die

von der Orientierung abhängen. Das bedeutet, dass wir für jede Kristallstelle acht optische Übergänge erwarten können, falls wir annehmen, dass die g -Faktoren für das Grund- und das erste angeregte Niveau voneinander verschieden sind.

Um diese Übergänge zu messen verwenden wir einen nahinfraroten Diodenlaser von Toptica dessen Frequenz mithilfe eines Piezoelements über die Übergangsfrequenz gefahren wird. Mit einer Linse können wir den Strahl in eine Faser einkoppeln und an den optischen Tisch am Kryostat leiten. Dort wird der Strahl dann durch die optischen Fenster im Kryostat auf den in einem Probenhalter angebrachten Kristall fokussiert. Hinterher messen wir das Signal mit einer Photodiode. Der Kryostat hat eine Basistemperatur von etwa 25 mK. Dies ist nötig um die Bevölkerung der höheren Energieniveaus sehr klein zu halten und die Kohärenzzeiten zu verlängern.

Für die erste Kristallstelle sehen wir sechs optische Übergänge. Das reicht um wenigstens die g -Faktoren von einer magnetischen Klasse zu bestimmen. Diese sind $g_{\text{grund}} = 1.79 \pm 0.20$ und $g_{\text{angeregt}} = 0.69 \pm 0.08$. Für die andere Kristallstelle sehen wir sieben Übergänge und bekommen $g_{\text{grund}} = 1.13 \pm 0.13$ und $g_{\text{angeregt}} = 0.57 \pm 0.06$. Die Fehler stammen hauptsächlich von dem ungenau bekannten Frequenzbereich und der abgeschätzten Magnetfeldstärke.

Als nächstes ist es notwendig die Kohärenzzeiten T_1 und T_2 für den Kristall zu bestimmen. Dies kann durch die Anregung von sogenannten Photonenechos realisiert werden. Die Intensitätsamplitude dieser Lichtpulse hängt von der jeweiligen Wartezeit bzw. der Verzögerungszeit bei 3PE und 2PE Pulssequenzen ab. Man erhält dann einen exponentiellen Abfall und kann eine Ausgleichsfunktion durch die Messdaten legen. Diese Methode wird auch bei Elektronenspins und Kernspins angewandt, z.B. bei der Kernspintomographie. Um diese Messungen durchzuführen verwenden wir akustooptische Modulatoren zur Erzeugung der Lichtpulse.

Bei 25 mK und 280 mT erhalten wir folgende Ergebnisse für die Kohärenzzeiten. Für die erste Kristallstelle ergibt sich $T_1 = 0.836 \text{ ms} \pm 0.096 \text{ ms} \pm 0.043 \text{ ms}$ und $T_2 = 12.10 \text{ } \mu\text{s} \pm 1.38 \text{ } \mu\text{s} \pm 0.44 \text{ } \mu\text{s}$ während wir für die zweite Stelle $T_1 = 0.755 \text{ ms} \pm 0.052 \text{ ms} \pm 0.041 \text{ ms}$ und $T_2 = 8.71 \text{ } \mu\text{s} \pm 0.38 \text{ } \mu\text{s} \pm 0.31 \text{ } \mu\text{s}$ erhalten. Wir stellen fest, dass es bei der ersten Stelle für T_2 starke Oszillationen im exponentiellen Abfall gibt, die sich auf die Kopplung zu den Kernspins von benachbarten Yttrium- und Sauerstoffatomen zurückführen lassen. Die stärksten Frequenzen liegen bei 152 kHz, 271 kHz und 372 kHz. Für höhere Temperaturen nehmen die Kohärenzzeiten ab. T_1 erleidet zusätzlich einen sehr starken Abfall ab etwa 600 mK aufgrund von einsetzender Kopplung an Phononen. T_2 ist zunächst durch Spin-Spin Kopplung begrenzt und fällt dann ab etwa 3 K wegen der T_1 -Begrenzung ab. Die Quantenumwandlung muss innerhalb dieser Kohärenzzeiten erfolgen, damit die Erhaltung des Quantenzustandes gewährleistet ist. Das heißt es wäre unter Umständen möglich bei bis zu 3 K zu arbeiten.

Zusätzlich möchten wir noch eine integrierte Lösung für die optische Kopplung an den Erbiumkristall demonstrieren. Hierzu stellen wir einen optischen Wellenleiter in der Si_3N_4 Schicht eines siliziumbasierten Chips her. Der positive Photoresist ZEP 520A wird mithilfe eines Spincoaters auf den Chip aufgetragen. Der Wellenleiter wird durch Elektronenstrahlolithographie in den Photoresist geschrieben und mit Xylen en-

twickelt. Der Photoresist dient nun als Ätzmaske für reaktives Ionenätzen mit SF_6 und O_2 . Die Kopplung an diesen Wellenleiter erfolgt durch Gitterkoppler, die wie Bragggitter funktionieren. Die optimale Ausrichtung der Fasern auf diese Koppler erfolgt durch das Aufkleben eines Faserfelds auf den Chip. Die Transmission am morgen nach dem Aufkleben war $T = 2.5 \cdot 10^{-5}$.

Leider ist der Kleber anscheinend noch weiter gekrochen. Das Faserfeld hat sich also etwas verschoben und es ist keine Transmission durch den integrierten Wellenleiter mehr messbar. Wir werden das Kleben nochmal versuchen, allersings wird dies nicht rechtzeitig gelingen, um in dieser Arbeit noch darüber zu berichten.

Als nächster Schritt ist die Kopplung zwischen dem Mikrowellen- und dem nahinfraroten Bereich im Kristall vorgesehen. Für einen kohärenten Quantenwandler müssen wir in der Lage sein ein Mikrowellenphoton in einem bekannten Quantenzustand zu präparieren. Nach der Umwandlung müssen wir diesen Zustand am Infrarotphoton messen können. Hierfür ist eine Umwandlungspulssequenz zu entwickeln sowie eine effektive Emission des Infrarotphotons zu gewährleisten. Ein atomarer Frequenzkamm könnte dabei eine wichtige Rolle spielen. Letztlich wäre es wünschenswert einen integrierten Quantenwandler herzustellen, der neben dem optischen Wellenleiter auch einen supraleitenden Mikrowellenresonator auf dem Chip enthält. Dabei muss das Modenvolumen der Mikrowellen sowie des nahinfraroten Lichts im Kristall übereinstimmen, damit immer dieselben Erbiumatome angeregt werden.

Auch wenn es noch ein weiter Weg ist wäre es durchaus denkbar, dass in den nächsten Jahren wichtige Fortschritte auf diesem Feld erzielt werden, die den Bau des ersten echten Quantencomputers ermöglichen. Dies könnte eine neue Generation an Computertechnologie ermöglichen, deren Potential enorm ist und ungeahnte Anwendungen bietet.

1 | Introduction

Classical computers are based on bits with two states, 0 and 1, as their fundamental information units. Quantum computation, in contrast, aims to exploit the fact that a quantum mechanical two level system (TLS) can take any superposition state of the two pure eigenstates [40, 20, 12]. This yields a massive advantage in terms of computation velocity for many applications such as integer factorization (Shor-algorithm, [52, 31]) and the search of large databases (Grover-algorithm, [2, 30]). It also opens up new possibilities for quantum simulation of many-body objects [20]. Unfortunately, the decoherence times of these quantum states make the construction of a quantum computer rather challenging.

A significant constraint for many systems is the need to operate at low temperatures to permit manipulations of the quantum states within the time scale of the coherence times in the first place. Major issues persist in interfacing several qubits, which are used as processing unit, to save and emit microwave (MW) photons [48, 39]. Moreover, new software algorithms need to be developed which can actually make use of this new fundamental physical computation system.

Quantum networks and communication constitute another impressive application of quantum physics. It provides a level of intrinsic security unheard of in classical communication [21]. However, to efficiently interface quantum computers it is necessary to transfer quantum information over long distances which is very inefficient in the MW regime due to transmission losses. Near-infrared (NIR) photons, already widely-used in classical fiber communication, provide a much superior framework. Although, for long distances a quantum repeater which can replicate the quantum state of a NIR photon is still required [13, 9]. Furthermore, a way to convert the quantum state from the MW regime to the NIR regime and vice versa needs to be provided [8, 35, 44]. Developing the hardware of such a quantum converter is the motivation of this thesis.

A system used for quantum conversion has to be able to couple to MW as well as NIR photons. Additionally, a conversion mechanism and a way to retrieve the converted quantum state must be implemented. The rare earth element erbium, which is used as an amplifier in classical optical communication, is promising as a dopant because the electron transition of the ground state to the first excited state is in the NIR regime. The Zeeman splitting can be employed to tune the split ground levels to the MW frequency of choice. Yttrium orthosilicate is chosen as the host crystal due to its low coupling to the dopant which results in very high coherence times and extremely narrow linewidths [6, 3, 4, 5].

The motivation for the experiments presented in this thesis is to measure the optical electron transitions of the erbium-doped crystal at milli-Kelvin. This will provide information about the g-factors [49] of the ground and the excited state and serves as preparation for one of the most important steps in the development of Er:YSO as a quantum converter, namely to determine the optical coherence times of the quantum states. This can be done by applying a sequence of light pulses to trigger a photon echo [18, 5]. Since the intensity of this echo depends on the coherence times of the quantum states we can determine them and investigate their behavior at different temperatures and magnetic fields. This information is vital in designing a quantum converter and assessing the boundaries for the conversion mechanism, which needs to take place well within the coherence times in order to preserve the quantum state during the energy conversion [14].

In addition, we try to take a step towards an integrated solution. The potential future spread of this technology depends largely on its qualification for affordable mass production. Hence, we try to demonstrate coupling between the erbium-doped crystal and an integrated optical waveguide on a silicon based chip. The crystal is to be placed on top of that waveguide and light is transmitted through the waveguide. By means of evanescent wave coupling we should be able to excite the erbium atoms [16, 24].

The thesis is structured as follows. First, the theoretical basics of the crystal and the internal effects are explained. Then, the experimental setup is presented and we illustrate how the experiments were conducted. Subsequently, we turn our attention to the design and fabrication of the integrated waveguide, after which the results of the experiments and their evaluation are shown and discussed. Finally, the contents of this thesis are summarized and the conclusions as well as an outlook are provided.

2 | Theory

We start by introducing the fundamental physical effects that underlie the experiments presented in this thesis. First, the structure and properties of rare earth-doped crystals and the nature of the energy levels in erbium are accounted for. Then, we explain how these energy levels are affected by a magnetic field as well as homogeneous and inhomogeneous broadening. Furthermore, the interaction with electromagnetic waves is outlined and, lastly, the excitation of photon echoes, which are essential in measuring the life times of quantum states in erbium, is covered. These effects are crucial to eventually conduct coherent quantum state conversion.

2.1 Rare Earth Doped Crystals

Rare earth elements are a special group of elements in the periodic table. They consist of the 15 lanthanides plus scandium and yttrium [6]. The interesting feature of these elements is the fact that their triply-ionized ions have a partially filled 4f shell which is very well shielded by the surrounding 5s² and 5p⁶ electron shells. The resulting inner-shell 4f-4f transitions have very narrow line widths spanning a spectrum from the far infrared to the ultraviolet [23]. When doped into a host crystal, the shielding remains effective and the crystal field of the host is merely a weak perturbation of the free ion levels.

2.1.1 Energy Level Structure

The Er³⁺ energy levels arise from the odd-numbered 4f¹¹ electron configuration with a ⁴I term [8]. It is split into fine structure levels by spin-orbit coupling as depicted in figure 2.1. For our laser spectroscopy experiments it is convenient to use a simple two-level system model, where the energy levels ⁴I_{15/2} and ⁴I_{13/2} serve as the ground state and excited state, respectively [6]. The optical transition from the ground state ^{2S+1}L_J = ⁴I_{15/2} to the excited state ⁴I_{13/2} happens around the C-band telecom frequency (1550 nm \approx 195 THz). The free erbium ion with the angular momenta J and M_J has $2J + 1$ fold degenerate energy levels. When introduced into a crystal, the shielded crystal field symmetry causes a partial lifting of the $2J + 1$ fold M_J degeneracy. This results in the ground state ⁴I_{15/2} being split into eight ($J + 1/2$) Kramers doublets and the excited state ⁴I_{13/2} being split into seven such doublets [25, 14].

As we conduct our experiments in the milli-Kelvin regime, it is fine to assume that any excited states are very lowly populated (2.1.4). The degeneracy of the Kramers doublets can be lifted by applying an external magnetic field. This is called Zeeman splitting. Due to the g-factors, the strengths of these Zeeman interactions are

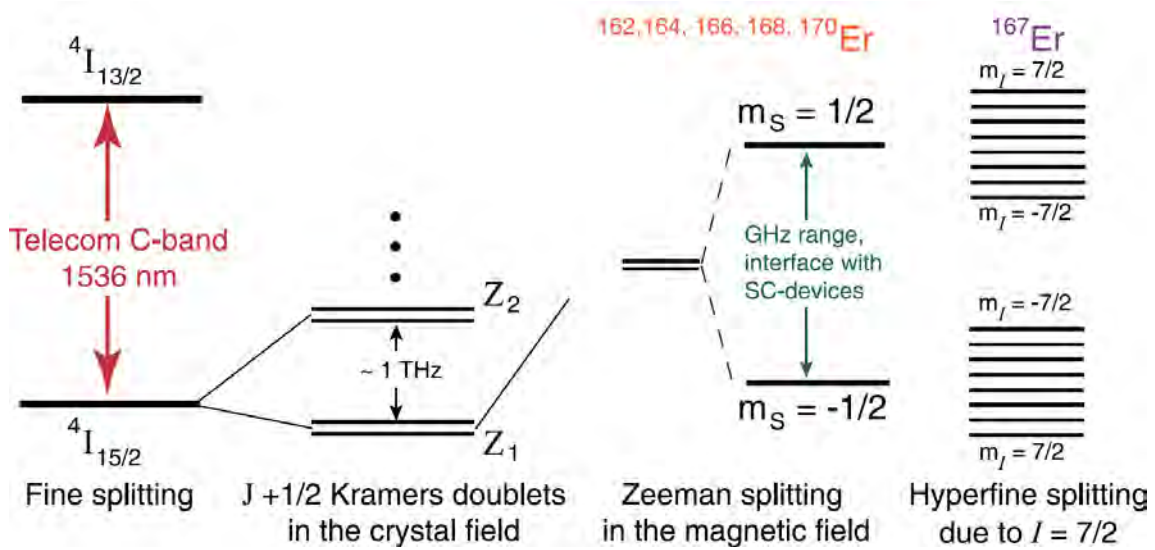


Figure 2.1: The structure of the energy levels of Er^{3+} ions in YSO. S, L and J correspond to spin, orbital and total magnetic momentum of the ion, respectively. At milli-Kelvin only the lowest of the $(J+1/2)$ Kramers doublets is highly populated and their degeneracy can be lifted by an external magnetic field which gives rise to a Zeeman splitting. For the odd isotope ^{167}Er each Zeeman level is furthermore split into 8 hyperfine levels. (Image from [8].)

different for the ground and the excited state. Consequentially, we can model such an erbium-doped crystal in a magnetic field at milli-Kelvin by a four-level structure consisting of two Zeeman levels in the ground state and two in the excited state. Moreover, there are four optical transitions as the Zeeman levels in the ground and the excited state are not equidistant.

Yet another predicate of this material is readily explained by taking into account that erbium has five even isotopes: ^{162}Er , ^{164}Er , ^{166}Er , ^{168}Er , ^{170}Er ; and one odd isotope: ^{167}Er with $I = 7/2$ [8]. Thus, the electronic states of ^{167}Er are split into eight hyperfine levels which correspond to the spin-spin interactions between the electrons and nucleons. The spin projection in the direction of the field, typically defined as the z direction, is given by $m_S = \pm 1/2$.

2.1.2 $\text{Er}^{3+}:\text{Y}_2\text{SiO}_5$

The host crystal of choice is yttrium orthosilicate due to the very narrow linewidths when doped with a rare earth element and because the cross sections of the absorption spectra are rather large. It also has the highest magnetic anisotropy. It is a monoclinic biaxial crystal belonging to the C_{2h}^6 space group. Er^{3+} substitutes for the Y^{3+} ions which occupy two crystallographically nonequivalent sites of C_1 symmetry while the primitive cell of Y_2SiO_5 contains 16 Y^{3+} ions (see figure 2.2). Site 1 has seven oxygen atom neighbors whereas site 2 has only six of them. Hence, there are two different optical absorption lines corresponding to the transition $^4I_{15/2} \leftrightarrow ^4I_{13/2}$ with the vacuum resonance wavelengths 1536.48 nm and 1538.90 nm for site 1 and site 2, respectively, at zero magnetic field [3, 5].

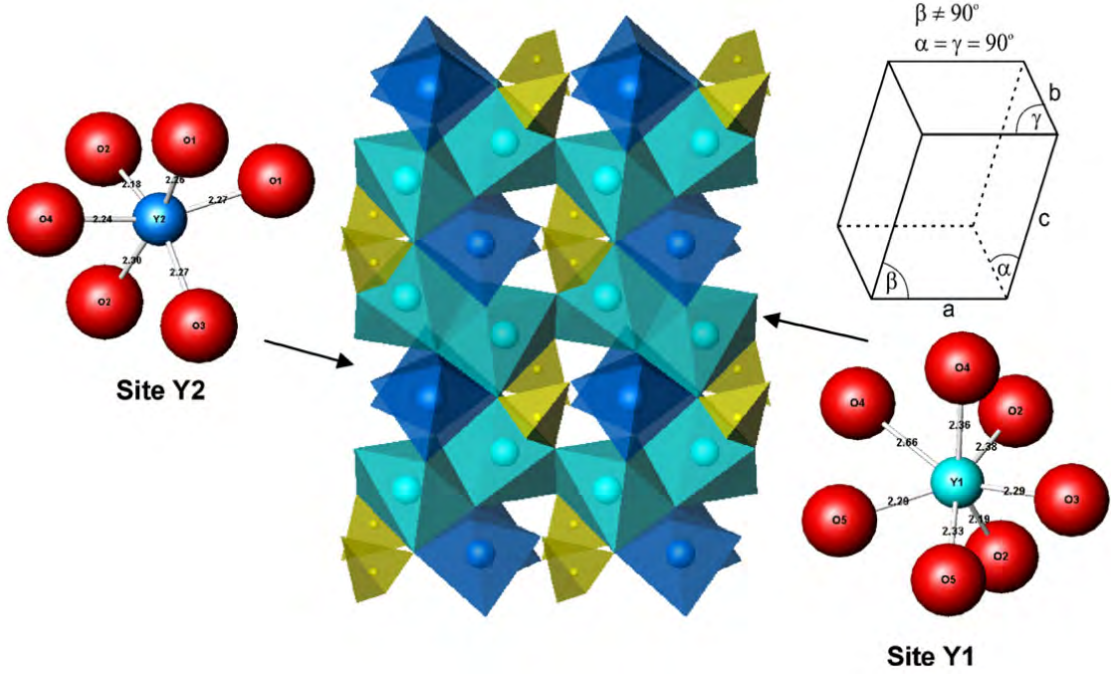


Figure 2.2: The crystalline structure of the host crystal Y_2SiO_5 contains two nonequivalent sites at which a Y^{3+} ion can be substituted for. Y^{3+} at Site 1 with a vacuum resonance wavelength of 1536.48 nm for the transition ${}^4I_{15/2} \leftrightarrow {}^4I_{13/2}$ is light blue and at Site 2 (1538.90 nm) it is dark blue. The silicon atoms are yellow and the oxygen atoms are at each node in between the other atoms. (Image from [17].)

The monoclinic cell of Y_2SiO_5 has the dimensions $a = 10.410 \text{ \AA}$, $b = 6.721 \text{ \AA}$, $c = 12.490 \text{ \AA}$ and $\beta = 102.39^\circ$ where β is the angle between a and c while the unit-cell volume is $V = 853.51 \text{ \AA}^3$ [5]. On top of the crystal axis a , b and c , the optical extinction axis D_1 and D_2 as well as the direction of the magnetic field need to be taken into account in order to describe the crystal properties (see figure 2.3). The relationship between the two sets of coordinates formed by a , b and c ; as well as D_1 , D_2 and b is important since clockwise and counterclockwise rotations around C_2 yield different results [49]. For each of the two crystallographic sites mentioned above we have four subclasses of different orientations that can be obtained by rotation and inversion in C_2 . The two classes related by inversion respond identically to a magnetic field in any direction, however, the ones connected via rotation do not, they are magnetically nonequivalent.

Due to these nonequivalent orientations, we generally expect to see twice as many transitions in both crystallographic sites when applying a magnetic field giving rise to a Zeeman splitting. This means, we should see eight optical transitions for each site, four for each magnetic orientation. In special cases, i.e., if the magnetic field is parallel to the b axis or in the D_1 - D_2 plane, these subclasses are degenerate [49].

2.1.3 Homogeneous and Inhomogeneous Broadening

The emission spectrum of a certain transition in a crystal is never infinitely narrow. Instead, it is broadened by a number of physical effects which can be divided into homogeneous and inhomogeneous broadening. Homogeneous broadening includes

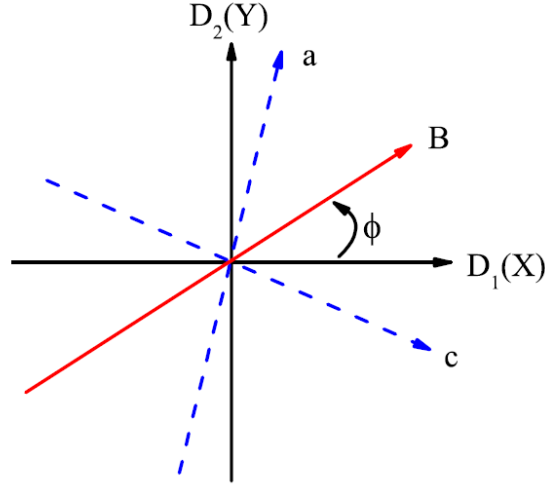


Figure 2.3: Crystal symmetry of Y_2SiO_5 . B is the magnetic field, D_1 and D_2 are the optical extinction axis and a and c correspond to the unit-cell while b points out of the page. (Image from [49].)

everything that affects all atoms in the same manner and is governed by dynamical processes which act as perturbations on the ion's resonance frequency or phase. Effects which are not equally experienced by all atoms are called inhomogeneous broadening. Even a resting atom which is not interacting at all with its environment has a linewidth which deviates from a delta function. This is called natural linewidth and is a consequence of the Heisenberg uncertainty principle:

$$\Delta E \cdot \Delta t \geq \frac{\hbar}{2} \quad (2.1)$$

Classically, this effect is described by the Fourier transform limit $\Delta\omega \cdot \Delta t = 1/2$ and means the same thing.

The *homogeneous linewidth* of Er^{3+} -doped crystals can be described as the sum of the individual contributions and has a Lorentzian profile [6]:

$$\Gamma_{hom} = \Gamma_{pop} + \Gamma_{Er-Er} + \Gamma_{Phonon} + \Gamma_{Er-Host} + \Gamma_{ISD} \quad (2.2)$$

These contributions shall be briefly explained here:

- Γ_{pop} corresponds to the excited state population lifetime T_1 :

$$\Gamma_{pop} = \frac{1}{2\pi T_1} \quad (2.3)$$

- Some erbium ions are subject to phonon-induced spin-flip resulting in the modulation of the energy levels (Γ_{Er-Er}). These contributions are highly dependent on the Er^{3+} -ion concentration.
- Γ_{Phonon} describes dephasing from temperature-dependent phonon scattering. The cryogenic temperature ensures that only indirect phonon processes contribute here.
- The interaction of the ion with the nuclear and electronic spin of the host lattice is included in $\Gamma_{Er-Host}$.

- Γ_{ISD} accounts for an effect called instantaneous spectral diffusion (ISD), which relates to changes in the local environment caused by the optical excitation of nearby atoms. It can be controlled by reducing the doping concentration.

All in all, the homogeneous linewidth of $\text{Er}^{3+}:\text{Y}_2\text{SiO}_5$ can be as tremendously narrow as 100 100 Hz [6]. This allows for very high lifetimes of the quantum states T_1 and T_2 (see sections 2.2.4 and 2.2.3).

In contrast, *Inhomogeneous broadening* is a result of variations of the crystal field due to local strain in the lattice as well as magnetic field inhomogeneity. They can be caused by crystal growth, impurities or lattice imperfections and dislocations as well as thermal motion of the atoms (thermal Doppler broadening) [6]. These local

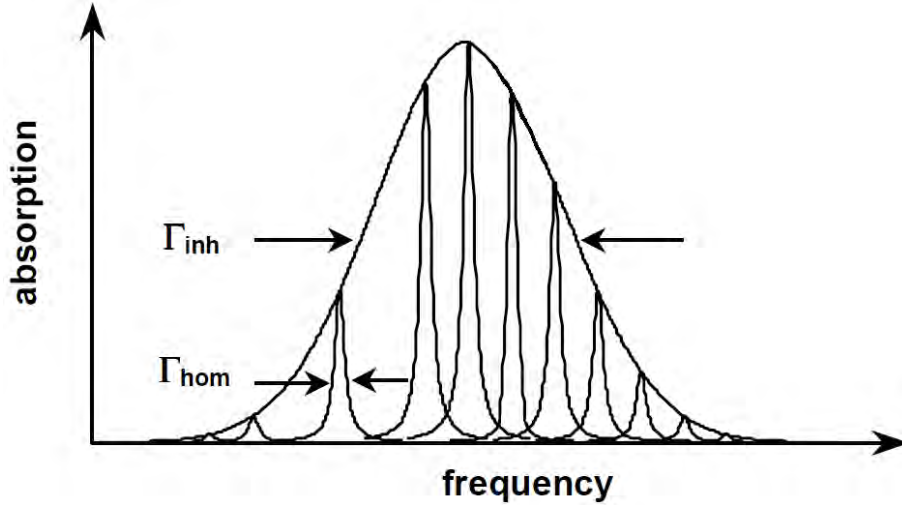


Figure 2.4: The optical transition of an erbium ion in a host lattice is subject to homogeneous broadening. Due to local variations of the crystal field the center frequencies of the individual ions are shifted. The overall shape combining many of these shifted linewidths is much broader. This is the inhomogeneous linewidth. (Image from [6].)

differences shift the center frequency of the homogeneous linewidths of the erbium ions. The combination of many of these shifted homogeneously broadened lines becomes a much broader, often Gaussian, frequency distribution called inhomogeneous linewidth Γ_{inh} (see figure 2.4). In the case that an inhomogeneous effect such as Doppler broadening occurs independently, the resulting linewidth has a Voigt profile which is the convolution of a Lorentz and a Gaussian profile. However, in our case thermal Doppler broadening is minimal due to the cryogenic temperatures.

2.1.4 The Milli-Kelvin Regime

The fact that our experiments are conducted at temperatures far below 1 K is important in several ways. The obvious and mandatory reason is to ensure that, in good approximation, only the lowest energy level is populated by the erbium electrons in the 4f shell. Otherwise it would not be possible to temporarily store the quantum state of a single incoming microwave photon and, after a series of pulses, emit a near-infrared photon in that same quantum state - or vice versa - which is eventually the goal of this project.

The population of an excited state is given by the Boltzmann distribution. In the case of a simple two level system the population distribution in thermodynamical equilibrium is given by

$$\frac{N_2}{N_1} = \exp\left(-\frac{\Delta E}{k_B T}\right) \quad (2.4)$$

where ΔE is the energy difference of those levels, k_B the Boltzmann constant and T the temperature. The energy gap due to the Zeeman splitting depends linearly on the applied magnetic field (section 2.1.5). This means, we can easily tune that gap to whatever frequency we need. As the resonance frequency of our on-chip microwave resonators is around 3.7 GHz we shall assume an energy difference of

$$\Delta E = h\nu \approx 6.626 \cdot 10^{-34} \text{ Js} \cdot 3.7 \text{ GHz} \approx 2.5 \cdot 10^{-24} \text{ J} \quad (2.5)$$

where h is the Planck constant. With $c = \lambda f$ the corresponding wavelength in vacuum is 8.1 cm (with the vacuum speed of light: $c \approx 3 \cdot 10^8$ m/s).

The base temperature of our dilution fridge LD-250 from Bluefors is around 25 mK. In thermal equilibrium, the relative population of the upper Zeeman level of the ground state is then given by

$$\frac{N_2}{N_1} \approx \exp\left(-\frac{2.5 \cdot 10^{-24} \text{ J}}{1.38 \cdot 10^{-23} \text{ J/K} \cdot 23 \text{ mK}}\right) \approx 0.038 \% \quad (2.6)$$

The energy gap between the Zeeman levels in the excited state is expected to be a little smaller. However, as the thermal excitation of the upper state is marginal we can neglect it for the timescale of the coherence times T_1 and T_2 (sections 2.2.4, 2.2.3).

Incidentally, there are a couple of side effects which prove convenient in the construction of such a quantum converter. Since only the lowest energy level is occupied we can argue that there is no population in any level other than the lowest Kramers doublet. Hence, the simplification of a 4-level system consisting of the lowest Kramers doublets of each the ground and the first excited state is valid. The energy gaps between the first excited state and higher states raised by fine splitting are nowhere near the telecom frequency and are therefore not affected by our laser field.

Such low temperatures also maximize the already high lifetimes, T_1 and T_2 , of the erbium states caused by the narrow linewidth and low doping concentrations. Essentially, this is relevant as it provides the time window to apply the pulses which transfer the quantum state in the crystal from the microwave to the optical regime or vice versa. The actual realization of such a conversion scheme is still the content of research and is not quite straight forward mainly due to inhomogeneous broadening [42].

2.1.5 The Zeeman Effect

The Zeeman effect has a major impact on the experiments presented in this thesis. We shall briefly derive it here. The Hamiltonian of an atom in a magnetic field is

$$H = H_0 + V_M = H_0 - \vec{\mu} \cdot \vec{B} \quad (2.7)$$

where $\vec{\mu} = -\mu_B g \vec{J} / \hbar$ is the magnetic moment of the atom. We neglect the nuclear part here. $\mu_B = q\hbar/(2m)$ is the Bohr magneton, $\vec{J} = \vec{L} + \vec{S}$ is the total electronic angular momentum. \vec{L} and \vec{S} are the orbit angular momentum and the spin angular momentum, respectively. g is the Landé g-factor.

The magnetic moment can be written as

$$\vec{\mu} = -(g_l \vec{L} + g_s \vec{S}) \frac{\mu_B}{\hbar} \quad (2.8)$$

The respective Landé factors for the orbital angular momentum and the spin angular momentum are $g_l = 1$ and $g_s \approx 2.00232$. The deviation of g_s from the value 2 can be explained by quantum electrodynamics and is caused by vacuum fluctuations.

In our case the magnetic potential V_M is small and the level splitting due to the magnetic field is much less than the fine structure splitting which happens as a result of the LS (orbit-spin) coupling. We can thus treat V_M as a weak perturbation of H_0 which results in the linear Zeeman effect. For larger magnetic fields the LS

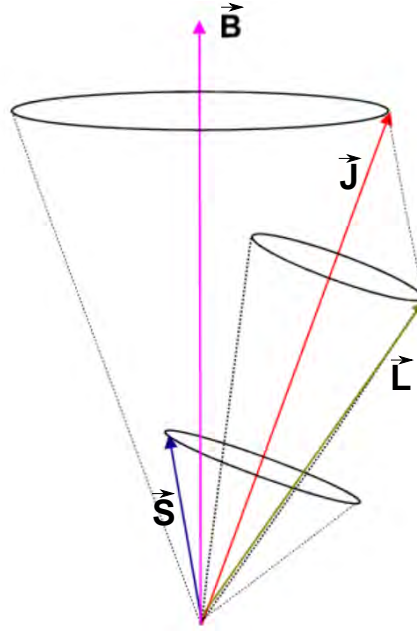


Figure 2.5: When a weak magnetic field is applied to an atom with one electron in the outer shell, the total angular momentum $\vec{J} = \vec{L} + \vec{S}$ is precessing around the field direction with the Larmor frequency due to the magnetic moment. \vec{L} & \vec{S} (orbit and spin angular momentum) are precessing around \vec{J} .

coupling may be far exceeded by the magnetic level splitting which is then called Paschen-Back effect. For ultrastrong fields, where the magnetic interaction exceeds even H_0 , one talks about Landau levels instead.

For the Zeeman effect (weak magnetic fields) \vec{L} and \vec{S} are not separately conserved, only $\vec{J} = \vec{L} + \vec{S}$ is. \vec{L} and \vec{S} are precessing around \vec{J} and \vec{J} is precessing around \vec{B} (figure 2.5) due to the magnetic moment

$$\vec{\mu}_{total} = \vec{\mu}_j = \vec{\mu}_l + \vec{\mu}_s = \frac{\mu_B}{\hbar} (\vec{L} + g_s \vec{S}) \quad (2.9)$$

The angular velocity of the precession around \vec{B} is given by

$$\omega_L = \frac{g_j q}{2m} B = \frac{\Delta E}{\hbar} \quad (2.10)$$

and is called Larmor precession with q being the charge and m the mass of the electron.

In a stationary magnetic field it is sufficient to merely look at the projection of \vec{J} onto the $\vec{B} = (0, 0, B)^T$ direction J_z . Likewise we can use the projection of \vec{L} and \vec{S} as $L_z = m_l \hbar$ and $S_z = m_s \hbar$, respectively. m_l can take any integer value from $-l_z$ to $+l_z$ resulting in $2l_z + 1$ numbers of energy levels. The outer electron shell, or in our case the 4f shell, is always populated by either one effective electron or by none in regard to S_z . This is because the electron shells are filled in such a way that the spins along \hat{z} of an even number of electrons in one shell cancel each other out. For an odd number of electrons in the outer shell, which is the case for Er^{3+} , we obtain

$$S_z = \pm \frac{1}{2} \hbar \quad (2.11)$$

while for an even number we get $S_z = 0$ which is called normal Zeeman effect with $L_z = J_z$.

Generally, the energy level is split into $(2J + 1)$ levels with an energy difference of

$$\Delta E_{m_j, m_{j-1}} = g_j \mu_B B \quad (2.12)$$

which depends linearly on the magnetic field. The Landé factor g_j is then given by the Landé equation

$$g_j = \left(1 + \frac{j(j+1) + s(s+1) - l(l+1)}{2j(j+1)} \right) \quad (2.13)$$

Here, the abnormal Landé factor of the electron spin is not incorporated, instead the exact value of 2 is used.

In the specific level structure of $\text{Er}^{3+}:\text{Y}_2\text{SiO}_5$ each Kramers doublet is two fold degenerate due to the electron spin. A magnetic field lifts this degeneracy and each doublet splits into two levels due to the Zeeman effect. The difference in energy between these two levels is

$$\Delta E_{+\frac{1}{2}, -\frac{1}{2}} = g_j \mu_B B \quad (2.14)$$

with two different Landé factors for the ground and the excited state lowest Kramers doublet.

2.2 Time Resolved Spectroscopy

To conduct time dependent spectroscopy experiments one first needs a detailed understanding of a quantum two level system (TLS). When we understand how such a TLS can be manipulated by an external field, we can conduct a series of pulsed measurements that allow us to determine the lifetimes of the electron. This method is called photon echo. Incidentally, such pulses will eventually allow coherent quantum state conversion. Throughout this entire section we will use the Dirac notation of quantum states (with Bras $\langle \psi |$ and Kets $|\psi\rangle$) which is explained in any common textbook on quantum mechanics, e.g. [26, 45, 10].

2.2.1 Two Level Systems

A TLS is a quantum mechanical system that is described by a Hilbert space with two degrees of freedom. The complete basis spanning that space must therefore consist of two independent states. However, $\text{Er}^{3+}:\text{Y}_2\text{SiO}_5$ is approximately described by a four level system when a magnetic field is applied. But since we only excite one transition, we can assume that the TLS of this transition is isolated and does not interact with the other levels. We assume that the applied magnetic field is large enough to prevent thermal excitation from the lower ground state $|g \downarrow\rangle$ to the upper

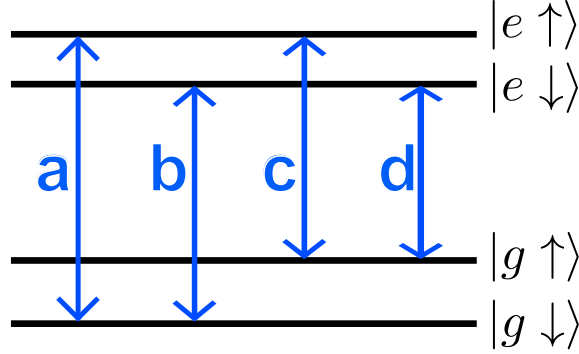


Figure 2.6: The effective four level structure of $\text{Er}^{3+}:\text{Y}_2\text{SiO}_5$ consisting of the two Zeeman split levels in the ground state $|g\rangle$ and those in the excited state $|e\rangle$.

ground state $|g \uparrow\rangle$ as well as from the lower excited state $|e \downarrow\rangle$ to the upper excited state $|e \uparrow\rangle$. Any two of those four levels, e.g. $|g \downarrow\rangle$ & $|e \downarrow\rangle$, can now be approximated by a TLS.

The state of the electron in the TLS is generally given by a superposition of the two eigenstates $|g \downarrow\rangle \hat{=} |1\rangle$ and $|e \downarrow\rangle \hat{=} |2\rangle$

$$|\psi(0)\rangle = c_1 |1\rangle + c_2 |2\rangle \quad c_1, c_2 \in \mathbb{C} \quad (2.15)$$

with $c_1^2 + c_2^2 = 1$ because the state is normalized. The time evolution of this state is given by the time dependent Schrödinger equation $H\psi = i\hbar\partial\psi/\partial t$. After the time t it will have evolved into

$$|\psi(t)\rangle = c_1 |1\rangle e^{-iE_1 t/\hbar} + c_2 |2\rangle e^{-iE_2 t/\hbar} \quad (2.16)$$

In the sub-Kelvin regime we can assume that $c_1 = 1$ and $c_2 = 0$ when the system is in thermal equilibrium (section 2.1.4). A convenient representation of the superposition of a TLS is a vector on a Bloch sphere. Each state corresponds to one point on the unit sphere. We pick the energy eigenstate $|1\rangle$ to sit at the south pole of the sphere with $\theta = \pi$ and the energy eigenstate $|2\rangle$ at the north pole with $\theta = 0$. The colatitude θ and the azimuth ϕ are determined by c_1 and c_2 (see figure 2.7). For each TLS there is a characteristic angular frequency around ϕ . This is the Larmor frequency as mentioned in section 2.1.5

$$\omega_L = \frac{|E_2 - E_1|}{\hbar} \quad (2.17)$$

It is also present in the transition ${}^4I_{15/2} = |g\rangle \leftrightarrow {}^4I_{13/2} = |e\rangle$ (see figure 2.6) with zero magnetic field because the difference of energy of the two levels will already

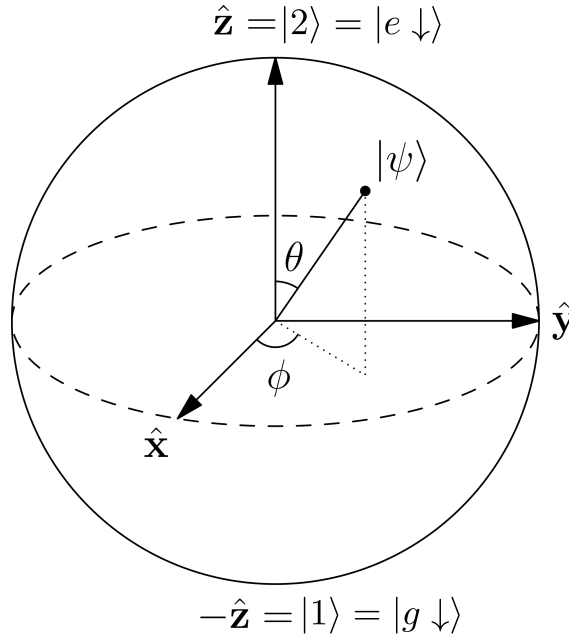


Figure 2.7: A two level system can be represented as a point on the unit Bloch sphere. The lower energy eigenstate is shown as $|1\rangle = -\hat{z}$ with the colatitude $\theta = \pi$ and the upper energy eigenstate is $|2\rangle = \hat{z}$ with $\theta = 0$. ϕ is the azimuth.

cause a precession due to the electric dipole moment.

An arbitrary TLS quantum state which is described by a point on the unity Bloch sphere is exactly equivalent to the phase (azimuth ϕ) and polarization (colatitude θ) of a photon. This is the reason coherent interaction between an oscillating electromagnetic field and a TLS is possible in the first place.

2.2.2 Interaction of an External Field with a TLS

Let us consider a static magnetic field $\vec{B} = B\hat{z}$ along the \hat{z} direction. In order to make the mathematical description more transparent, we consider an isolated electron as TLS with the two spin states, e.g. $|g \downarrow\rangle$ and $|g \uparrow\rangle$, as the two eigenstates. Then, the interaction Hamiltonian is $H = -\vec{\mu}\vec{B} = -\mu\vec{\sigma}\cdot\vec{B}$ where μ is the magnitude of the particle's magnetic moment and $\vec{\sigma}$ the vector of Pauli matrices. With the time dependent Schrödinger equation we obtain

$$|\psi(t)\rangle = e^{i\omega t\vec{\sigma}\cdot\hat{z}} |\psi(0)\rangle \quad (2.18)$$

where $\omega = \mu B/\hbar$ and $e^{i\omega t\vec{\sigma}\cdot\hat{z}} = \cos(\omega t)\mathbb{1} + i\hat{z}\cdot\vec{\sigma}\sin(\omega t)$.

This corresponds to the Bloch vector precessing around \hat{z} with the angular frequency $2\omega = \omega_L$. Moreover, it is

$$e^{i\omega t\vec{\sigma}\cdot\hat{z}} = \begin{pmatrix} e^{i\omega t} & 0 \\ 0 & e^{-i\omega t} \end{pmatrix} \quad (2.19)$$

The Bloch vector for a state vector $|\psi(0)\rangle$ is the vector of expectation values $\vec{R} = (\langle\sigma_x\rangle, \langle\sigma_y\rangle, \langle\sigma_z\rangle)$. Any normalized state vector $|\psi(0)\rangle$ can be written as a superposition of $|g \downarrow\rangle = |\downarrow\rangle$ and $|g \uparrow\rangle = |\uparrow\rangle$. In the σ_z basis we have for the specific case of

the colatitude $\theta = 90^\circ$

$$|\psi(0)\rangle = \frac{1}{\sqrt{2}} \begin{pmatrix} 1 \\ 1 \end{pmatrix} \quad (2.20)$$

The components of $|\psi(t)\rangle$ on the Bloch sphere are given by

$$\vec{R} = (\cos(2\omega t), -\sin(2\omega t), 0) \quad (2.21)$$

This vector begins pointing along \hat{x} at $t = 0$ and precesses around \hat{z} in a left handed manner.

Now consider a static magnetic field \vec{B}_0 in the \hat{z} direction and additionally, a weak transverse field \vec{B}_1 that oscillates at a frequency ω_r in the xy-plane. Then, the entire magnetic field is

$$\vec{B} = \vec{B}_0 + \vec{B}_1 = \begin{pmatrix} B_1 \cos(\omega_r t) \\ B_1 \sin(\omega_r t) \\ B_0 \end{pmatrix} \quad (2.22)$$

The interaction Hamiltonian is again $H = -\mu\vec{\sigma} \cdot \vec{B}$ and $|\psi(t)\rangle$ is the solution of the time dependent Schrödinger equation. After some calculation we get

$$\frac{\partial |\psi\rangle}{\partial t} = i \left(\omega_1 \sigma_x + \left(\omega_0 + \frac{\omega_r}{2} \right) \sigma_z \right) |\psi\rangle \quad (2.23)$$

with $\omega_0 = \mu B_0/\hbar$ and $\omega_1 = \mu B_1/\hbar$. The resulting Bloch vector is precessing around

$$\vec{R} = \begin{pmatrix} \omega_1 \\ 0 \\ \omega_0 + \omega_r/2 \end{pmatrix} \quad (2.24)$$

with a frequency that is twice the magnitude of the vector. The angular frequency of the rotating magnetic field can be chosen such that $\omega_r = -2\omega_0$. Hence, in the rotating frame of the \hat{z} precession, the state vector will also precess around \hat{x} (see figure 2.8). This means the electron is flipped from the lower state $|\downarrow\rangle$ to the upper one $|\uparrow\rangle$ and back. This is called a Rabi cycle. Unfortunately, we cannot detect the Rabi cycle in continuous wave mode in our setup because of the low intensity absorption. Limiting the oscillating field to a certain duration makes it possible to transfer the Bloch vector to any value of the colatitude θ . The vector is, of course, precessing around \hat{z} all along due to the static magnetic field \vec{B}_0 .

These considerations, are valid for all TLS enabling us to prepare the Bloch vector in any orientation by letting the TLS interact with the field of a particular direction and strength for a precise duration.

2.2.3 T_2 , T_2^* and 2PE

In a TLS there are several different processes which cause an excited state to fall back into the equilibrium state after some time. This is called decoherence. We divide these decoherence effects into two groups: processes causing depopulation parallel to the external magnetic field $\vec{B}_0 = B\hat{z}$ are called T_1 and dephasing processes perpendicular to that field are termed T_2 . We shall first concern ourselves with the T_2 relaxation.

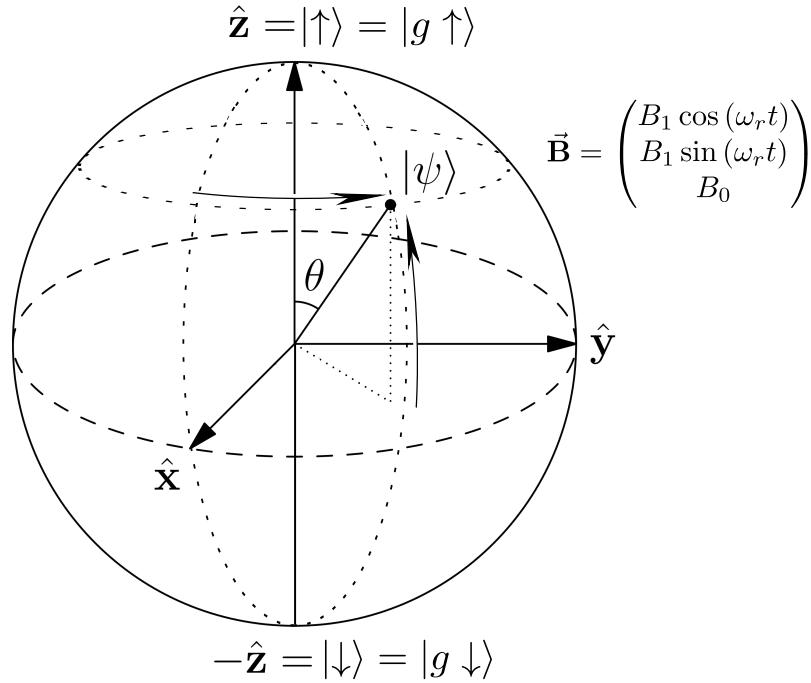


Figure 2.8: In a static magnetic field along \hat{z} the Bloch vector of a TLS will precess around that axes. When an additional transverse oscillating field is applied, it is possible to flip the state from $|\downarrow\rangle$ to $|\uparrow\rangle$ as the Bloch vector is also precessing around the \hat{x} axis.

There are several different effects that can cause a dephasing in the xy -plane. For example, homogeneous and inhomogeneous broadening as well as spectral diffusion [4]. Spectral diffusion refers to a time dependent modulation of the transition frequency which is caused by microscopic processes. It is important to note that spectral diffusion implies that the fluctuations are slow to effectively broaden the transition frequency. At least, they should be as large as the homogeneous linewidth. We distinguish between dephasing effects that are time dependent, referred to as T_2 , and such processes that are seemingly constant in time, called T_{inhom} as they are caused by inhomogeneous broadening.

The timescale of T_{inhom} is much slower than the decay rates, i.e. much slower than milliseconds, as it is caused by local variations of the crystal field. This means that the Larmor frequency of the Bloch vector varies for different locations in the crystal and these vectors dephase with time. However, the homogeneous linewidth and spectral diffusion cause fluctuations of the transition frequency, which leads to fluctuations in the Larmor frequency. These add up to the T_2 relaxation. The two dephasing processes combine to T_2^*

$$\frac{1}{T_2^*} = \frac{1}{T_2} + \frac{1}{T_{inhom}} \quad (2.25)$$

T_2 is usually much longer than T_2^* .

Now, it is possible to measure T_2 by applying a method called photon echo. As discussed in the previous section 2.2.2, we can modify the state of a TLS by gen-

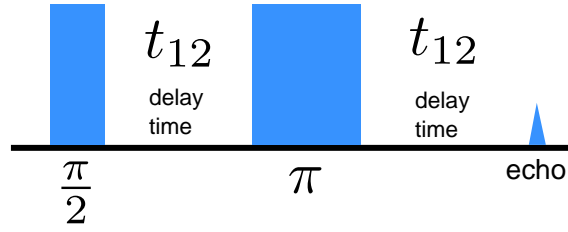


Figure 2.9: A $\pi/2$ -pulse excites the ensemble by 90° . It starts to dephase. After the delay time a π -pulse allows the ensemble to recover the T_{inhom} dephasing. The photon echo is emitted after another delay time t_{12} . By varying this time we can measure the decoherence time T_2 as it cannot be recovered due to its statistic nature.

erating a specific oscillating field transverse to the static magnetic field in the \hat{z} direction. If this is done for a certain time we can basically rotate the Bloch vector by an arbitrary colatitude angle θ . A pulse rotating the TLS by $\theta = 180^\circ$ is called a π -pulse and, analogous, a pulse that rotates the TLS by $\theta = 90^\circ$ is called a $\pi/2$ -pulse. Consider now that we have a full ensemble of TLS ($|g \downarrow\rangle \leftrightarrow |e \downarrow\rangle$) that are all in the ground state $|g \downarrow\rangle$. By applying a $\pi/2$ -pulse we can rotate them into the superposition state $|\psi\rangle = 1/\sqrt{2}|g \downarrow\rangle + 1/\sqrt{2}|e \downarrow\rangle$ (with $\langle\psi|\psi\rangle = 1$). At first, they start to precess around the static field B_0 in phase. But then they immediately commence to dephase due to the T_2 and T_{inhom} dephasing effects. After a delay time t_{12} , we

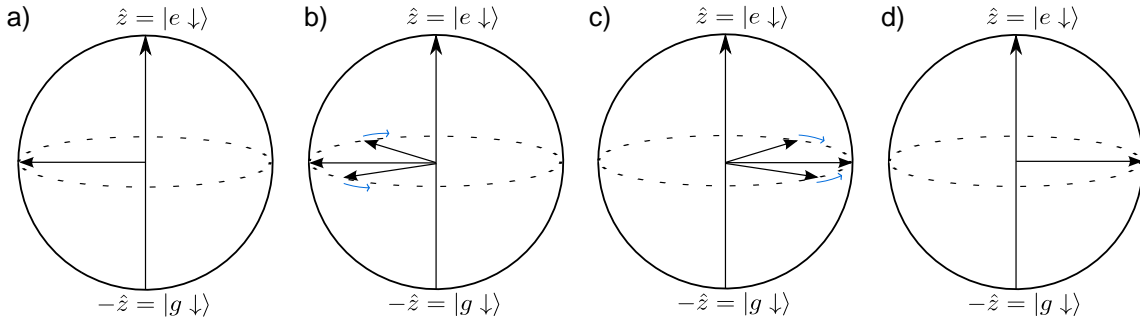


Figure 2.10: a) The $\pi/2$ -pulse excites the ensemble to the 90° superposition state. b) The ensemble starts dephasing along the azimuth ϕ immediately. c) After the delay time t_{12} a π -pulse is applied to rotate the ensemble by 180° . This effectively reverses the magnetic field. d) After another delay time period, the ensemble is rephased as T_{inhom} is recovered. An echo is emitted. Note, that for clarity these images do not contain the precession around \hat{z} and the actual T_2 dephasing, only T_{inhom} .

apply a π -pulse, which effectively means we reverse the magnetic field with respect to the Bloch vectors. This does not affect the T_2 relaxation, which cannot be recovered. However, the T_{inhom} dephasing cancels out now because it is approximately constant for times smaller than 1 ms. As a result, the Bloch vectors rephase again to a certain degree and after another delay time t_{12} the ensemble will emit a Gaussian shaped pulse as T_{inhom} is now completely recovered. This pulse is called photon echo.

The photon echo is rather weak compared to the pulses, about 1%. This can be explained by the fact that the ensemble does not absorb a large fraction of the

pulses and that some of the absorbed energy is dissipated otherwise, e.g. due to T_2 dephasing. The pulses should be as short as possible in order to allow neglecting the interaction time of the pulse with the ensemble. The actual rotation angle is dictated by the area under the pulse. Thus, we need to apply high pulse intensities.

If we now vary the delay time t_{12} , we get an exponential decoherence curve by plotting the echo intensity over the delay time. Basically, this gives us the T_2 decoherence time. For ideal TLS, the decoherence curve is a single exponential decay proportional to $\exp(-4t_{12}/T_2)$ [6]. The homogeneous linewidth may then be determined from the dephasing time T_2 by

$$\Gamma_{hom} = FWHM = \frac{1}{\pi T_2} \quad (2.26)$$

with the full width half maximum $FWHM$ (see section 2.1.3).

In a real system, alas, we usually deal with spectral diffusion. Thus, the observed photon echo becomes non-exponential. As the different contributions to T_2 cannot be separated from one another, we use an empirical decay shape first proposed by Mims [38] to describe spin echoes

$$I(t_{12}) = I_0 \cdot \exp \left[2 \left(\frac{2t_{12}}{T_M} \right)^x \right] \quad (2.27)$$

with the initial echo intensity I_0 . The exponent x determines the shape of the decay curve and the effective decoherence time T_M - which Mims called phase memory - over which the material decays to $1/e^2$ of its initial intensity.

In order to describe the empirical parameter T_M in real systems we need to know how it is influenced by spectral diffusion. The relations can be derived from the physical model for the echo decay [5], giving

$$T_M = \frac{2\Gamma_0}{\Gamma_{SD}R} \left(\sqrt{1 + \frac{\Gamma_{SD}R}{\pi\Gamma_0^2}} - 1 \right) \quad (2.28)$$

where Γ_0 is the linewidth in absence of spectral diffusion, Γ_{SD} is the full width at half maximum of the dynamic distribution of transition frequencies due to dipole-dipole interactions. R is the rate of the spectral diffusion process given by the sums of the spin flip transition rates.

An empirical linewidth $1/(\pi T_M)$ is often used in literature in analogy to the homogeneous linewidth in ideal TLS, however, this 'empirical' linewidth is not clearly defined in the presence of spectral diffusion as discussed by Böttger et al. [4]. They argue that only for the case that $R \ll T_M$ and $\Gamma_0 \ll \Gamma_{SD}$ can $1/(\pi T_M)$ be used as a true linewidth, or if $\Gamma_0 \gg \Gamma_{SD}$ and $T_M = T_2$ hold true. They chose to analyze the T_M values directly instead of analyzing $1/(\pi T_M)$. In this thesis we do likewise.

As the pulse sequence consists of two pulses, it is generally called 2PE (2-photon-echo) and it is also used for electron spin resonance and nuclear spin resonance where it is referred to as spin echo. One of the most important applications is certainly magnetic resonance imaging (MRI) where nuclear spin echo is used to identify and differentiate between tissues in the human body.

2.2.4 T_1 and 3PE

The relaxation processes parallel to the external magnetic field $\vec{B}_0 = B_0 \hat{z}$ are called T_1 decay. Spontaneous emission triggered through vacuum fluctuations is one effect that contributes to T_1 depending on the transition frequency. In nuclear spin systems, for instance, it is typically negligible but not in optical transitions. The other relaxation effect is spectral diffusion [6, 18]. At higher temperatures phonons play an important role.

T_2 is limited by T_1 by a relation that is valid in all TLS:

$$2T_1 \geq T_2 \geq T_2^* \quad (2.29)$$

For most systems T_1 is much larger than T_2 as it is furthermore suppressed by other mechanisms. In our case it is spin-spin interactions. We can measure T_1 by means of photon echo excitation just like T_2 but with a modified pulse sequence. This is called stimulated photon echo or 3PE as it consists of three $\pi/2$ -pulses (figure 2.11). The first two pulses are separated by a delay time t_{12} . The third $\pi/2$ -pulse is applied

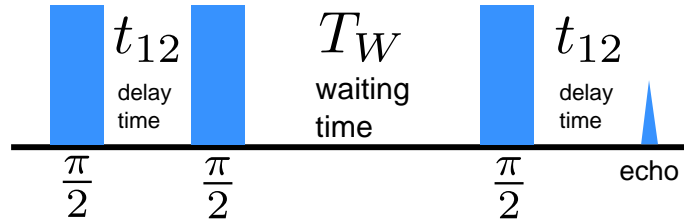


Figure 2.11: The 3PE pulse sequence consists of three $\pi/2$ -pulses. The first and the second are separated by the delay time t_{12} where the ensemble gathers some T_2^* dephasing. During the waiting time T_W the ensemble, now in the excited state, experiences T_1 depopulation. Eventually, the third pulse leads to a photon echo because T_{inhom} is fully recovered after another delay time period (also see section 2.2.3).

after a waiting time T_W and after another delay time period a stimulated echo is emitted.

The first pulse rotates the Bloch vectors by 90° where they start to dephase due to T_2 and T_{inhom} . The second pulse then excites all vectors that are dephased by less than π into the excited state, i.e., the upper half of the Bloch sphere. All vectors that are dephased by more than π are rotated back into the ground state, the bottom half of the Bloch sphere. Then, the vectors in the upper half begin to decay into the bottom half due to spectral diffusion and other mechanisms. The third pulse then brings the ensemble back into the superposition state where T_{inhom} starts to recover. After the waiting time period when T_{inhom} is completely recovered, an echo is emitted. This process is depicted in figure 2.12. The echo intensity depends on the T_2 dephasing as well as the T_1 population decay. By keeping the delay time and constant, the T_2 dephasing contribution is constant as well. Only the waiting time between the second and third pulse is varied. It is now possible to obtain T_1 as the decay of the stimulated echo intensity over the waiting time.

In the absence of spectral diffusion the echo intensity is proportional to two factors

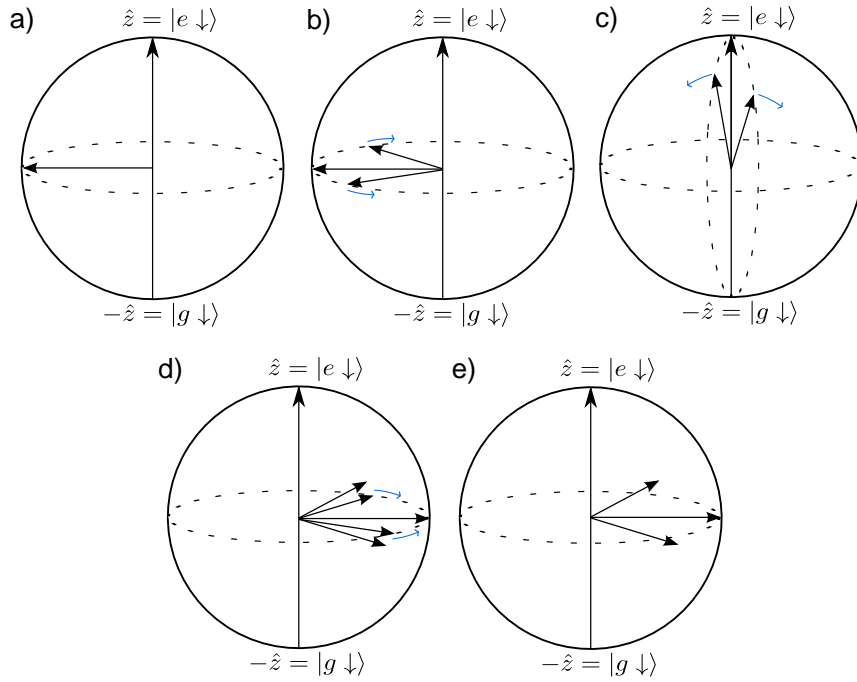


Figure 2.12: a) The $\pi/2$ -pulse excites the ensemble to the 90° superposition state. b) The ensemble starts dephasing along the azimuth ϕ immediately. c) After the delay time t_{12} a second $\pi/2$ -pulse is applied to excite the ensemble into the $|e \downarrow\rangle$ state. The ensemble starts to decay along the colatitude θ . d) After the waiting time T_W a third $\pi/2$ -pulse brings the ensemble back into the superposition state but with a reversed magnetic field compared to the first delay time period. e) After another delay time period the T_{inhom} (see section 2.2.3) is completely recovered. The 3PE echo is emitted which is typically stronger than a 2PE echo. Note that neither T_2 nor the precession around \hat{z} are depicted.

[5]. The first factor depends on $\exp(-2T_W/T_1)$ and corresponds to the depopulation during the waiting time T_W . The second factor is proportional to $\exp(-4t_{12}/T_2)$ and describes the dephasing effects due the homogeneous linewidth during the delay time t_{12} . It is constant because t_{12} is constant. The full width half maximum of that linewidth is given by $\Gamma_{hom} = 1/(\pi T_2)$. This results in the exponential decay form of the stimulated photon echo intensity [27]:

$$I(t_{12}, T_W) = I_0 \exp\left(-\frac{2T_W}{T_1}\right) \exp(-4t_{12}\pi\Gamma_{hom}) \quad (2.30)$$

where I_0 is the maximum echo intensity.

Unfortunately, the presence of spectral diffusion makes the situation more complex. Paramagnetic ions, such as Er^{3+} , are particularly sensitive to local field fluctuations because their magnetic dipole moment is very large [19, 5]. Magnetic dipole-dipole interactions are therefore a major source for spectral diffusion in these materials because the transition energy of each paramagnetic ion depends on the orientation of all other magnetic moments in the host. Thus, whenever an electronic or nuclear spin changes its orientation, all ions in close proximity are perturbed and experience

spectral diffusion.

Describing the influence of spectral diffusion during t_{12} and T_W can be done by introducing two additional factors [5, 38]. The first describes the spectral diffusion during t_{12} (see equ. 2.28), which causes a progressive loss of phase coherence between ions leading to a non-exponential dephasing process. The other factor corresponds to spectral diffusion during T_W which causes a linewidth broadening. The observed decay rate is affected because of the additional decoherence during the last t_{12} of the 3PE echo sequence. As discussed by Böttger et al. [5] these factors can be included by replacing the constant homogeneous linewidth with a time-dependent effective linewidth $\Gamma_{eff}(t_{12}, T_W)$

$$I(t_{12}, T_W) = I_0 \exp\left(-\frac{2T_W}{T_1}\right) \exp[-4t_{12}\pi\Gamma_{eff}(t_{12}, T_W)] \quad (2.31)$$

This effective linewidth is derived from the spectral diffusion factors while assuming a Lorentzian diffusion process. It can be written as

$$\Gamma_{eff}(t_{12}, T_W) = \Gamma_0 + \frac{1}{2}\Gamma_{SD}[Rt_{12} + (1 - \exp(-RT_W))] \quad (2.32)$$

where Γ_0 is the linewidth in absence of spectral diffusion which includes homogeneous linewidth and instantaneous spectral diffusion (ISD, see section 2.1.3). The latter refers to optical excitation as it changes the magnetic moments of the excited ions causing changes in the local fields of neighboring atoms [28]. Γ_{SD} is the full width half maximum of the dynamic distribution of transition frequencies due to dipole-dipole interactions and R is the characteristic rate of the spectral diffusion. R is given by the sum of the upward and downward spin-flip transition rates of the perturbing spins.

3 | Experimental Setup

This chapter describes the different experiments that we performed. Initially, the optical setups for the respective experiments with the different components are shown and we explain how the experiments were conducted. Subsequently, we describe how the integrated waveguide works with respect to design, fabrication, functioning and the coupling to the chip.

3.1 Optical Setup and Experimental Procedures

At first, we present the experimental setup for our measurements and explain the individual components. The setup is similar for all three fundamental experiments, namely the Zeeman splitting, the photon echo and the coupling to the integrated waveguide. For the first two we use an open beam through windows in the cryostat while for the integrated waveguide we need fibers inside of it. At this point we also outline how these experiments were conducted.

3.1.1 Zeeman Splitting

Initially, we want to measure the optical transitions of the $\text{Er}^{3+}:\text{Y}_2\text{SiO}_5$ crystal from the ground state $^4I_{15/2}$ to the first excited state $^4I_{13/2}$ as a function of the external magnetic field. The field lifts the two fold Kramers degeneracy through Zeeman splitting. Additionally, due to the nonequivalent magnetic orientations, there are twice as many optical transitions for each crystallographic site as expected. This is explained in sections 2.1.1, 2.1.2. Using a pair of Helmholtz coils, we gradually increase the magnetic field from zero to around 280 mT in steps of 5 mA (0.175 mT). This corresponds to a current of 8 A in the coils.

The measurement is conducted in the continuous wave (cw) mode and the laser frequency of our Toptica diode laser (figure 3.1) is swept back and forth in a range of about 13 GHz around the resonance frequency by means of a piezo crystal. The sweeping range of the laser needs to be adjusted to the splitting of the energy levels which depends linearly on the magnetic field to get the best resolution. The sample holder with the crystal is mounted inside the Helmholtz coils, carefully aligned to the center of the optical windows of our Bluefors cryostat. The best signal to noise ratio can be achieved by using very low intensities of around $2.5 \mu\text{W}$. A photo detector is used to measure the signal.

As shown in figure 3.2, the first part of the optical setup is mounted on an optical table with air pressure damping to suppress vibrations. The laser beam of our

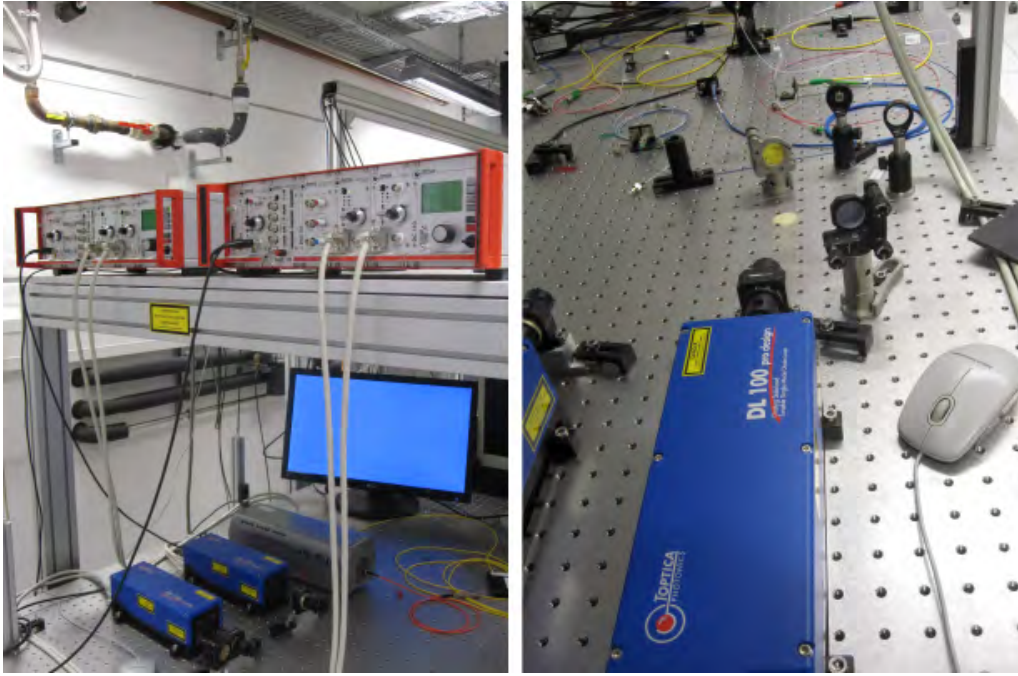


Figure 3.1: *Left:* Our two Toptica diode lasers (blue) on the table and their drivers above. With the drivers we can control the power output and initialize a frequency sweep by means of a piezo element. The lasers work in the NIR regime between 1520 nm and 1550 nm and have a maximum power output of around 50 mW.

Right: One of the lasers, the optical insulator as well as two gold plated mirrors and a beam collimator to couple into an optical fiber.

near-infrared (NIR) diode laser first passes an optical isolator (figure 3.3), which light can only pass in one direction, to account for the vulnerability of the laser regarding feedback. Then, it is coupled into a fiber via a beam collimator (figure 3.4). Two gold plated mirrors are used to control the four degrees of freedom, namely the angle and the height in both the x and the y direction. This is crucial for efficient coupling to the fiber. Aligning the mirrors takes some practice at first.

A beam splitter diverts one percent of the beam towards a wavelength meter (figure 3.3) with an absolute accuracy of 2 MHz, which is connected to the lab computer via USB. Afterwards, the intensity of the rest of the beam is decreased by a tunable attenuator. Polarization maintaining fibers in a cable bridge guide the light to the cryostat.

The optical table around the cryostat represents the second part of the optical setup. The light is coupled out of the fiber by a beam collimator and passes a couple of mirrors used for alignment. Subsequently, a polarization filter assures a defined polarization in the sample which is important as the crystal is highly anisotropic regarding absorption. With the $\lambda/4$ and the $\lambda/2$ wave plate in front of the polarization filter we can rotate the polarization. The $\lambda/4$ transforms an arbitrary elliptical polarization into a linear one. The $\lambda/2$ wave plate can rotate the linear polarization by a certain angle. This ensures that the intensity after the polarization filter is maximal. The polarization maintaining fibers help to stabilize the intensity inside the fibers. They are fabricated under tension to maintain a certain strain. Any changes in me-

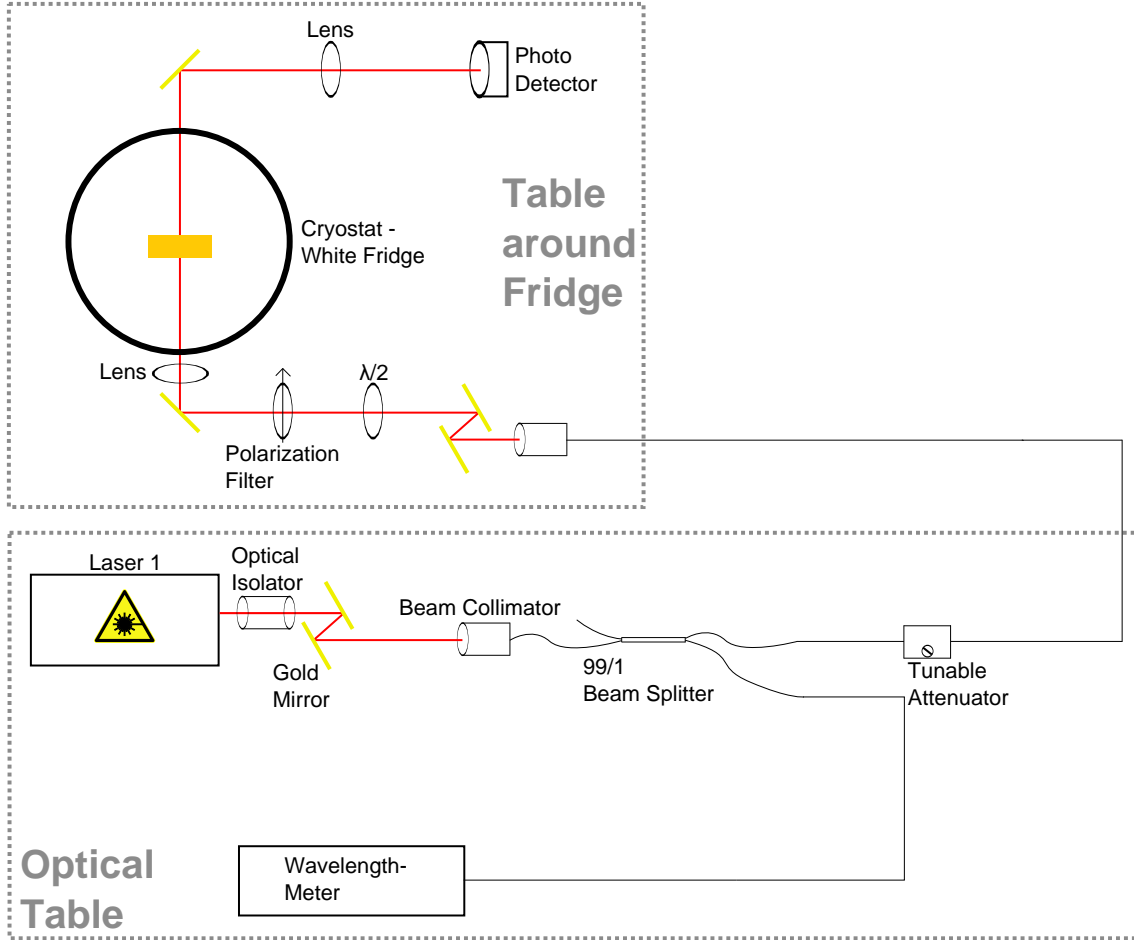


Figure 3.2: Setup for Zeeman splitting; the laser beam passes an optical isolator to protect the laser from feedback and a beam splitter to measure the frequency accurately with the wavelength meter. Then, it is focused through the windows of the cryostat onto the crystal. The signal is detected by a photo diode after the cryostat. We apply a magnetic field with a pair of Helmholtz coils and observe all optical transitions in $\text{Er}^{3+}:\text{Y}_2\text{SiO}_5$ from the ground state to the upper state by sweeping the laser over the resonance frequency. The readout is performed via a digital oscilloscope.

chanical strain in the fibers would affect the refractive index leading to polarization shifts which typically appear in an oscillating manner. Such polarization oscillations have a direct impact of the laser intensity at the sample due to the polarization filter.

Then, the beam is focused by a lens through the optical window of our cryostat onto the crystal situated in a copper sample holder (figure 3.5). The cryostat has a base temperature of around 25 mK. It achieves this by using a mixture of ^3He - ^4He as cooling liquid.

After passing the sample, the light comes out of the second window of the cryostat. It is focused on the ThorLabs photo detector, depicted in figure 3.6. The detector is operated at 50 dB gain and connected to a digital oscilloscope, which is utilized to convert the electrical signal into digital data. The data is averaged over 100 acquired cycles to improve the signal to noise ratio. Conveniently, the oscilloscope is interfaced with a computer to allow automated measurement scripts. This

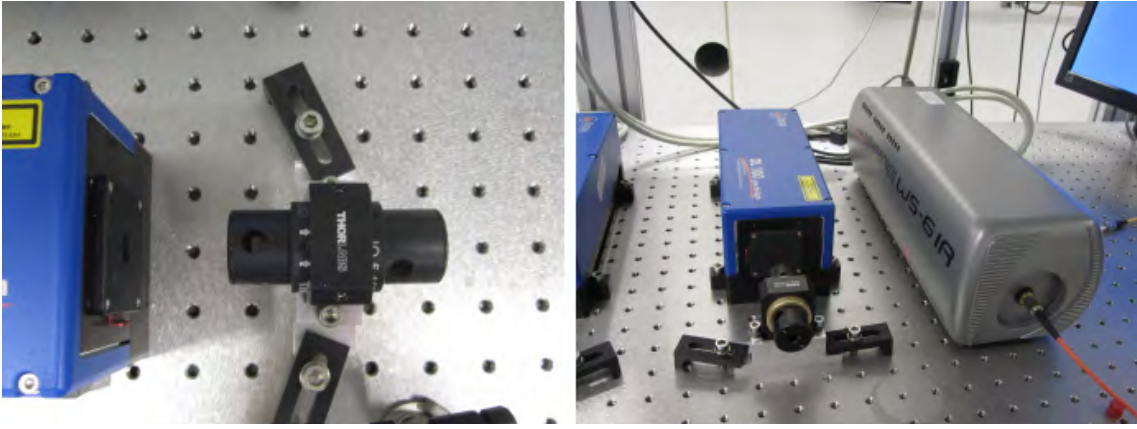


Figure 3.3: *Left:* The optical insulator is important to prevent feedback to the lasers because they are highly vulnerable to back-reflection.
Right: With the wavelength meter, we can accurately measure the laser frequency. A fiber-coupled 99/1 beam splitter delivers a continuous beam of small power.



Figure 3.4: *Left:* A gold mirror for alignment which has a very high reflectivity.
Right: A beam collimator used to couple light into an optical fiber.

makes it possible to gain a very high magnetic field resolution.

3.1.2 Photon Echo

We determine the optical coherence times, T_1 and T_2 , of the erbium crystal by measuring the photon echo intensities of the 2PE and 3PE sequences introduced in sections 2.2.3 and 2.2.4. By altering the delay time and the waiting time between each measurement, respectively, we can determine the coherence times depending on the temperature and the magnetic field.

A photon echo can only be achieved by applying a sequence of light pulses which requires an active modulation element. We use acousto-optic modulators (AOM, figure 3.7) with an operation frequency of 200 MHz to create these sequences. An AOM consists of a crystal in which sound waves are generated with a certain frequency. These sound waves create an optical lattice which acts as a Bragg grating diffracting an incoming light beam. By aligning the optical setup to the diffracted



Figure 3.5: *Left:* Our Bluefors cryostat has a base temperature of around 25 mK and achieves this with a mixture of ^3He and ^4He . The optical setup on the table around the cryostat is aligned to the windows.

Right: The cryostat consists of several different temperature stages. In this picture we see the 25 mK plate, the 700 mK plate and the 4 K plate. Below the 25 mK plate is our pair of Helmholtz coils delivering up to 280 mT at a current of 8 A.

beam of first order we can use any electrical signal as input for the AOM driver (figure 3.9). Thus, the driver delivers a signal to the AOM which converts an incoming light beam accordingly. Our AOMs are not fiber-coupled so it is necessary to couple the beam out of the fiber before the AOM and back in thereafter, which is also depicted in figure 3.8. The intensity of the diffracted beam of first order depends on the alignment and can reach up to 60% of the incoming beam. In our case the π -pulse is 500 ns.

Subsequently, the pulses are guided to the optical table around the cryostat. The beam radius is 1.5 mm after coupling out of the beam collimator. It is defined as the distance from the beam axis to the point where the optical intensity drops to $1/e^2$ of the intensity at the beam axis. Since we deal with a Gaussian beam, we increase the radius to 5 mm in order to get a very small focal point inside the sample. This allows for the use of very short pulses compared to the delay time between the pulses for a given intensity. We will shortly outline the specific properties and behavior of a Gaussian beam.

The intensity distribution of such a beam in any direction vertical to the propagation direction is well modeled by a Gaussian distribution. The fundamental transverse mode of all stable cavities is usually a Gaussian beam, hence most lasers emit such a beam. It is characterized by a beam waist where the beam radius is minimal



Figure 3.6: *Left:* Our ThorLabs photo detector with a maximum gain of +70 dB. We use it to detect the Zeeman splitting and for the pulses in the photon echo experiment as well as for the integrated optics part. *Right:* The digital oscilloscope by Tektronix has 4 channels with an additional trigger input and is interfaced with our lab computer to conduct automated measurements.

while on either side of the waist the beam radius increases. When refracted at a diffraction-limited lens, a Gaussian beam is transformed into another Gaussian beam with different parameters, notably the radius of the beam waist and the distance of the waist to the lens.

For a Gaussian beam propagating in free space with a wavelength λ and a waist radius w_0 , the beam radius at a distance z from the waist is given by ([46, 33, 50])

$$w(z) = w_0 \sqrt{1 + \left(\frac{z}{z_R}\right)^2} \quad (3.1)$$

where z_R is the Rayleigh range which defines the distance from the waist to the point where the beam radius is $\sqrt{2}w_0$

$$z_R = \frac{\pi w_0^2}{\lambda} \quad (3.2)$$

At this distance the beam can be considered to be parallel. The waist radius w_f of a Gaussian beam transformed by a diffraction-limited lens with focal length f is

$$w_f^2 = w_0^2 \frac{f^2}{z^2 + z_R^2} \quad (3.3)$$

where w_0 , z and z_R correspond to the initial beam.

With a beam radius of 5 mm, the Rayleigh range is

$$z_R = \frac{\pi \cdot 5 \text{ mm}}{1538 \text{ nm}} \approx 51 \text{ m} \quad (3.4)$$

We use a lens with the focal length $f = 0.3 \text{ m}$ to focus the beam on the crystal through the optical windows of the cryostat. Since $z_R \gg f$, we can assume a parallel beam before the lens and, thus, the beam waist of the transformed beam is approximately at the focal point of the lens. This is where we place the crystal,

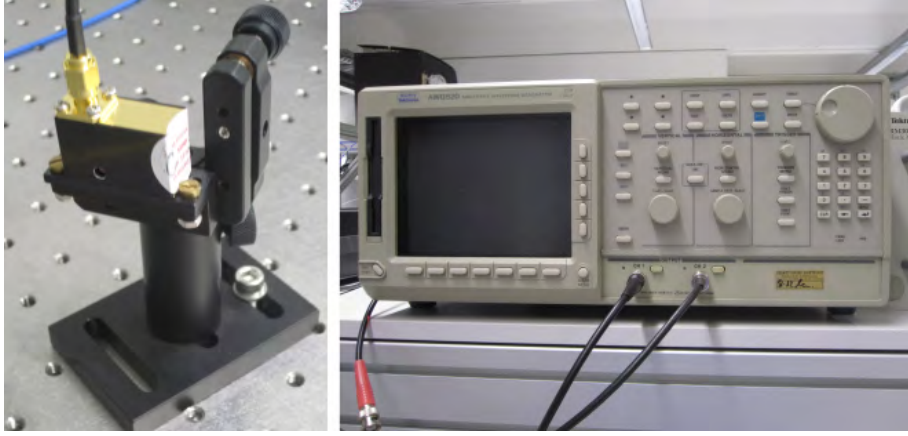


Figure 3.7: *Left:* We use AOMs (acousto-optical modulators) to generate the optical pulses. In our case the π -pulse is 500 ns. When an electrical signal is applied the AOM produces sound waves inside a crystal which diffract the light propagating through that crystal. The diffracted light in first order is used as optical pulse.

Right: With the AWG (arbitrary waveform generator) we generate the electrical pulses that are fed to the driver of the AOM.

which means z is in the order of millimeter and therefore negligible compared to z_R . With these assumptions equation 3.3 can be approximated by

$$w_f = \frac{f \lambda}{\pi w_0} = \frac{0.3 \text{ m} \cdot 1538 \text{ nm}}{\pi \cdot 5 \text{ mm}} \approx 30 \mu\text{m} \quad (3.5)$$

If we used a beam radius of 1.5 mm instead, the waist radius at the sample would be

$$w_f = \frac{0.3 \text{ m} \cdot 1538 \text{ nm}}{\pi \cdot 1.5 \text{ mm}} \approx 100 \mu\text{m} \quad (3.6)$$

The intensity would have to be that much higher for us to use the same pulse lengths because the mode volume would be bigger and, hence, the field strength smaller. This would be disadvantageous because of interaction effects that can happen during the pulse.

We employ a telescope to widen the beam radius from 1.5 mm to 5 mm before the cryostat. It consists of two lenses with $f_1 = -7.5 \text{ cm}$ and $f_2 = 25 \text{ cm}$ positioned at a distance of $d = -7.5 \text{ cm} + 25 \text{ cm} = 17.5 \text{ cm}$ with a magnification factor of 10/3.

An arbitrary waveform generator (AWG, figure 3.7) with two channels, which we trigger externally, provides the input signal for the AOMs. The trigger frequency of the AWG, which means the repetition rate for the pulse sequences, is 4 Hz, which is more than ten times T_1 . Therefore, we can assume that all erbium atoms are in the ground state at the start of each pulse sequence. The first AOM generates the pulse sequence while the second AOM is only opened for a small time window to detect the photon echo, excluding the excitation pulses. Since the intensity of the pulses of the generated sequence is larger than the echo intensity by a factor of about 100, the detector would saturate and could not be trusted to be accurate regarding the relative intensity during the photon echo. This is why we use a second, much faster detector which is aligned to the diffracted signal of the second AOM to detect the

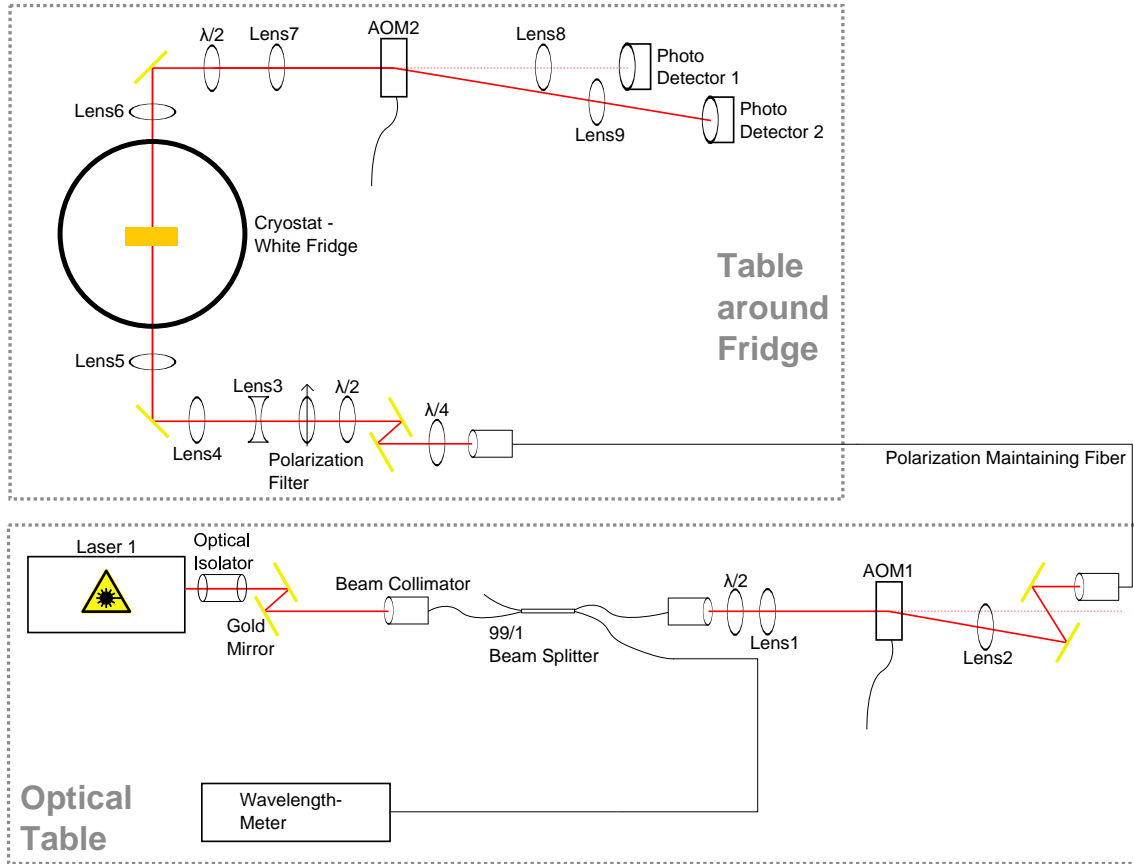


Figure 3.8: We excite a photon echo by applying a pulse sequence to determine T_1 and T_2 of the erbium crystal. An arbitrary waveform generator (AWG) is utilized as source for an acousto-optic modulator (AOM) that transforms the electrical input signal into an optical signal using the acousto-optic effect. A second AOM protects the detector from saturation effects due to the high intensity pulses as it is only opened after the pulse sequence to measure the echo. Pulse sequence generation and data readout are automatically carried out with QTLab.

actual photon echo. On the other hand, the ThorLabs detector is used for the zero order beam as a reference to detect the optical pulses.

Both detectors are connected to an oscilloscope which is triggered with a marker signal by the AWG. The AWG and the digital oscilloscope are interfaced with a computer to allow us the use of automated measurement scripts. This results in a high resolution for the delay time and the waiting time of the 2PE and the 3PE sequences, respectively.

3.1.3 Integrated Solution

In addition, we want to demonstrate that an integrated solution is possible. Thus, we want to probe coupling between an integrated waveguide and the erbium crystal. We use a silicon based chip with an optical waveguide which is coupled to the crystal via evanescent waves. A fiber array with optical fibers is aligned to the grating couplers on the chip to couple to the integrated waveguide. Hence, we need to install fibers in the cryostat and fusion splice them with the fibers of the fiber array. In order to

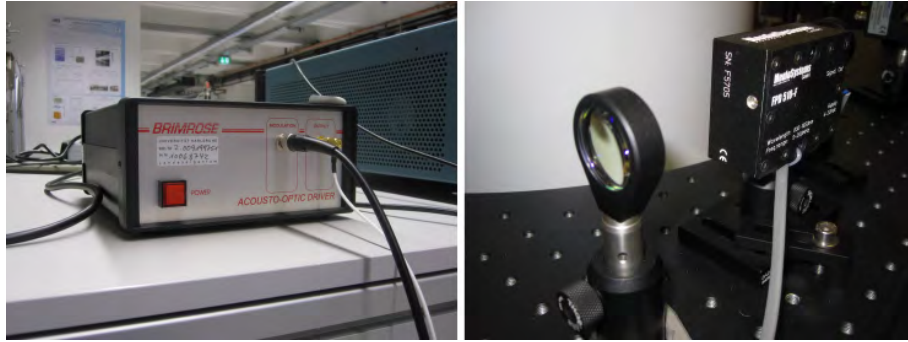


Figure 3.9: *Left:* The driver of the AOM.

Right: Our second photo detector is much faster than the ThorLabs detector and, hence, well equipped to assimilate the actual photon echo data. It does not have gain, though. A second AOM just in front of the detector ensures that only the echo signal passes through to this detector and not the optical pulses since they are much stronger and might lead to unwanted saturation effects in the detector.

to seal the vacuum of the cryostat we use a two component epoxy glue to fill the small metal tubes through which the fibers enter the cryostat. In addition, aluminum film is used to shield off hot photons inside the cryostat between the different stages. The ThorLabs detector with 50 – 70 dB gain is used to detect the signal and account for high losses inside the integrated waveguide and during coupling.

3.2 Integrated Optics

This section is devoted to the optical chip spanning every development step from design over fabrication and optimization to the actual measurement.

3.2.1 Substrate

We use a silicon bulk of several hundred micrometers with 2.6 μm SiO_2 and a 450 nm polished Si_3N_4 layer. The Si_3N_4 layer has a refractive index of about 1.97 at 1550 nm and serves as the actual waveguide. The SiO_2 layer and air, with the refractive indices of around 1.44 and 1.00, respectively, allow for total internal reflection of light in the Si_3N_4 layer at the interfaces. This is basically the same idea as with optical fibers. The maximum angle for total internal reflection at an interface can be obtained from Snell's law relating the angles of incidental (*inc*) and transmitted (*trans*) light beam when refracted at an interface

$$n_1 \sin \theta_{inc} = n_2 \sin \theta_{trans} \quad (3.7)$$

The chips are cut from a wafer by scribing the predetermined breaking lines with a diamond cutter into the unpolished silicon surface and subsequently bending the wafer over a plastic edge at this line. We usually cut 15 · 15 mm² chips. This is convenient for the specific sample holder of the Jeol electron beam lithograph that we use. The chips are stored in plastic protection cases to keep them clean of dust and other contamination.

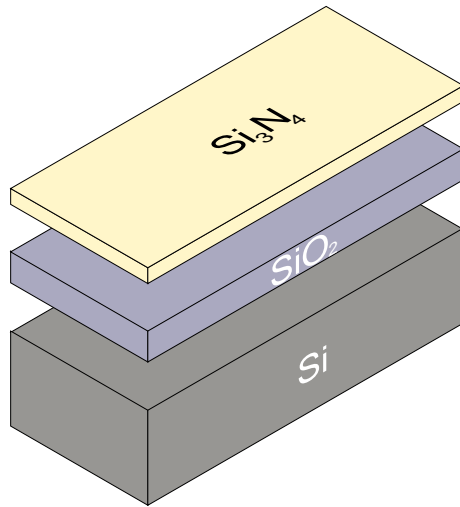


Figure 3.10: The substrate we use consists of several hundred micrometers of silicon, $2.6\ \mu\text{m}$ SiO_2 and $450\ \text{nm}$ Si_3N_4 . The actual waveguide is in the Si_3N_4 layer which can guide the light by means of total internal reflection.

3.2.2 Mode Simulation

We simulate the waveguide with the physics simulation software Comsol. This enables us to calculate the modes in the waveguide for different waveguide widths to determine the best design for the attempted experiment. All that needs to be done is make a geometrical cross section of the waveguide and the surrounding material and assign a refractive index to each of them. Comsol then calculates a predefined number of solutions for the electric field, the magnetic field and the effective refractive index. Basically, the effective refractive index is the refractive index for a certain mode with the specific surrounding materials. As can be seen in figure 3.11 a) and b), the fundamental modes TE_{00} and TM_{00} , in this case for a width of $1.2\ \mu\text{m}$, are very close together in terms of their refractive indices. This means, that it is very difficult to fabricate a waveguide in which, e.g., TE_{00} is guided but not TM_{00} .

It turns out that those modes are guided in a waveguide starting at a width of about $700\ \text{nm}$. Moreover, at a width of $1.25\ \mu\text{m}$ there are already higher order modes of TE and TM (see figure 3.11 c). Since we are interested in single mode operation we choose a waveguide width of $1\ \mu\text{m}$. The fact that we actually have two stable modes with TE_{00} and TM_{00} is not really an issue because a grating coupler only couples in one of these modes. Figure 3.11 d) shows a mode that is not stable in the waveguide with a width below $700\ \text{nm}$. This can be verified easily enough as the maximum intensity lies far outside the waveguide.

3.2.3 Design

The design of the devices is developed in Cadence, an electronic design automation program. With Cadence it is possible to export the .gds file needed for the electron beam lithography process. Fortunately, a lot of the fundamental functions already exist in Wolfram Pernice' group at the INT (Institute for Nano-Technologies at KIT) such as straight waveguides, bent waveguides and most importantly the grating couplers. The couplers work like Bragg gratings to couple light from a fiber into the integrated waveguide.

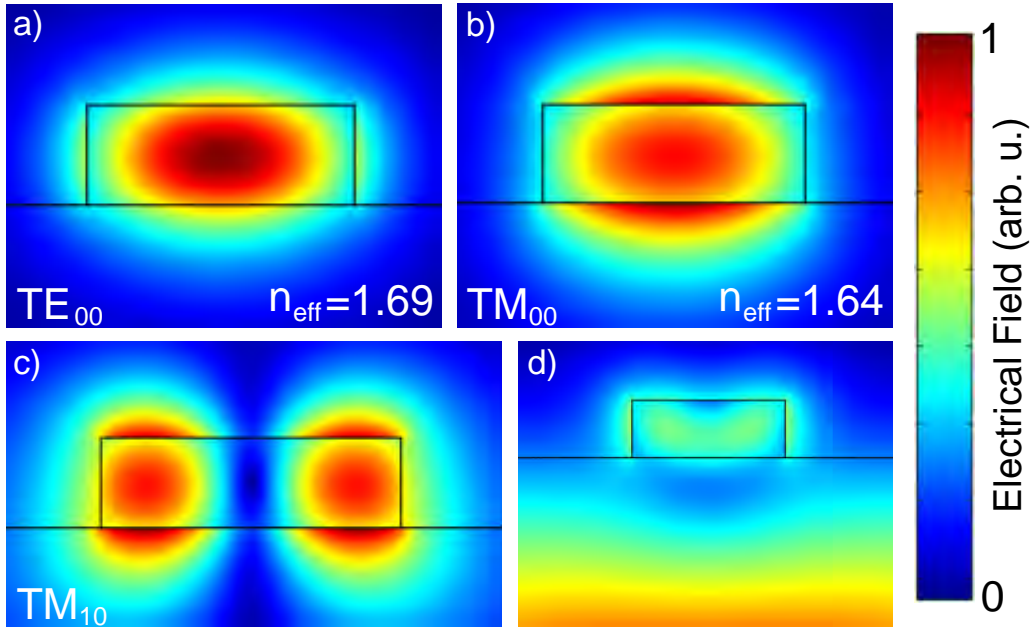


Figure 3.11: Simulation of modes in the waveguide with comsol; a) and b) show the fundamental modes TE_{00} and TM_{00} at a waveguide width of $1.2 \mu\text{m}$, c) is a mode of higher order, TM_{10} , at a width of $1.25 \mu\text{m}$ and d) shows a mode that is not guided in the waveguide. We use a width of $1 \mu\text{m}$ for our devices since we get TE_{00} and TM_{00} starting at a width of about 700 nm and higher orders from $1.25 \mu\text{m}$ on.

Hence, the task is to use these elements to produce a device which solves the problem at hand. In our case we need a long transmission line on which we want to place the crystal to get evanescent wave coupling to optically excite the erbium ions (see figure 3.12). Initially, the marker around the couplers were implemented to help gluing a fiber onto each coupler. However, this did not work well as explained in section 3.2.10. The bending radius of the waveguide is $50 \mu\text{m}$ while it spans an area of $2.6 \cdot 1.9 \text{ mm}^2$. The distance between the couplers, called pitch, is $750 \mu\text{m}$ in order to be able to measure it with the fiber array in the measurement setup (section 3.2.5). The transmission line is about 6 cm long.

3.2.4 Fabrication

We fabricate the chip by coating it with a positive photo resist. This resist is then illuminated by means of electron beam lithography at every point which is supposed to be removed when developing the resist. The resist now functions as an etching mask for reactive ion etching (RIE) with CHF_3 and O_2 to manufacture the waveguide in the Si_3N_4 layer. All steps except for the etching are carried out in the CFN (Center for Functional Nanostructures at KIT) cleanroom with ISO 6 standard, which means that there are less than one million particles per cubic meter.

Before applying the photo resist via a spin coater, it needs to be cleaned. The first step is an eight minute ultra sonic bath during which the chip is covered in acetone to remove particles as small as a couple of micrometers. Then, it is cleaned in isopropyl alcohol and dried with a nitrogen gun. The subsequent oxygen plasma,

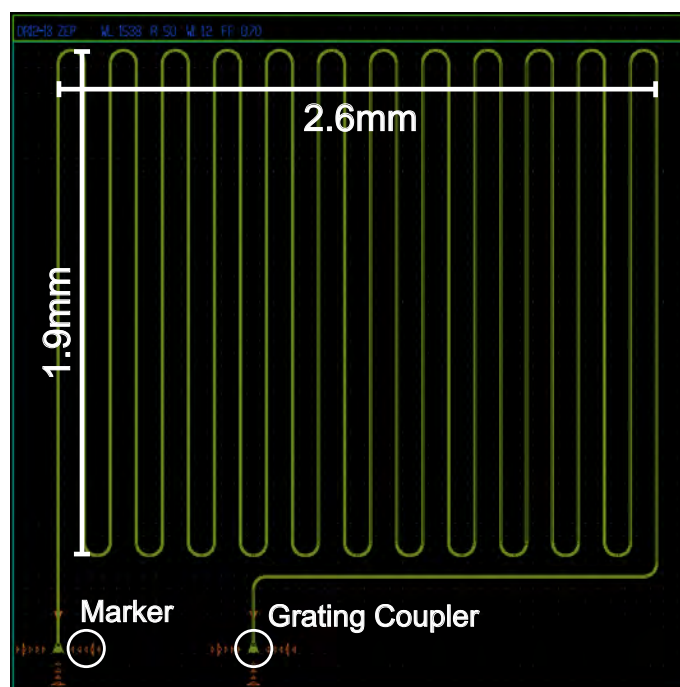


Figure 3.12: The devices are designed with Cadence to create a .gds file. We use a 6 cm long transmission line in a meander form on which the crystal is placed to get good evanescent coupling. Light is coupled in from a fiber on top of a grating coupler. After propagating through the whole waveguide, it is coupled out into a second fiber above the other grating coupler.

to which the chip is exposed for five minutes, ensures that the chip is devoid of organic molecules. Now it is time to apply the positive photo resist "ZEP 520A". The spin coater is set to one minute with a rotation frequency of 6000 per minute which results in a layer thickness of around 400 nm. Afterwards, the thickness can be precisely measured with a thin-film thickness measurement tool by Filmetrics. This is necessary to set the charge dose of the electron beam accordingly to ensure that the beam penetrates the whole resist. Now, the chip is ready to be exposed to the electron beam.

The CFN maintains an electron beam lithography system by JEOL. Apart from the .gds design file all that is needed to illuminate the chip is the charge dose of the beam and a near-field approximation which accounts for all the edges in the design by adjusting the dose in these regions. This lithograph uses two means of directing the electron beam. For small areas the beam is deflected under an angle. However, this covers only a region of $100 \cdot 100 \mu\text{m}^2$, which is called a writing field. To illuminate the next writing field a lateral movement in the x-y plane is used which is, unfortunately, not as precise and might cause so called stitching errors at the interface of two writing fields. To prevent any problems arising from this we make sure that the most sensible elements such as couplers are always placed entirely inside of one writing field.

The process of illumination takes about 1.5 h for each device in our case. It is essential that the chip is developed promptly after the exposure to achieve a good result. ZEP is developed in a xylene bath for 50 s. Afterwards it is cleaned with

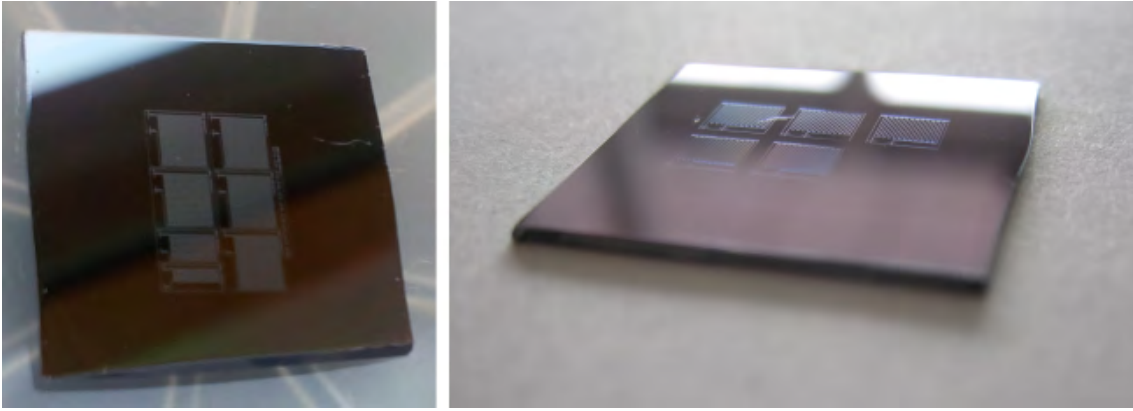


Figure 3.13: The chips are fabricated using an electron beam lithography system to write the nanostructures into a photo resist applied with a spin coater. This serves as an etching mask for reactive ion etching (RIE).

isopropyl alcohol. We use a reflow process to accomplish a higher surface quality of the developed resist interfaces. This is done by heating the chip up to 145 °C for three minutes. In principle, the resist is now stable and the chip can be safely stored for months before etching it.

We etch the chips at the INT with a reactive ion etching (RIE) system by Oxford. Before the actual etching process can start, we prepare the condition in the reaction chamber by applying a SF₆ plasma for 5 minutes and afterwards an oxygen plasma for 50 minutes. Since we use a positive resist, only a small part of the resist which surrounds the waveguide is removed during development. Thus we cannot measure the thickness of the Si₃N₄ layer directly on the chip and have to employ a reference substrate which is simply a small piece of the same wafer but without the resist. This allows us to check the etching rate half way through the process and adjust the etching duration in order to etch the Si₃N₄ completely through but none of the SiO₂ layer beneath it. Afterwards, the remaining resist is removed by an oxygen plasma.

3.2.5 Measuring the Devices

After fabrication the devices are measured to ensure that there are no defects and the devices work fine. This is done by moving a fiber array with well defined fiber distances by means of a piezo stage above the couplers and measure optical transmission. The chip is placed on a stage which can move in the x and y directions via micrometer screws as well as piezo-controlled. The fiber array is mounted on a rack which can be moved in the z direction by a mechanical screw and electrically with a piezo as well. A tunable laser in the telecom C-band range is used to sweep the frequency between 1510 nm and 1620 nm when measuring transmission. A camera above the stage helps with aligning the fiber array.

The polarization of the laser beam is controlled with a fiber polarization controller (FPC). It can transform an arbitrary polarization into another arbitrary one with three consecutive waveplates. The first is a quarterwave plate which transforms the incoming elliptical polarization into a linear polarization, a halfwave plate then rotates the linear polarization by an arbitrary angle and another quarterwave plate

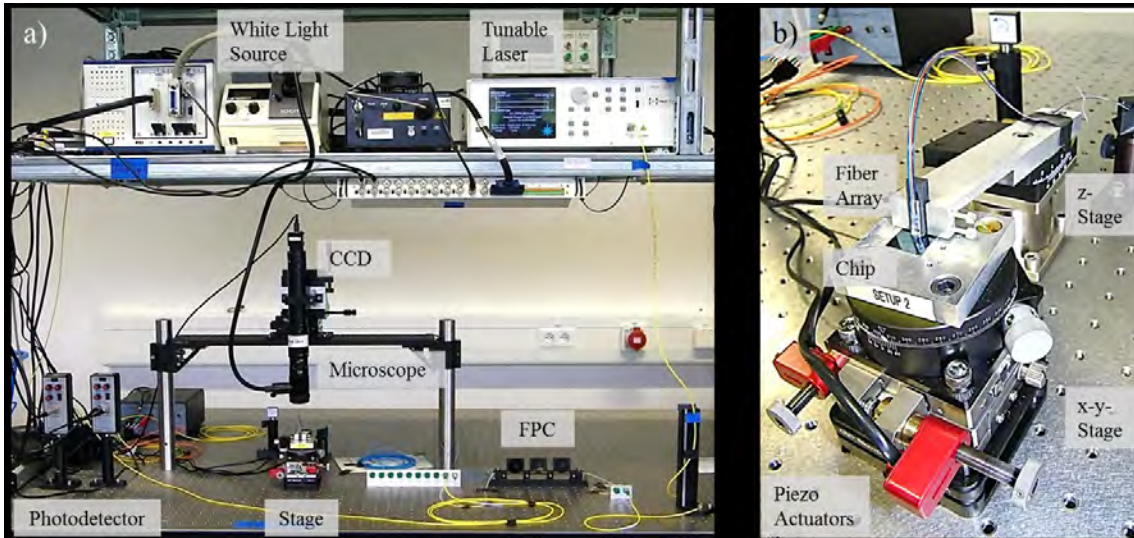


Figure 3.14: We measure the devices by moving a fiber array above the grating couplers via a piezo stage. By using a tunable laser sweeping the frequency, we obtain a graph with intensity over frequency. Polarization fluctuations are effectively suppressed by employing a polarization controller (FPC). (Images by Nico Gruhler, INT)

finally transforms the linear polarization into an arbitrary elliptical one. This is necessary because the coupling efficiency of the grating couplers depends strongly on the polarization. Hence, by setting the FPC to maximum transmission, we eliminate any intensity fluctuation due to polarization changes in the fibers. We can now determine the absolute intensity losses due to coupling and transmission in the integrated waveguide. Sweeping the laser frequency allows us to determine the maximum transmission for each device as a function of the frequency.

3.2.6 Grating Coupler

One of the most important things in integrated optics is a way to couple light in and out of a circuit. One method is the so called end-fire approach where a fiber is aligned to a waveguide from the side of the chip. This approach achieves very low coupling losses [36] and can be achieved by either especially polished and cleaved waveguides [32] or by adjusting the geometric aspect ratio to better match the field profiles [7].

Another way is to use prisms [47] or grating couplers [11] which have much higher coupling losses but are easier to access. Therefore, they allow for measuring a much larger number of devices on a chip and, in the case of the grating coupler, are much faster to align for characterization of the devices. We use grating couplers to couple to the integrated transmission line on the chip. They consist of a pattern of equidistant bars etched into the Si_3N_4 layer (see figure 3.15) to form a triangle. The top end of that triangle is a large area of Si_3N_4 which gradually decreases in width until it seamlessly becomes the waveguide itself. This is called the taper. Note that we work with a positive resist which is why we etch only a $4\ \mu\text{m}$ wide strip on both sides of the waveguide and around the grating coupler.

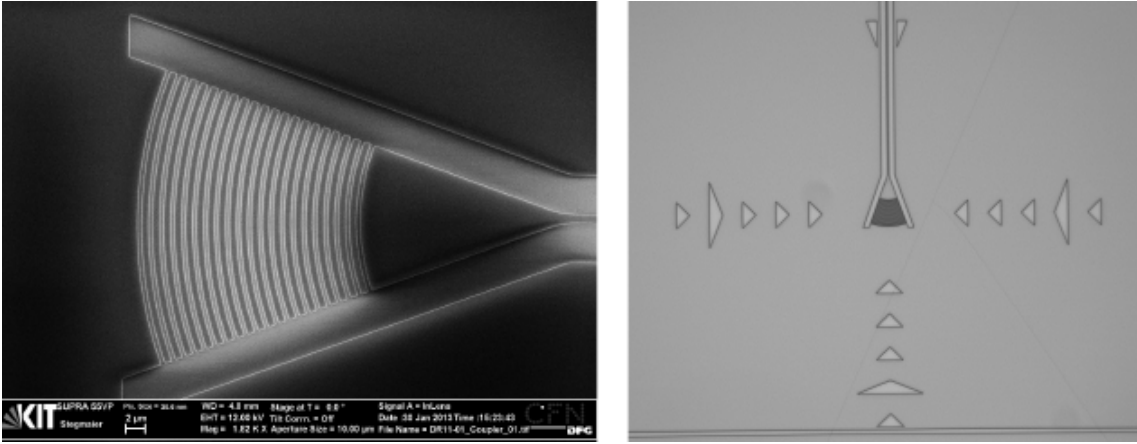


Figure 3.15: A SEM and a microscope picture of a grating coupler, which is used to couple light into and out of the integrated waveguide. The markers around the coupler in the microscope image were intended for alignment while gluing single fibers onto the coupler.

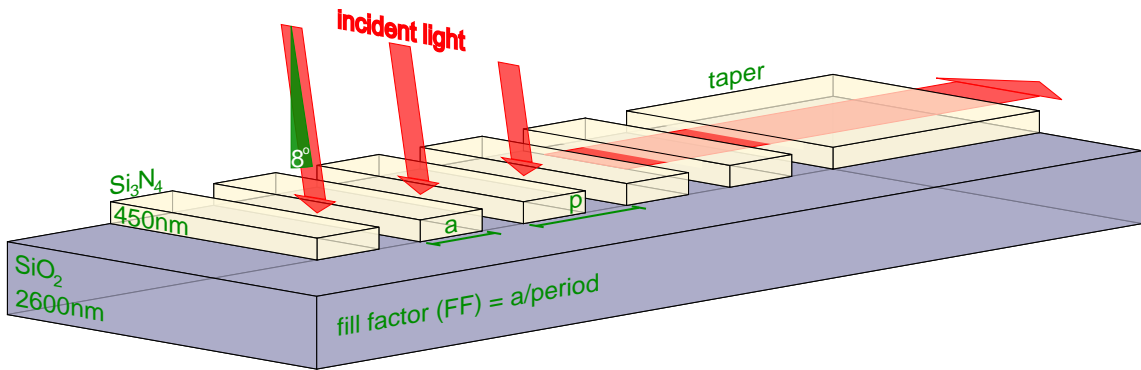


Figure 3.16: Light that propagates through the vertical interfaces of a grating coupler is diffracted in directions which meet the Bragg condition. The coupler is constructed in such a way that the incidental light for specific angle is diffracted into the waveguide in first order.

Grating couplers work similar to a Bragg grating (figure 3.16) and couple light into the waveguide that propagates from above through the side walls of a grating bar. Depending on the incident angle, in our case optimized to 8° , the light is then diffracted in directions which meet the Bragg condition

$$p(n_{dif} \sin \theta_{dif} - n_{inc} \sin \theta_{inc}) = m\lambda \quad m \in \mathbb{N} \quad (3.8)$$

The indices *inc* and *dif* mean incident and diffracted, respectively. The coupled mode theory describes grating couplers in a more detailed way [29, 37] including spectral width and efficiency.

3.2.7 Parameter Optimization

It is essential that a couple of parameters of the device are adjusted to meet the specific requirements of the used wavelength and material. At first we optimize the fill factor (FF) of the grating coupler and its period. The FF is the length of one grating bar divided by the period: $FF = a/p$ (see figure 3.16). Both parameters ensure maximum coupling efficiency for an arbitrary wavelength in the employed ma-

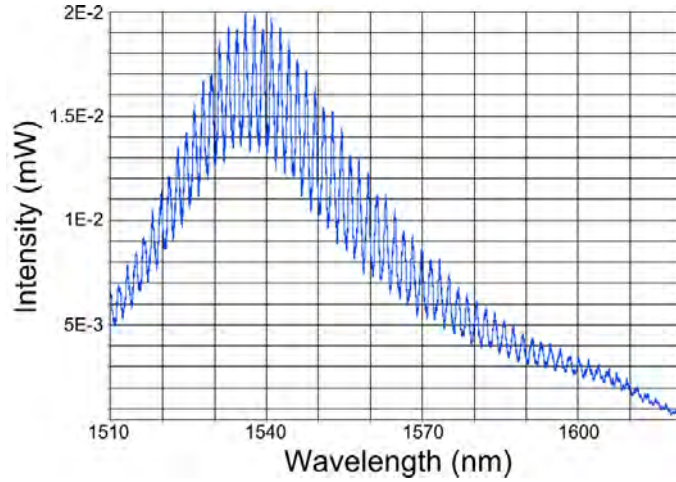


Figure 3.17: The transmission intensity over laser frequency for a two-coupler-device typically has a Gaussian shape. The sinusoidal oscillations overlaying this shape are Fabry-Perot interferences caused by back-reflections from the grating coupler.

terial. Having varied these parameters for a number of simple two-coupler-devices, the most efficient FF is 0.7 with a period of $1.123 \mu\text{m}$ for the wavelength 1538 nm . Since the period p (in μm) is approximately linear to the wavelength wl (in nm) for maximum coupling in a certain range, we can convey this with the following equation for $FF = 0.7$

$$p(wl) = \frac{wl - 517.8 \text{ nm}}{909.1} \quad (3.9)$$

The transmission spectrum of a grating coupler is approximately a Gaussian envelope (figure 3.17). Moreover, there are oscillations corresponding to the internal reflections of a Fabry-Perot interferometer which is unintentionally realized by fabricating equidistant grating bars with the same width. The transmittance T of such an interferometer can be written as [29]

$$T = \frac{1}{1 + F \sin\left(\frac{\delta}{2}\right)} \quad (3.10)$$

with the phase shift per round trip δ and the factor of the finesse F

$$F = \frac{4R}{(1 - R)^2} \quad (3.11)$$

while R is the radius of the ring.

An effective way of eliminating such oscillations is the use of so called apodized grating couplers [1]. This means that over the length of about ten grating bars before the taper the width of those bars is gradually increased which leads to destructive interference of reflected light at different grating bars.

To maximize the coupling efficiency, it is again important to optimize the parameters. In this case we optimize the number of normal grating bars and the period because the wavelength of maximum coupling gets shifted (figure 3.18). Taper length and number of apodized grating bars were kept constant as they should not have a

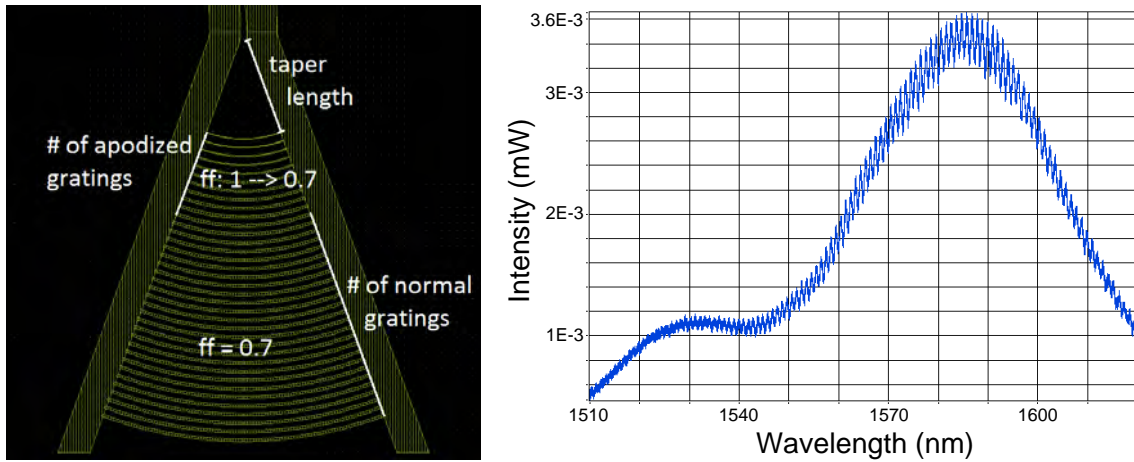


Figure 3.18: Apodized couplers are used to suppress the Fabry-Perot oscillations by varying the fill factor. Reflected light at different grating bars undergoes destructive interference resulting in decreased oscillations.

large effect on the efficiency. Unfortunately, the Fabry-Perot oscillations are not suppressed entirely but they are weakened. Probably the parameters should have been varied over a larger range of values. There seems to be a second Gaussian envelope overlaid with the first one but much weaker. This can be explained with a higher order mode which is only just beginning to be guided for this waveguide width. The fields of this mode have a large overlap with areas outside of the waveguide and are thus subject to high losses resulting in the weaker signal.

3.2.8 Ring Resonators

We also want to measure the propagation loss in the waveguide. For this a ring resonator is well suited. This device is classically often used to filter a specific channel e.g. in telecommunication or in microwave systems [34] but also for enhancement or suppression of spontaneous emission in combination with the Purcell effect [53, 41], cavity opto-mechanics [24], electro-optic resonators [34] and strong coupling cavity QED [15]. A suitable device consists of a two-coupler-device as explained above and a waveguide forming a circle, which is situated close to the two-coupler-device with

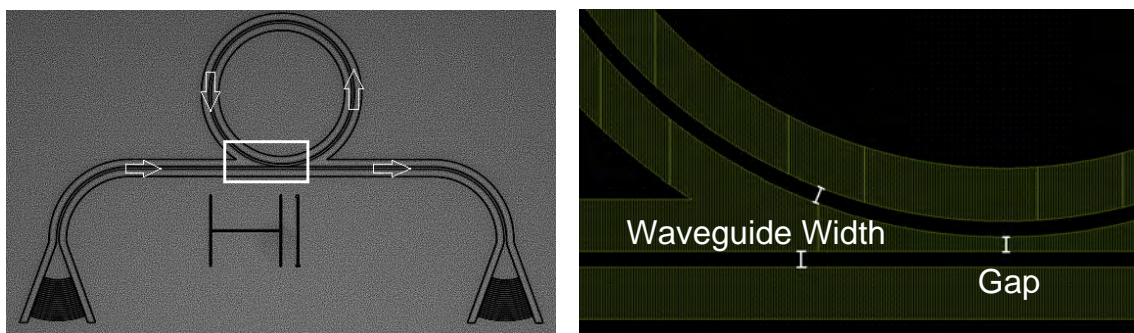


Figure 3.19: Ring resonators are used to estimate the transmission losses in a bended waveguide as well as the coupling strength depending on the gap and the width of the waveguides.

a gap in between. We use a bending radius of $40\ \mu\text{m}$ on the basis that in other materials losses increase drastically for a radius below $30\ \mu\text{m}$. For the real device used

in the experiment with the crystal we choose a bending radius of $50 \mu\text{m}$ to make sure there are no unnecessary losses and also because it is convenient for scaling the waveguide bending to the writing fields of the Jeol electron beam lithograph as described in section 3.2.4.

When light is coupled in via one of the grating couplers it propagates through the waveguide and couples to the ring resonator. This can be approximately described by point coupling at the point where the distance is minimal (see figure 3.19). Since the light in the ring resonator is forced on a closed loop it interferes with itself. The

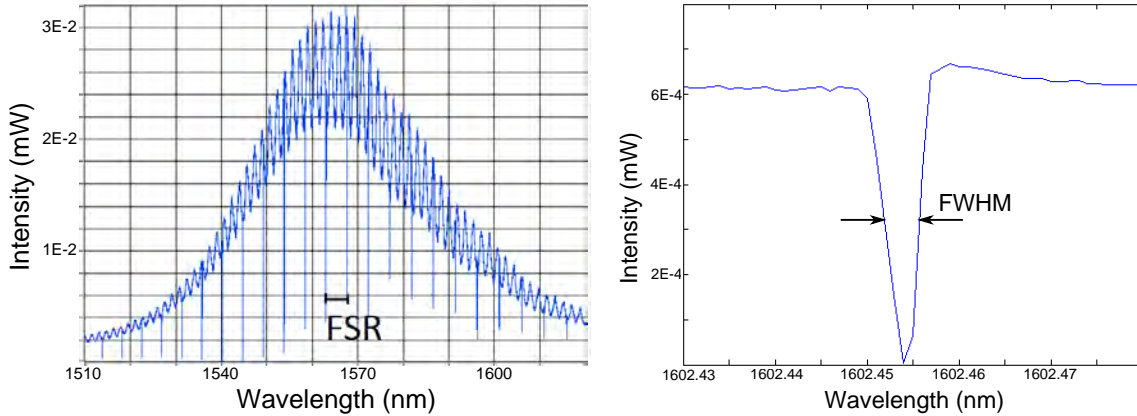


Figure 3.20: For every frequency at which the resonance condition is met, the transmission intensity shows an absorption peak. These peaks can be fitted with a Lorentzian and the quality factor can be obtained. They are also equidistant which is described by the free spectral range (FSR). The FSR can be used to calculate the absorption coefficient for a certain wavelength with the cavity's quality factor at that wavelength obtained from the full width half maximum (FWHM).

condition for standing waves is

$$2\pi R_{ring} = \frac{m\lambda}{2} \quad m \in \mathbb{N} \quad (3.12)$$

with the ring radius R_{ring} . If this is fulfilled we can observe an absorption peak that corresponds to coupling to the ring resonator.

The modes of such a cavity are called whispering gallery modes (WGM) [22], first observed as sound waves in the whispering gallery of St. Paul's Cathedral in London. Its quality factor is typically very large [51]. The quality factor is given by

$$Q = \frac{\lambda_0}{\text{FWHM}} \quad (3.13)$$

where FWHM is the full width half maximum of the Lorentzian that can be fitted to the absorption peak (see figure 3.20). λ_0 is the resonance wavelength of that peak. The best quality factor that we achieved so far is

$$Q_{max} \approx \frac{1602 \text{ nm}}{3.1 \text{ pm}} \approx 517\,000 \quad (3.14)$$

The free spectral range (FSR, figure 3.20), the distance between two absorption peaks, allows us to obtain an approximation of the absorption coefficient in the waveguide [16, 43]:

$$\alpha_{ring} = \frac{2\pi n_g}{Q\lambda_0} = \frac{\lambda_0}{Q \text{FSR} R_{ring}} \approx \frac{1602 \text{ nm}}{Q \cdot 5 \text{ nm} \cdot 40 \mu\text{m}} \approx -0.15 \frac{1}{\text{cm}} \approx -0.67 \frac{\text{dB}}{\text{cm}} \quad (3.15)$$

with the refractive group index n_g and the quality factor calculated in equation 3.14. Naturally, as this is the best quality factor we observe, the absorption coefficient in the actual device with the 6 cm long waveguide can be expected to be worse because we expect many more material defects in such a large structure.

3.2.9 Evanescent Field Coupling

How does the coupling to the ring resonator and also to the crystal on the chip actually work? In fact, it is both the same effect called attenuated total internal reflection. This happens due to the fact that there are evanescent waves penetrating through the interface into the adjoined material whenever total internal reflection happens. These evanescent waves appear to be traveling along the boundary inter-

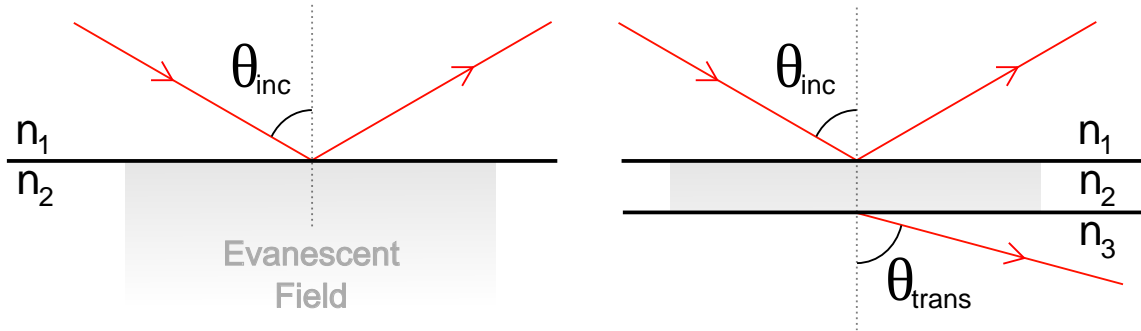


Figure 3.21: *Left*: total internal reflection with $n_1 > n_2$; an evanescent field penetrates the interface and decays exponentially but no energy is transferred.

Right: attenuated total internal reflection with $n_1 > n_3 > n_2$; after decaying exponentially the evanescent field also reaches the second interface and light is transmitted by tunneling through the small gap that is the middle medium.

face and are decaying exponentially in the direction perpendicular to the interface of the two materials. They can quickly be derived from total internal reflection:

$$\sin(\theta_{trans}) = \frac{n_1}{n_2} \sin(\theta_{inc}) \quad (3.16)$$

with $\theta_{crit} = \theta_{inc} = \arcsin(n_2/n_1)$ for $\theta_{trans} = 90^\circ$.

If we now consider an angle $\theta_{inc} > \theta_{crit}$ then this would lead to $\sin \theta_{trans} > 1$ and therefore $\cos \theta_{trans}$ becomes complex:

$$\cos \theta_{trans} = \sqrt{1 - \sin^2 \theta_{trans}} = i\sqrt{\sin^2 \theta_{trans} - 1} \quad (3.17)$$

The transmitted wave vector for a plane wave confined in the x-z plane is

$$\vec{k}_{trans} = k_{trans} \sin(\theta_{trans})\hat{x} + k_{trans} \cos(\theta_{trans})\hat{z} \quad (3.18)$$

Using $k_{trans} = \omega n_2/c$ the electric field of the transmitted plane wave is given by

$$\begin{aligned}\vec{E}_{trans} &= \vec{E}_0 e^{i(\vec{k}_{trans} \cdot \vec{r} - \omega t)} \\ &= \vec{E}_0 \exp \left[i(xk_{trans} \sin(\theta_{trans}) + zk_{trans} i \sqrt{\sin^2(\theta_{trans}) - 1} - \omega t) \right] \\ &= \vec{E}_0 e^{-\kappa z} e^{i(kx - \omega t)}\end{aligned} \quad (3.19)$$

where $\kappa = \omega/c \sqrt{(n_1 \sin(\theta_{inc}))^2 - n_2^2}$ and $k = \omega n_1/c \sin(\theta_{inc})$. Although there is a field in the second medium an energy transfer does not take place as the Poynting vector, if averaged over time, vanishes in the component perpendicular to the interface.

If, however, there is another medium very close to the first one with a refractive index n_3 so that $\theta_{inc} = \arcsin(n_3/n_1) < \theta_{crit}$ then light is indeed transmitted into that third medium (see figure 3.21). This is because the evanescent field, even though it decays exponentially perpendicular to the boundary surface, does penetrate into the third medium and the light tunnels through the small gap consisting of the middle medium with n_2 . In case of a ring resonator and the crystal on top of the waveguide in our experiment we call this evanescent coupling.

3.2.10 Gluing Single Fibers onto the Chip

In order to access the integrated waveguide we use grating couplers as explained in sections 3.2.6, 3.2.7. However, the method to actually place the fibers on top of these couplers proofs challenging for the setup in the cryostat. Initially, we intended to glue the fibers directly onto the couplers (figure 3.22), but we did not succeed. The idea was to deploy a bonding machine which is normally used to bond super-

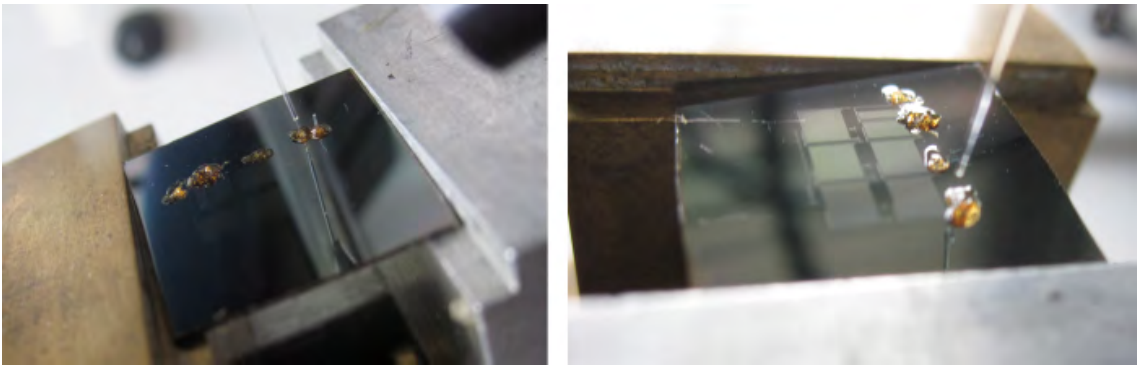


Figure 3.22: A bonding machine for superconducting wires was employed to try and glue single fibers onto the grating couplers. This was unsuccessful as the accuracy of placing the fibers is too low and the fibers are very fragile with a stripped off protection jacket.

conducting wires onto a chip. It contains a needle which can be moved electrically in a vertical direction and there is a stationary microscope on the bonding machine. We used a clamp to fix the fiber onto the needle and tried to glue it onto the coupler with GE Varnish, a widely used cryogenic glue, while utilizing the microscope for precise alignment.

However, after applying some glue onto a coupler it is very hard to still see the coupler clearly. The glue is not very transparent and it is near impossible to place the fiber perfectly in the middle of the coupler after applying the glue. An additional annoyance is the fragility of the fibers. They need to be prepared for good coupling efficiency. This includes stripping the protection jacket, cleaning them afterwards and cleaving off some of the fiber to achieve a high surface quality. Unfortunately, the fibers tend to break when stripped. The diameter of a stripped fiber is only $250\ \mu\text{m}$.

3.2.11 Gluing a Fiber Array onto the Chip

Another approach to align fibers to the grating couplers on the chip, albeit one that is rather more expensive, is to glue a whole fiber array onto the chip. This is very promising because we can measure the transmission while gluing. We use the

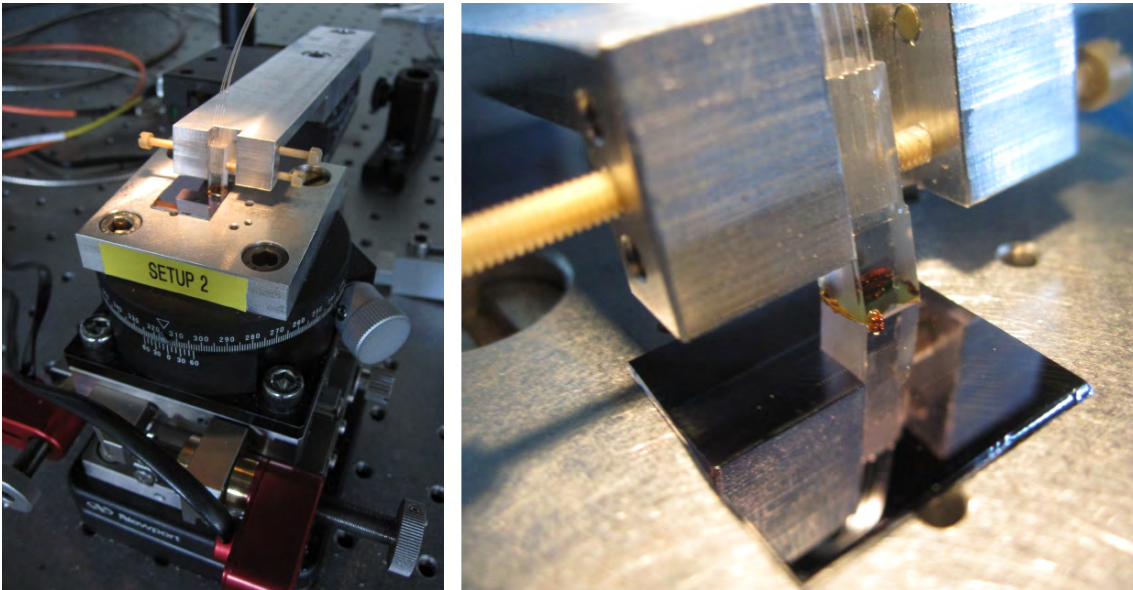


Figure 3.23: We now try to glue a whole fiber array onto the chip. This works much better because we can measure the transmission while gluing as we use the nanophotonic setup (see section 3.2.5) for alignment.

nanophotonic setup at the INT as discussed in section 3.2.5 to align the fiber array with the 3D piezo stage onto the couplers. We applied GE Varnish to the bottom surface of the fiber array after the alignment with the piezo stage.

The transmission intensity before applying the glue was about $T = 2 \cdot 10^{-4} \%$. Due to relaxations in the piezo stage and creeping of the glue while drying, the transmission intensity decreases and is now at around $T = 2.5 \cdot 10^{-5} \%$. While pressing the fiber array onto the chip with the applied glue, a small drop of glue appeared on the front side from under the fiber array, visible in the right picture in figure 3.23 on the left side of the fiber array. Unfortunately, it is directly above one of the grating couplers. When sweeping the laser frequency there were very heavy oscillations. That drop of glue seems to act as a very effective cavity, which leads to Fabry-Perot-like interferences (see figure 3.24). However, these interferences apparently do not affect the transmission at $1536\ \text{nm}$ and $1539\ \text{nm}$ where it is still $T = 2.5 \cdot 10^{-5} \%$.

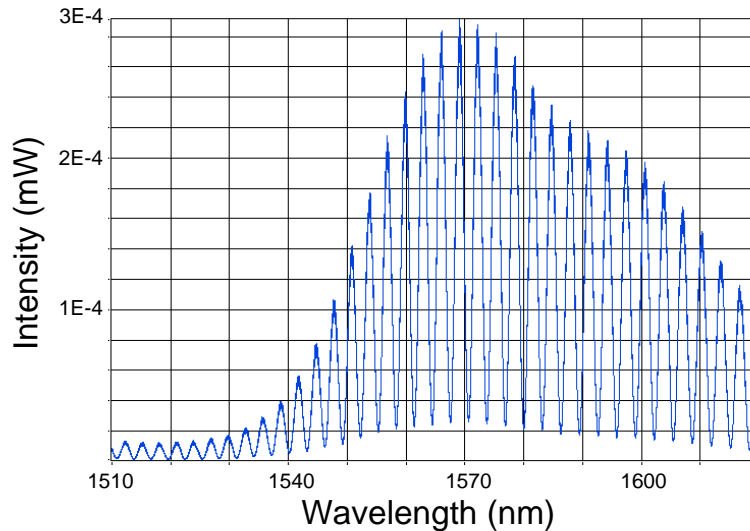


Figure 3.24: The transmission intensity drops when applying the glue compared to a perfectly aligned fiber array without any glue due to piezo relaxations and glue creeping as the glue dries over night. Transmission after gluing is $T = 2.5 \cdot 10^{-5} \%$. During gluing a drop of glue built over one of the couplers. This acts as a cavity giving rise to strong oscillations as can be seen in the transmission diagram.

In our experiment, in order to measure the full Zeeman split transitions, we sweep the laser frequency within a region of around 15 GHz. This means that we probably will not encounter any trouble here as the oscillation in figure 3.24 is about 10 periods per 30 nm and thus far broader than our sweep.

3.2.12 Sample Holder

The sample holder for the chip is depicted in figure 3.25. We need it to mount the chip with the crystal centrally within the pair of Helmholtz coils in the cryostat. In addition, it is important to connect the chip thermally to the coolest stage of the cryostat. Hence, we use copper to manufacture the sample holder. The chip is glued onto the bottom of the sample holder while the crystal is placed on top of the device and fixed in a good position by a teflon screw in the cover. Usually, by means of observing the interference fringes between chip and crystal, we can assess the gap between crystal and chip and place the crystal accordingly. However, when using a crystal with anti-reflection coating, such as the one in figure 3.25 this is not always possible. The fibers of the fiber array are guided out of the sample holder through the big hole in the cover of the sample holder. The sample holder is mounted in the middle of the Helmholtz coils in the cryostat (figure 3.26). The slits in the side walls of the sample holder can be used to access the crystal with an open laser beam. The optical windows of the cryostat are aligned with these slits. This might be useful for later experiments.



Figure 3.25: The chip with the fiber array is glued onto the bottom of the copper sample holder. Copper is necessary because of thermal conduction. A material which becomes superconducting has a comparably bad thermal conduction and can therefore not be used. The crystal is then placed on top of the chip and kept there by means of a teflon screw from the cover of the sample holder.

After installing the sample holder, we spliced the fibers of the fiber array with the ones installed in the cryostat. However, we do not see any transmission through the integrated waveguide any more. We checked the fibers that are installed in the cryostat and any other components that are involved to rule out other error sources. Probably, the glue did move a bit further which lead to weaker coupling. It seems that the glue does not dry completely during one night. We will attempt to remove the fiber array and try the gluing again. Unfortunately, the remaining time until the submission date is insufficient to report further developments in this thesis.

In hindsight, it may have been better to use a different coupler for the integrated waveguide. The grating couplers are excellent for fast characterization of many devices on a chip. However, we need permanent coupling to the waveguide. Also, a higher coupling efficiency would be advantageous. Therefore, the end-fire approach (see section 3.2.6) might be better suited for future experiments on coupling of an integrated waveguide to a rare earth doped crystal.

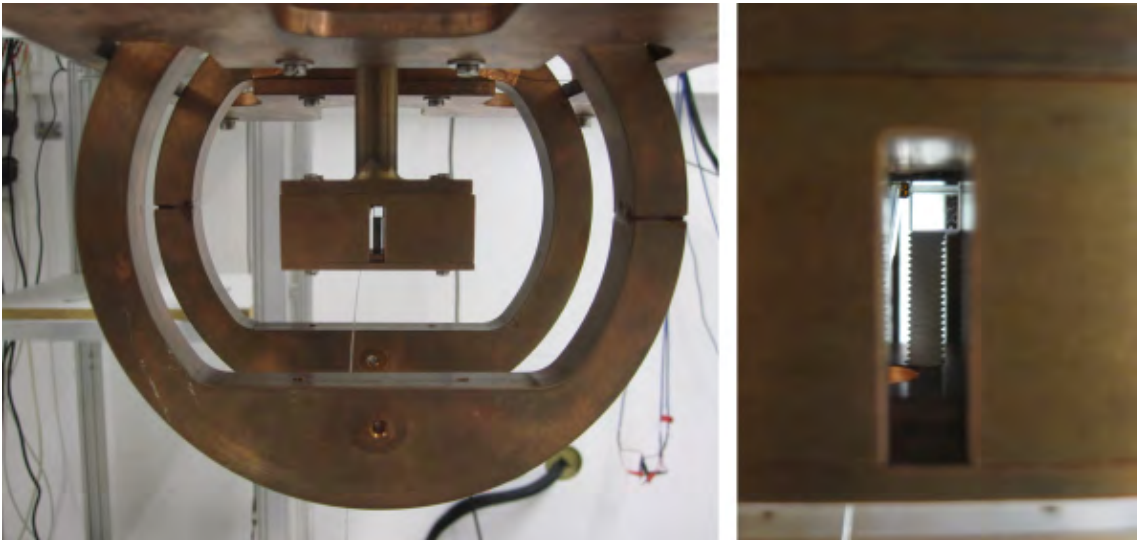


Figure 3.26: The sample holder is placed in the middle of the Helmholtz coils. It is upside down since the fibers are guided out of the sample holder through the cover. The slits in the side can be used in an open beam experiment and are aligned with the optical windows of the cryostat.

4 | Results, Evaluation & Discussion

In this chapter we present the evaluated data of our experiments and discuss and assess these results. We also clarify the employed methods of evaluation as well as estimate the errors of our measurements. The plots are created with Matlab. The fitting is done with the least squares method in Matlab, as well.

4.1 Zeeman Splitting

First, we present the data for the Zeeman splitting at 21 mK for each crystallographic site, which was taken for magnetic fields of up to 280 mT. By assigning the correct transition to each absorption peak, we can calculate the g-factors for the ground and the excited state for both crystallographic sites.

4.1.1 Crystallographic Site 1 (1536.48 nm)

The data for the Zeeman splitting was detected by continuously sweeping the laser frequency back and forth over the transitions. For site 1, we used a power of around $2 \mu\text{W}$. Post processing of the raw data was necessary to account for intensity oscillations due to our setup (see section 3.1). When optical fibers experience mechanical stress the refractive index of the material changes. Since this stress fluctuates slowly over time, the polarization of the light guided in the fiber will oscillate as well. Due to the polarization filter in front of the cryostat window the light intensity at the sample oscillates as well. Moreover, the sweeping of the laser frequency also causes a drop in intensity because the polarization in the fibers depends on the wavelength of the light.

In order to remove such intensity fluctuations in the data for different laser frequencies, we averaged over 100 data points at the beginning and the end of a sweep for each magnetic field value. These two points were used to draw a linear slope to the data. Then, each point was corrected relative to its position on the slope. This means, that the slope is now horizontal. This leads to a relatively constant intensity level for frequencies away from absorption peaks for one frequency sweep. To remove the time dependent intensity oscillations as well, we used the intensity for the first sweep as a reference to correct the intensity for all other sweeps. The remaining intensity fluctuations in the background are rather small.

Figure 4.1 shows the Zeeman splitting for site 1. We can clearly see six absorption

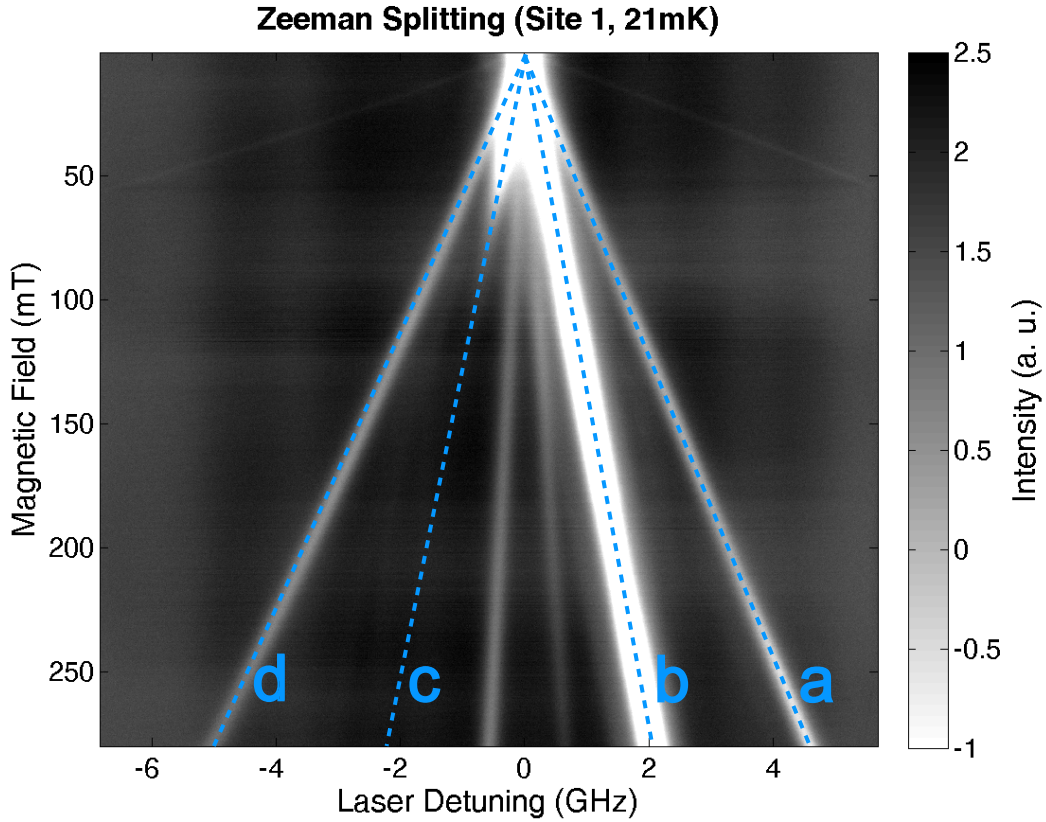


Figure 4.1: Of the expected eight transitions at site 1, six are clearly visible in this image. It is tricky to distinguish the different magnetic subclasses. We know that b is the strongest transition because a and d are suppressed since the angular momentum is not conserved. c and d should decrease with higher magnetic fields because the $|g \uparrow\rangle$ level depopulates due to the Boltzmann distribution. a and d have the highest and lowest transition energies, respectively, whereas b and c need not necessarily be in this specific order.

lines of the eight expected transitions for both magnetic subclasses. Now we want to assign the correct transitions to these absorption lines at least for the magnetic subclass where all four transitions are visible. This is somewhat tricky, especially to distinguish between the different magnetic subclasses. As a reminder the four transitions a to d as explained in the theory (section 2.1.1) are depicted in figure 4.2.

We know that the transition b must be the strongest transition. This is because it includes the lowest energy level $|g \downarrow\rangle$ which is always highly populated, especially at low temperatures. The upper Zeeman level of the ground state $|g \uparrow\rangle$, in contrast, suffers from depopulation for a rising magnetic field to the Boltzmann distribution of the population of the energy levels.

The second reason for b being the main transition are the selection rules. For the b and c transition the angular momentum is conserved. A photon carries an angular momentum of ± 1 in form of its polarization. When it gets absorbed by the electron of an erbium atom in the crystal, the angular momentum of the electron is changed

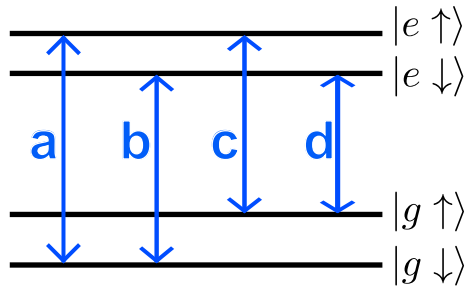


Figure 4.2: The four transitions for each crystallographic site and each magnetic subclass as discussed in section 2.1.1.

by 1 as it goes from the ground state to the first excited state. However, in the case of the a and d transition, the electron spin changes as well, which means the total change of the angular momentum is ± 2 or 0 and is not conserved any more. This leads to a lower transition probability compared to transitions with a conserved angular momentum.

Another indication for how to assign the transitions to the absorption lines is the transition energy. The transitions a and d are the ones with the largest and smallest transition energies, respectively. This is always true for this kind of level scheme, hence, for both crystallographic sites and both magnetic subclasses. The transitions b and c , however, are not necessarily in a specific order. This depends on whether the g -factor for the ground state or the one for the excited state is larger.

If we use these criteria appropriately, we now know why the transitions a , b and d are marked at their respective absorption line in figure 4.1. Transition c is more difficult to identify because we need to distinguish it somehow from the second magnetic subclass. We know that the relative intensity differences between the four transitions must be the same for both magnetic subclasses. The transition marked as c in figure 4.1 decreases in intensity very quickly. Therefore, it must be either a c or a d transition. Since its intensity is initially very high, it can only correspond to the c transition of the first magnetic subclass. Thus we have four transitions for the first magnetic subclass. The remaining two transitions (closest to 0 GHz laser detuning) belong to the other magnetic subclass.

The remaining two transitions are possibly the b transition at around -0.7 GHz laser detuning and the c transition (at $+0.8$ GHz) of the second magnetic subclass. This is because they should be stronger than the other transitions which are thus likely not visible here. Also, the left one does not decrease in intensity.

Having done the hard work, we can now determine the g -factors for the first magnetic subclass for the ground and the excited state at site 1. The g -factor for a certain energy level is given by the energy difference of the split levels and the applied magnetic field that causes this Zeeman splitting (section 2.1.5)

$$g_j = \frac{\Delta E_{m_j, m_{j-1}}}{\mu_B B} \quad (4.1)$$

with the Bohr magneton μ_B .

The g-factors for ground and excited state are given by

$$g_{ground} = \frac{E_a - E_c}{\mu_B B} = \frac{E_b - E_d}{\mu_B B} \quad (4.2)$$

$$g_{excited} = \frac{E_c - E_d}{\mu_B B} = \frac{E_a - E_b}{\mu_B B} \quad (4.3)$$

This is easy to comprehend by taking a look at the level scheme (figure 4.2) and reconstructing the actual energies that are calculated with the respective energy differences in the denominator of the fractions. It also gives us an additional method to check whether we correctly assigned the transitions to the absorption lines. Basically, this means the energy differences of the transitions $a-b$ and $c-d$ must be equal.

In figure 4.1 we determine the detuning frequencies at 280 mT for the four transitions of the first magnetic subclass: $E_a = 4.61$ GHz, $E_b = 2.05$ GHz, $E_c = -2.25$ GHz and $E_d = -5.08$ GHz. This results in the following g-factors for the ground and the excited state

$$\begin{aligned} g_{ground} &= \frac{E_a - E_c}{\mu_B B} = \frac{6.86 \text{ GHz}}{9.274 \cdot 10^{-24} \text{ J/T} \cdot 280 \text{ mT}} = 1.75 \\ &= \frac{E_b - E_d}{\mu_B B} = \frac{7.13 \text{ GHz}}{9.274 \cdot 10^{-24} \text{ J/T} \cdot 280 \text{ mT}} = 1.82 \end{aligned} \quad (4.4)$$

$$\begin{aligned} g_{excited} &= \frac{E_a - E_b}{\mu_B B} = \frac{2.56 \text{ GHz}}{9.274 \cdot 10^{-24} \text{ J/T} \cdot 280 \text{ mT}} = 0.65 \\ &= \frac{E_c - E_d}{\mu_B B} = \frac{2.83 \text{ GHz}}{9.274 \cdot 10^{-24} \text{ J/T} \cdot 280 \text{ mT}} = 0.72 \end{aligned} \quad (4.5)$$

where $1 \text{ GHz} = 6.626 \cdot 10^{-25} \text{ J}$ because the photon energy is $E = h \cdot \nu$ with the Planck constant $h = 6.626 \cdot 10^{-34} \text{ J/s}$ and the photon frequency ν .

The two values we calculated for the two g-factors of the ground state and the excited state are not identical but very similar. This is very comforting, it means we assigned the correct transitions to the different absorption lines. Surely, the difference originates from the error we introduce when trying to determine the value of the laser detuning frequency at 280 mT. This error should be less than 0.1 GHz.

There are also two other significant errors in this calculation. The first one owes something to the fact that we do not exactly know the sweeping range of the laser frequency. We estimate the range with the wavelength meter which is, unfortunately, a little bit too slow to detect the wavelength precisely when sweeping the frequency. The sweeping range for this measurement was about 13 GHz with an estimated error of 5%.

Since these two errors of the frequency are not correlated we can assume that they possibly cancel each other out to some degree. The Gaussian error propagation method is thus correct in this case. We will use the mean value for the result of the g-factors and also for the energy difference. This results in two different errors for the ground and the excited state g-factor

$$\sigma_{\Delta E}^{ground} = \sqrt{(0.1 \text{ GHz})^2 + (7.00 \text{ GHz} \cdot 5\%)^2} = 0.36 \text{ GHz} \quad (4.6)$$

$$\sigma_{\Delta E}^{excited} = \sqrt{(0.1 \text{ GHz})^2 + (2.70 \text{ GHz} \cdot 5\%)^2} = 0.17 \text{ GHz} \quad (4.7)$$

The uncertainty of the magnetic field is the last error which we consider significant for this experiment. We can only measure the electrical current running through the superconducting Helmholtz coils which is 8 A in this case. We estimate the magnetic field to be 35 mT per 1 A coil current based on a comparison of g-factors with a publication by Sun et al. [49]. The g-factor was measured with microwaves, hence only the g-factor for the ground state is known because the transition $|e \downarrow\rangle \leftrightarrow |e \uparrow\rangle$ is invisible due to very low population of the $|e \downarrow\rangle$ state at low temperatures. The error of the magnetic field in our case should be within 10%.

To determine the resulting error for the g-factors we use again the Gaussian error propagation for the uncorrelated errors of the laser frequency and the magnetic field

$$\begin{aligned} \sigma_g^{ground} &= \sqrt{\left(\frac{\partial g}{\partial \Delta E} \cdot \sigma_{\Delta E}\right)^2 + \left(\frac{\partial g}{\partial B} \cdot \sigma_B\right)^2} \\ &= \sqrt{\left(\frac{\sigma_{\Delta E}^{ground}}{\mu_B B}\right)^2 + \left(-\frac{\Delta E}{\mu_B B} \cdot \frac{\sigma_B}{B}\right)^2} \\ &= \sqrt{(0.092)^2 + (-1.79 \cdot 10\%)^2} \\ &= 0.201 \end{aligned} \quad (4.8)$$

$$\begin{aligned} \sigma_g^{excited} &= \sqrt{\left(\frac{\partial g}{\partial \Delta E} \cdot \sigma_{\Delta E}\right)^2 + \left(\frac{\partial g}{\partial B} \cdot \sigma_B\right)^2} \\ &= \sqrt{(0.043)^2 + (-0.69 \cdot 10\%)^2} \\ &= 0.081 \end{aligned} \quad (4.9)$$

The final results for the g-factors of the first magnetic subclass at site 1 for the ground and the excited state are then as follows

$$\underline{g_{ground} = 1.79 \pm 0.20} \quad (4.10)$$

$$\underline{g_{excited} = 0.69 \pm 0.08} \quad (4.11)$$

The g-factors are highly dependent on the orientation of the crystal. In the paper by Sun [49] the g-factor for the ground state of site 1 can vary between around 1.4 and 15. Therefore, our result of 1.79 for the ground state does not contradict Sun's results, however, it is also difficult to compare it as we do not know the orientation of our crystal precisely and have not conducted any experiments with varying crystal orientations. However, we are happy to report that the g-factor of the excited state for site 1, which corresponds to a ground state g-factor of 1.79 ± 0.20 , is 0.69 ± 0.08 .

4.1.2 Crystallographic Site 2 (1538.90 nm)

At site 2 the measurement was conducted in the same way. Here, a laser power of $25 \mu\text{W}$ was used. The data was also post processed to take intensity fluctuations

into account as described in the previous section. Figure 4.1 shows the measurement data. This time we can distinguish seven different absorption lines of the expected eight transitions. We will again only evaluate the data for one magnetic subclass.

It is interesting that the main transition b almost does not get shifted. The transitions c and d can also be assigned without much trouble. To assign the transition a

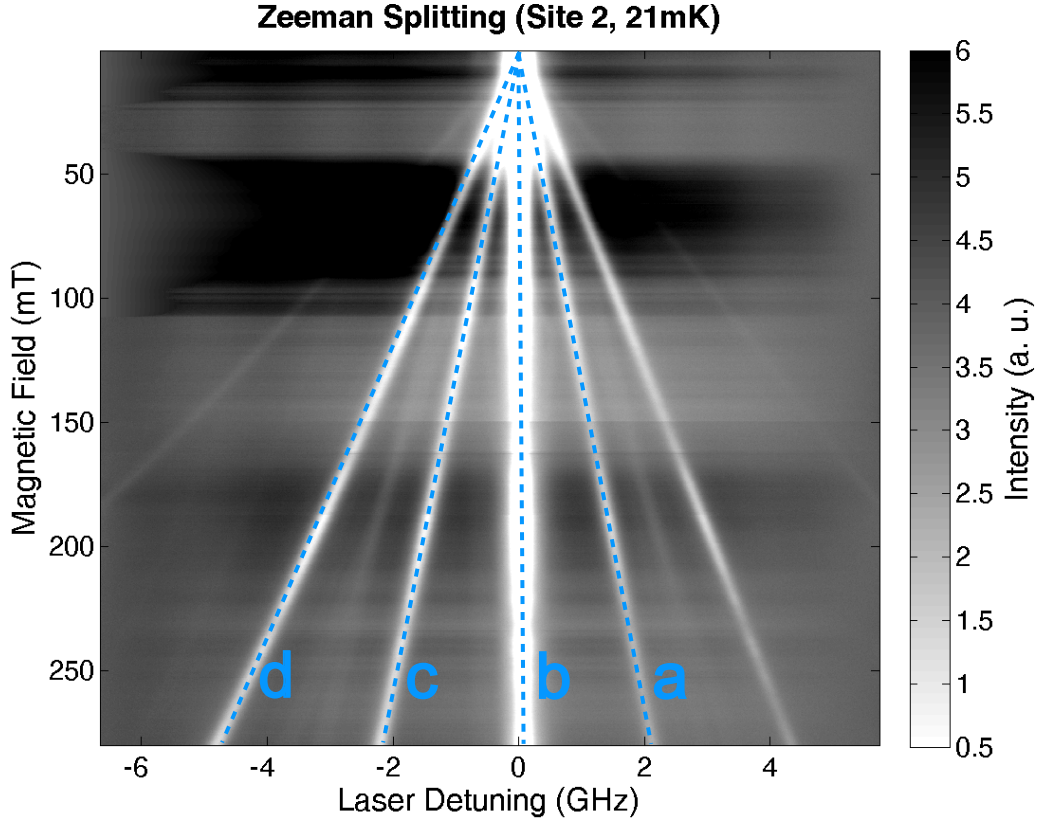


Figure 4.3: At site 2 we see seven transitions. The b transition almost does not get shifted compared to site 1. It is interesting that here the c transition almost does not decrease in intensity in contrast to what happens at site 1.

it is important to remember that the distance between the transitions a - b and the distance between c - d must be identical in order to be consistent with the theory. It thus follows that the transition on the far right at around 4.12 GHz (figure 4.1) cannot be the transition a of the first magnetic subclass. Instead, the four labeled transitions belong to the same magnetic subclass.

We find the frequency values for the four transitions of site 2 to be: $E_a = 2.05$ GHz, $E_b = 0.08$ GHz, $E_c = -2.10$ GHz and $E_d = -4.58$ GHz. The respective g -factors are

$$\begin{aligned}
 g_{ground} &= \frac{E_a - E_c}{\mu_B B} = \frac{4.15 \text{ GHz}}{9.274 \cdot 10^{-24} \text{ J/T} \cdot 280 \text{ mT}} = 1.06 \\
 &= \frac{E_b - E_d}{\mu_B B} = \frac{4.66 \text{ GHz}}{9.274 \cdot 10^{-24} \text{ J/T} \cdot 280 \text{ mT}} = 1.19
 \end{aligned} \tag{4.12}$$

$$\begin{aligned}
 g_{excited} &= \frac{E_a - E_b}{\mu_B B} = \frac{1.97 \text{ GHz}}{9.274 \cdot 10^{-24} \text{ J/T} \cdot 280 \text{ mT}} = 0.50 \\
 &= \frac{E_c - E_d}{\mu_B B} = \frac{2.48 \text{ GHz}}{9.274 \cdot 10^{-24} \text{ J/T} \cdot 280 \text{ mT}} = 0.63
 \end{aligned} \tag{4.13}$$

with the mean values $g_{ground} = 1.13$ and $g_{excited} = 0.57$.

The errors are the same as for site 1 and we calculate them in the same manner. This time the sweeping range of the laser frequency was 12.3 GHz. The resulting errors are

$$\sigma_{\Delta E}^{ground} = \sqrt{(0.1 \text{ GHz})^2 + (4.405 \text{ GHz} \cdot 5\%)^2} = 0.24 \text{ GHz} \tag{4.14}$$

$$\sigma_{\Delta E}^{excited} = \sqrt{(0.1 \text{ GHz})^2 + (2.225 \text{ GHz} \cdot 5\%)^2} = 0.15 \text{ GHz} \tag{4.15}$$

The Gaussian error propagation for the combined error of detuning frequency and magnetic field yields

$$\begin{aligned}
 \sigma_g^{ground} &= \sqrt{\left(\frac{\partial g}{\partial \Delta E} \cdot \sigma_{\Delta E}\right)^2 + \left(\frac{\partial g}{\partial B} \cdot \sigma_B\right)^2} \\
 &= \sqrt{(0.061)^2 + (-1.12 \cdot 10\%)^2} \\
 &= 0.128
 \end{aligned} \tag{4.16}$$

$$\begin{aligned}
 \sigma_g^{excited} &= \sqrt{\left(\frac{\partial g}{\partial \Delta E} \cdot \sigma_{\Delta E}\right)^2 + \left(\frac{\partial g}{\partial B} \cdot \sigma_B\right)^2} \\
 &= \sqrt{(0.038)^2 + (-0.50 \cdot 10\%)^2} \\
 &= 0.063
 \end{aligned} \tag{4.17}$$

The final results for the g-factors of the first magnetic subclass at site 2 are

$$\underline{g_{ground} = 1.13 \pm 0.13} \tag{4.18}$$

$$\underline{g_{excited} = 0.57 \pm 0.06} \tag{4.19}$$

The errors for these g-factors are rather large for site 1 and site 2 mostly due to a big uncertainty for the magnetic field. However, since the major contributions to the error in the magnetic field and the scale of the laser detuning are equal for both g-factors (ground and excited state), the relative difference of these g-factors should be much more accurate than the errors suggest.

The g-factors for site 2 are smaller than for site 1. This is due to the anisotropy of the two sites regarding the orientation toward an electromagnetic field. It could be used in the way that, for site 1, a smaller magnetic field is sufficient to tune the spin ensemble to a certain microwave frequency.

We notice one additional rather strange feature, which is visible in the measurement plots for both sites. The eight optical transitions are all confined to a frequency region of around 9 GHz at 280 mT for both sites. This was confirmed in another measurement which was conducted earlier where all eight transitions were

visible but unfortunately we had much less resolution in the axis of the magnetic field because no automated measurement script was used. Nonetheless, we do see two additional lines which split much stronger and seem to be symmetrical with respect to the detuning frequency. For site 2 they split about twice as strongly as the farthest transitions. For site 1 it may be as much as 5 to 10 times stronger. Frankly, we cannot explain these features. We are not aware of anything like this in the literature.

4.2 Photon Echo

The photon echo measurements allow us to determine T_1 and T_2 and characterize their dependence on the temperature and the magnetic field.

4.2.1 T_1 at 25 mK

The population decay time T_1 was measured with the 3PE pulse sequence as discussed in section 2.2.4. After this time the probability for the quantum state to still be in the excited energy level is $1/e$. By varying the waiting time T_W from around $100 \mu\text{s}$ to 4.5 ms between the second and third pulse and keeping the delay time t_{12} at $2 \mu\text{s}$ between the first two pulses constant, we get a decay in echo amplitude with increasing T_W . Fortunately, the data suggest that spectral diffusion does not have a major influence on the decay shape. The decay looks like a proper exponential decay, which lead us to fit the following function to the data:

$$I(T_W) = I_0 \exp\left(-\frac{2T_W}{T_1}\right) \exp\left(-\frac{4t_{12}}{T_2}\right) = I'_0 \exp\left(-\frac{2T_W}{T_1}\right) \quad (4.20)$$

with I'_0 as the 'effective' maximum echo intensity which takes the T_2 dephasing factor during the delay time t_{12} into account.

The result for site 1 at a temperature of 25 mK and a magnetic field of 280 mT is shown in figure 4.4. The blue line represents the fit, whereas the black circles correspond to the data points. As can be seen, the fitted function does describe the decay very well in terms of the overall shape. Although, there seems to be a high noise level and we have a few outliers.

The T_1 decay time and the standard error for this fit are $T_1 = 0.836 \text{ ms} \pm 0.096 \text{ ms}$. However, accurate assessment of the systematic error of our setup is challenging. The reason is that we have a setup that consists partly of fiber optics. This is very convenient in many ways, e.g., to direct the light from one optical table to the other. However, with respect to polarization stability it is less beneficial because there are slow oscillations of the polarization due to mechanical stress in the fibers. These oscillations do not disappear until weeks or even months after the setup installation. They lead to oscillations of the pulse intensity due to the polarization filter in front of the cryostat window.

A measurement for one set of data for a T_1 or T_2 decay takes about 20 to 30 minutes. During this time the intensity oscillation completes about two or three periods. The

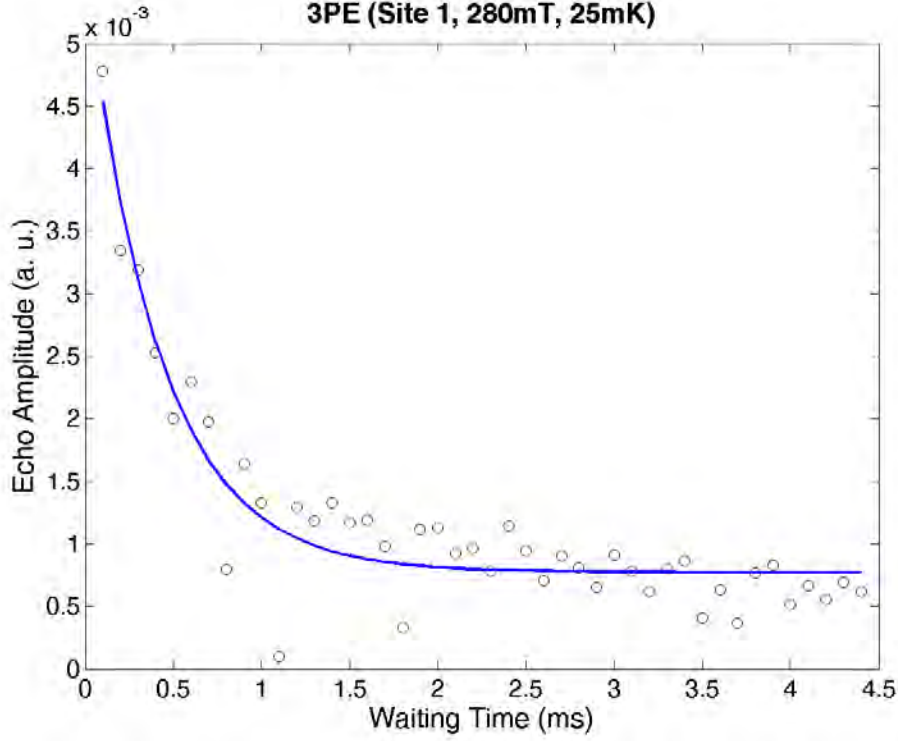


Figure 4.4: The population decay for site 1 at 25 mK and 280 mT. Spectral diffusion does not seem to affect the decay shape much, a simple exponential decay describes the data well. However, the noise is rather high and there are a few outliers. $T_1 = 0.836 \text{ ms} \pm 0.096 \text{ ms} \pm 0.043 \text{ ms}$. The systematic error (second one) is quite high as well due to intensity fluctuations caused by mechanical stress in the fibers which leads to polarization oscillations.

dependence of the echo intensity on the π - and $\pi/2$ -pulse intensities can be described by a squared sinus function

$$\frac{I_{echo}(I_{pulse})}{I} = \sin^2 \left(3 \cdot \frac{I_{pulse}}{I_{\pi/2}} \cdot \frac{\pi}{2} - \pi \right) \quad (4.21)$$

where I_{echo} is the measured echo intensity, I is the echo intensity for a real $\pi/2$ -pulse with the intensity $I_{\pi/2}$ and I_{pulse} is the intensity of the measured pulse. This is true because the echo intensity corresponds to the projection of the Bloch vector onto the xy-plane in the direction of the photon echo emission.

This means that fluctuations of as much as 20% in the $\pi/2$ -pulses lead to an echo intensity error of

$$\frac{\sigma_I}{I} = \frac{I_{echo}}{I} = \sin^2 \left(3 \cdot 0.8 \cdot \frac{\pi}{2} - \pi \right) = 34.5\% \quad (4.22)$$

We need to determine the error of T_1 , which must be smaller because we take many echo intensity data points into account for the fit. By applying the central limit theorem (CLT), we can approximate how the error of the echo intensity propagates even if we do not know the probability distribution exactly.

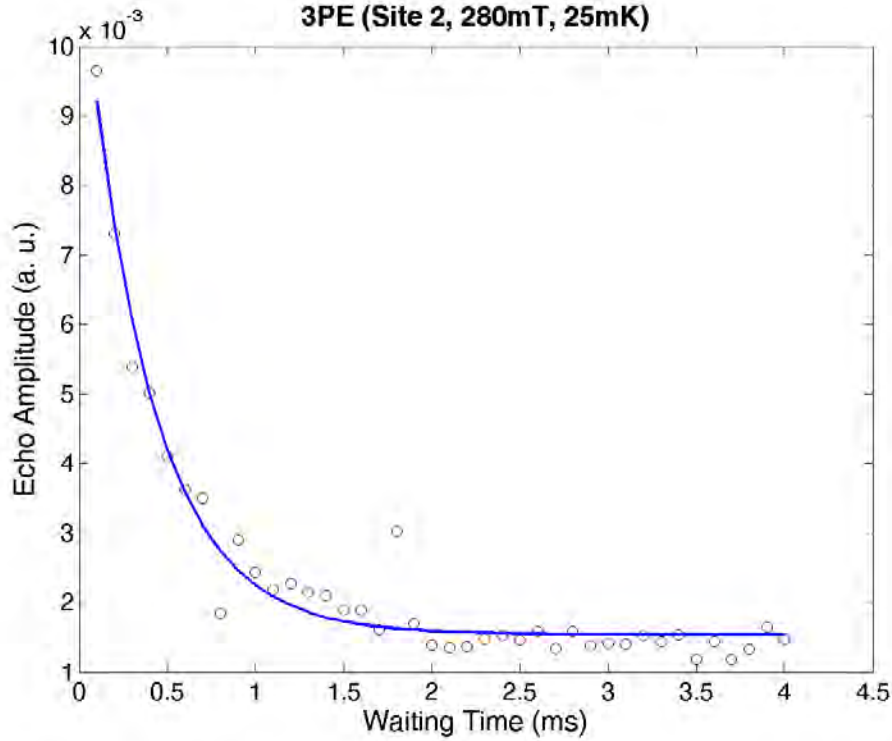


Figure 4.5: For site 2 the data looks similar but there is less noise. Matlab delivers a population decay time of $T_1 = 0.755 \text{ ms} \pm 0.052 \text{ ms} \pm 0.041 \text{ ms}$.

The CLT states that in this case

$$\bar{x} \pm \Delta x = \bar{x} \pm \frac{\sigma_x}{\sqrt{N}} \quad (4.23)$$

where N is the number of measurements. \bar{x} is the mean value of our parameter and σ_x is the standard error.

For site 1 we have 44 echo intensity data points. Hence, the systematic error is given by

$$\frac{\sigma_{T_1}}{T_1} = \frac{\sigma_{I_{echo}}}{\sqrt{N} I} = \frac{0.345}{\sqrt{44}} = 0.052 \quad (4.24)$$

which results in $\sigma_{T_1} = \pm 0.052 \cdot 0.836 \text{ ms} = 0.043 \text{ ms}$.

We tried to account for these fluctuations via evaluation arrangements since we did measure all the pulse intensities. However, our attempt to correct the fluctuations by measuring the echo and pulse intensities with a constant delay time and waiting time over a long period of time and then fit a squared cosine function did not work. A very high noise level of the data points did not allow the justification to perform this fit. Likewise, the attempt to correct the echo intensities at least linearly caused even larger statistical errors due to strong fluctuations in the data. Therefore we are content to simply estimate a systematic error without further corrections to the data.

Naturally, the best solution would be to use a polarization controller which is connected to a detector and can adjust the polarization automatically during the measurement. This will be taken into consideration for future measurements.

Thus we get a final result for the population decay for site 1 at a temperature of 25 mK and a magnetic field of 280 mT for the main transition (*b*-transition for the first magnetic subclass) with the statistical and the systematic error, respectively

$$\underline{T_1 (\text{Site 1, 25 mK, 280 mT}) = 0.836 \text{ ms} \pm 0.096 \text{ ms} \pm 0.043 \text{ ms}} \quad (4.25)$$

For site 2 the result looks similar, although there are fewer fluctuations which leads to a better fit (see figure 4.5). There are still a couple of outliers. Matlab provides a decay time of $T_1 = 0.755 \text{ ms} \pm 0.052 \text{ ms}$. The systematic error can be determined in the exact same way as for site 1 with $\sigma_{T_1}/T_1 = 0.345 \cdot 1/\sqrt{40} = 0.055$. The resulting population decay time for site 2 at 25 mK and 280 mT is

$$\underline{T_1 (\text{Site 2, 25 mK, 280 mT}) = 0.755 \text{ ms} \pm 0.052 \text{ ms} \pm 0.041 \text{ ms}} \quad (4.26)$$

4.2.2 T_2 at 25 mK

The data for the 2PE measurements can be evaluated in much the same way as for 3PE. The decay shape looks like a normal exponential decay which leads us to the conclusion that, once again, spectral diffusion apparently does not influence the T_2 in a drastic way. Thus, we can fit the following function as explained in section 2.2.3

$$I(t_{12}) = I_0 \exp\left(-\frac{4t_{12}}{T_2}\right) \quad (4.27)$$

with the delay time t_{12} between the $\pi/2$ -pulse and the π -pulse which was varied between around $1.4 \mu\text{s}$ and $10 \mu\text{s}$.

Figure 4.6 shows the data for site 1 with the fitted function. We can see very strong oscillations in the decay, which most probably correspond to coupling to the nuclear spin of neighboring yttrium, silicon and oxygen atoms. However, the overall exponential shape is still clearly visible. We will investigate these oscillations further in the next section. The fit with Matlab delivers a dephasing time at site 1 of $T_2 = 12.10 \mu\text{s} \pm 1.38 \mu\text{s}$.

T_2 is about two orders of magnitude smaller than T_1 . This is very common for rare earth doped crystals. Generally, T_2 is limited by T_1 as described in section 2.2.4. However, at very low temperatures the phonon interaction processes that usually govern T_1 cease to take place due to the lack of phonons. At this point the T_1 decay time gets much larger. Now, the main dephasing process for T_2 is no the T_1 limitation but spin-spin interactions. Hence, T_2 is much smaller than T_1 at milli-Kelvin.

The systematic error due to the intensity fluctuations can be estimated in the same way as for T_1 with the same fluctuations of the pulse intensity of about 20%. However, for T_2 we have more data points which will result in smaller systematic errors. For both sites we have 90 echo intensity data points. Thus, the systematic error is

$$\frac{\Delta T_2}{T_2} = \frac{\sigma_{I_{echo}}}{\sqrt{N} I} = \frac{0.345}{\sqrt{90}} = 0.036 \quad (4.28)$$

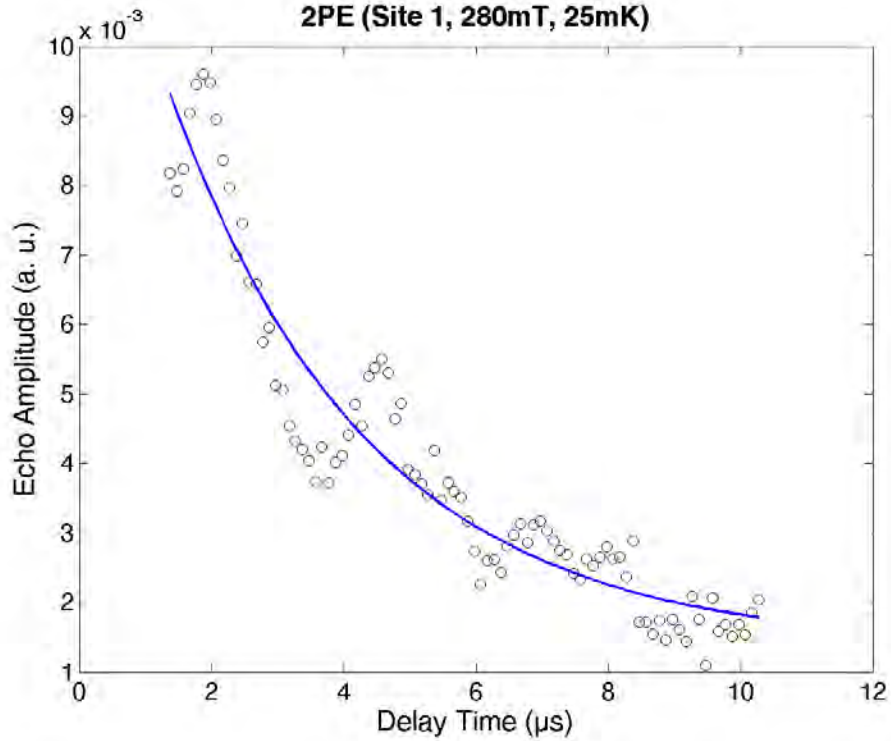


Figure 4.6: The 2PE dephasing for site 1 at 25 mK and 280 mT delivers $T_2 = 12.10 \mu\text{s} \pm 1.38 \mu\text{s} \pm 0.044 \mu\text{s}$. There are very strong cosine like oscillations in the decay shape which correspond to coupling between the nuclear spins of the erbium atom and neighboring atoms.

which results in $\sigma_{T_2} = \pm 0.036 \cdot 12.10 \mu\text{s} = 0.44 \mu\text{s}$ for site 1.

The final result for site 1 at 25 mK and 280 mT is

$$\underline{T_2 (\text{Site 1, 25 mK, 280 mT}) = 12.10 \mu\text{s} \pm 1.38 \mu\text{s} \pm 0.044 \mu\text{s}} \quad (4.29)$$

Figure 4.7 shows the data for site 2. The oscillations due to coupling to the nuclear spin of neighboring atoms are much smaller than at site 1 which means the fit is obviously much better. It delivers a dephasing time of $T_2 = 8.71 \mu\text{s} \pm 0.38 \mu\text{s}$ where the statistical error is smaller compared to site 1. The systematic error for site 2 is $\sigma_{T_2} = \pm 0.036 \cdot 8.71 \mu\text{s} = 0.31 \mu\text{s}$ which leads to a result of

$$\underline{T_2 (\text{Site 2, 25 mK, 280 mT}) = 8.71 \mu\text{s} \pm 0.38 \mu\text{s} \pm 0.31 \mu\text{s}} \quad (4.30)$$

We note that both T_1 and T_2 are larger for site 1 than for site 2. This is not necessarily trivial as the transition energy at site 1 with 1536.48 nm is larger than at site 2 with 1538.90 nm. We might generally expect the quantum state with the larger transition energy to decay faster. However, this is not true for all systems. It depends on the decay mechanisms and, while spontaneous emission is higher for larger transition energies, this is apparently not a major decoherence effect.

4.2.3 Oscillations in the T_2 Dephasing at 25 mK

The oscillations in the 2PE measurements stem from coupling to the nuclear spins of neighboring atoms, mostly yttrium and oxygen. First, we try to fit the product of the exponential decay and a cosine function (see figure 4.8) to the data for site 1

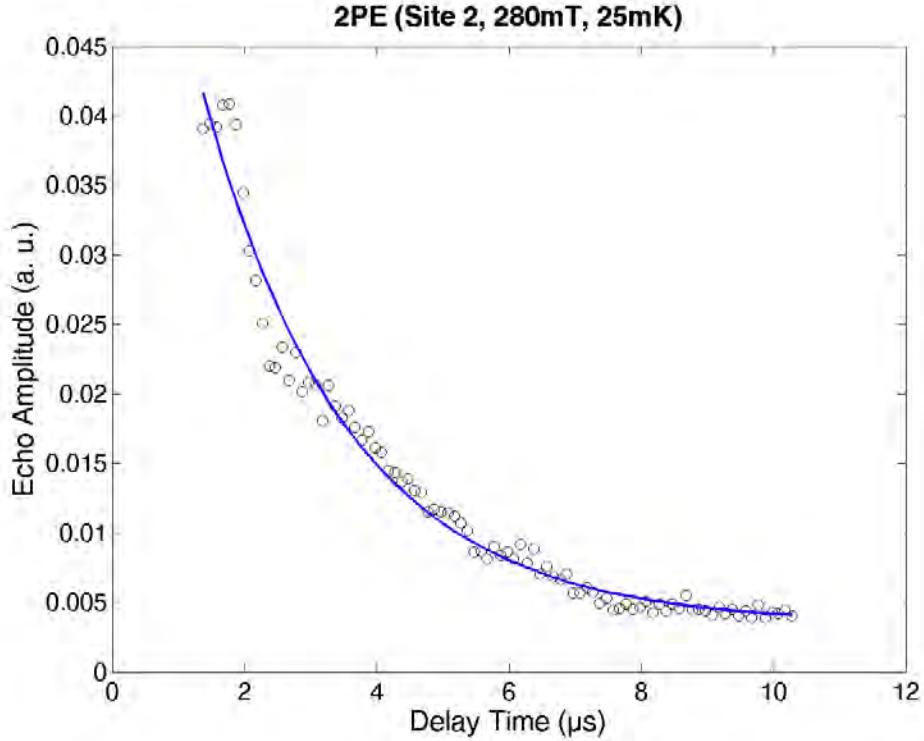


Figure 4.7: For site 2 the 2PE dephasing produces $T_2 = 8.71 \mu\text{s} \pm 0.38 \mu\text{s} \pm 0.31 \mu\text{s}$, a slightly smaller dephasing time than for site 1. The oscillations are much weaker.

$$I(t_{12}) = I_0 \cdot (a_0 + a_1 \cos(2\pi f + \phi)) \cdot \exp\left(-\frac{4t_{12}}{T_2}\right) \quad (4.31)$$

The result is somewhat unsatisfying because the fit does not really describe the data very well. This is mostly due to the fact that the oscillation seems to consist of several different frequencies, which makes it difficult to describe it with a single cosine function. For this fit we received the following parameter values: $T_2 = 11.99 \mu\text{s} \pm 0.84 \mu\text{s}$ and $f = 358 \text{ kHz} \pm 7 \text{ kHz}$.

To find out more about the involved frequencies we conduct a fast Fourier transformation (FFT) of the data. The result is depicted in figure 4.9. The exponential decay becomes a Lorentz function when Fourier transformed. However, due to the y-axis range the Lorentzian is barely visible in the plot. There are many frequencies and they are almost equidistant. The first 3 are at 152 kHz, 271 kHz and 372 kHz, whereas the last one of these seems to be the strongest one and is very close to the one that was used in the fit. It is difficult to actually assign these frequencies to the coupling of a specific neighbor atom. But the coupling depends on the distance to the neighbor atoms and should scale as $1/r^3$. The strongest coupling should be to the yttrium atoms' nuclear spin.

Even though for site 2 the oscillations are much weaker, we can still perform a FFT (figure 4.10). Here, the first frequency of 152 kHz was only vaguely visible and was left out of the y-range. This is because of the smaller T_2 time. Therefore, the Lorentz function is broader. Of course, it is also because for site 2 the oscillations are weaker. The other two frequencies mentioned above, however, are also visible

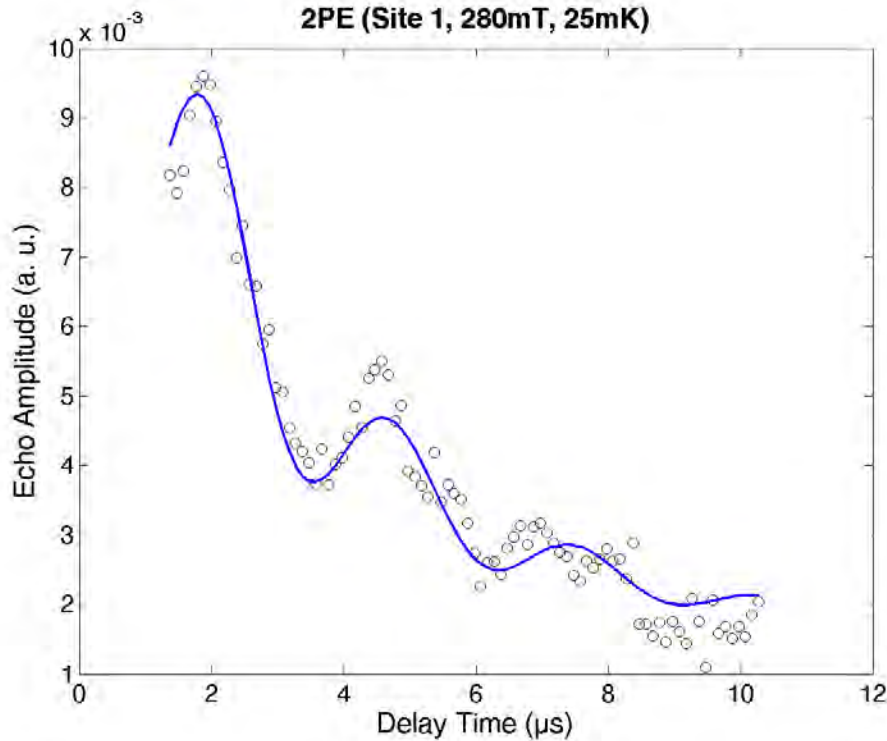


Figure 4.8: Fitting the product of the exponential decay and a cosine function does not really work because of many different frequencies are involved. Each frequency corresponds to coupling to the nuclear spin of a different atoms, mostly yttrium and oxygen. Nonetheless, the prevalent frequency seems to be at around 358 kHz.

here. At 262 kHz and 383 kHz they are a little bit shifted, yet clearly distinguishable. They are likely to correspond to the nuclear spins of the same neighbors as the respective ones for site 1. The relative peak intensities are also different as the peak for 383 kHz is not really stronger than for 262 kHz, which was the case for site 1.

4.2.4 T_1 versus Temperature

Now, we want to investigate the temperature dependence of T_1 . We are able to set the temperature in our cryostat up to 5 K. From 1 K to 5 K we measured in steps of 500 mK. Below that in steps of 200 mK. We waited several minutes after reaching each temperature before starting the measurement to make sure the sample holder and the crystal have actually reached that temperature.

The data is plotted in a double-logarithmic scale since this should give us some clues as to where any additional mechanism starts to affect the population decay. As we can see in figure 4.11, T_1 for site 1 seems to be pretty stable at around 1 ms up to 600 mK. Then it begins to decrease rapidly down to 0.011 ms at 4 K. At 4.5 K we have an outlier. At 5 K we could not fit a decay function to the data due to a very high noise level. The errors of the data points consist of the standard errors of the fit plus the systematic error due to the intensity fluctuation.

The plot for site 2 (figure 4.12) looks similar and without any outliers. However, at

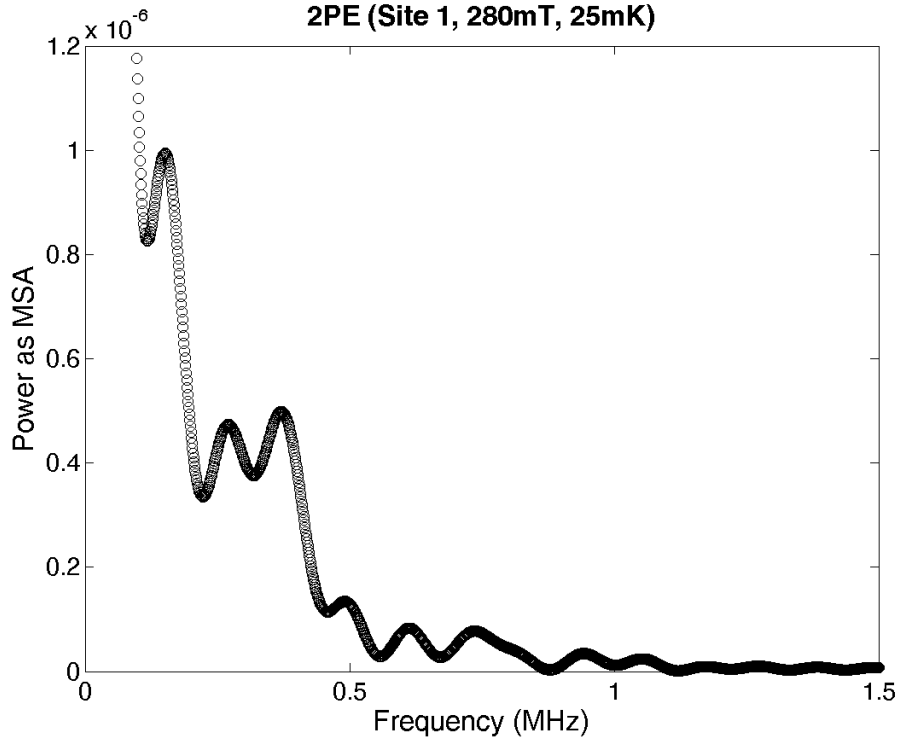


Figure 4.9: To investigate all the frequencies that contribute to the oscillations at site 1 we do a fast Fourier transformation (FFT) of the data. Apart from the Lorentz function which is the Fourier transform of the exponential decay we get quite a few frequency peaks. The first three are the strongest at 152 kHz, 271 kHz and 372 kHz.

5 K we could not retrieve a T_1 value either. The overall tendency is the same with T_1 being relatively stable at around 0.5 ms up to 600 mK. Then, it starts to drop off quickly down to 50 μ s at 4.5 K.

It seems that at 600 mK another decay mechanism starts to influence T_1 . This is most probably the coupling of the erbium electron to phonons. It is suppressed at very low temperatures because of the lack of phonons.

4.2.5 T_2 versus Temperature

The 2PE measurements were also conducted for different temperatures. Here, we see even better that, after a certain period of almost constant dephasing time, a new mechanism adds an additional decay channel. This leads to a different slope in the double-logarithmic plot for higher temperatures. For site 1 (figure 4.13) T_2 is between 10 μ s and 15 μ s below 3 K. Above that temperature it drops down to around 2 μ s for 5 K. The errors of the data points are again the sum of standard error from the fit and systematic error due to the intensity instability.

The plot for site 2 (figure 4.14) looks almost identical. The drop-off happens at 3 K, as well, but this time from around 5 μ s to 10 μ s down to 2 μ s at 5 K.

The behavior is very similar to the tendency seen in the T_1 plots. For T_2 it can

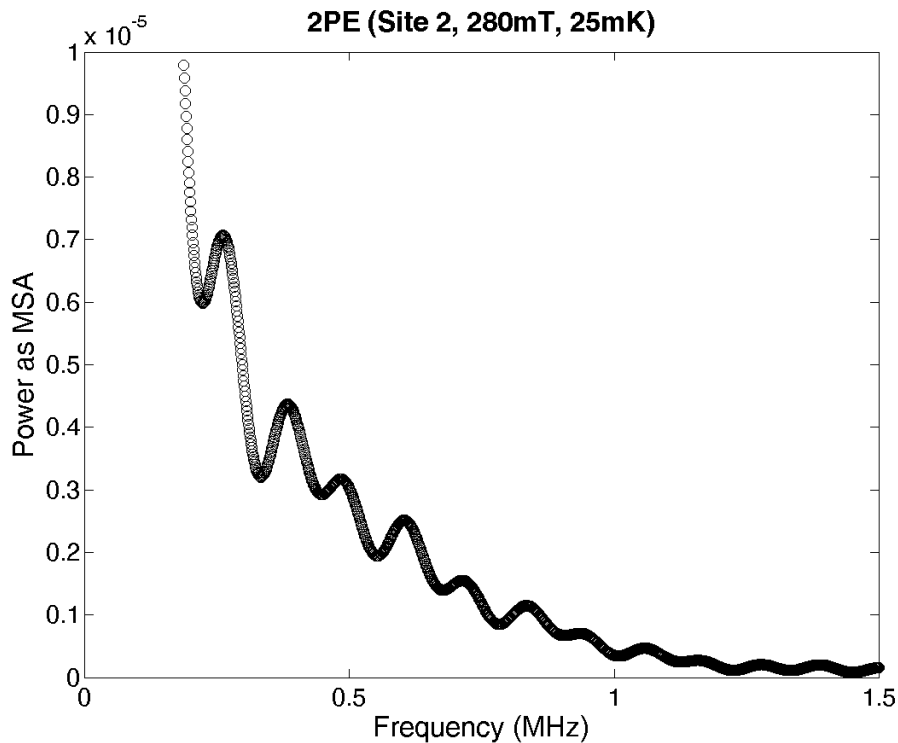


Figure 4.10: For site 2 the Fourier transform delivers a similar picture. The first frequency, even though existent, is very weak. The other two are slightly shifted at 262 kHz and 383 kHz compared to the site 1 results.

be explained as follows. Below 3 K the T_2 dephasing time is suppressed due to spin-spin coupling. This is approximately independent of the temperature. However, at higher temperatures T_2 is limited by T_1 . This is because the T_1 decay time decreases very fast with temperature due to the coupling to phonons. This means that above 3 K the two coherence times are similar. Since the optical T_2 dephasing time is the limiting factor for the conversion pulse scheme, it is sufficient to work at temperatures below 3 K with respect to the coherence times. However, the population of the energy states in thermal equilibrium is another story. Further examination is needed to assess whether the larger population of the higher Zeeman level at 3 K has a negative influence on the conversion.

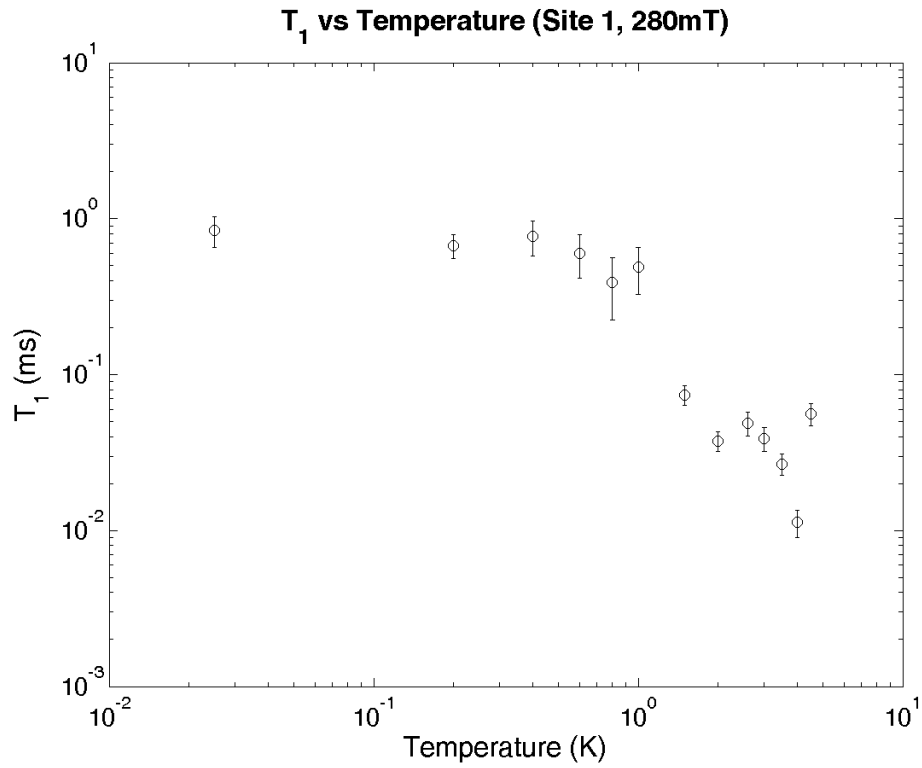


Figure 4.11: In a double-logarithmic plot we see that T_1 for site 1 is stable at first up to 600 mK but then drops quickly from around 1 ms to 0.011 ms at 4 K as the coupling to phonons starts to contribute to the population decay.

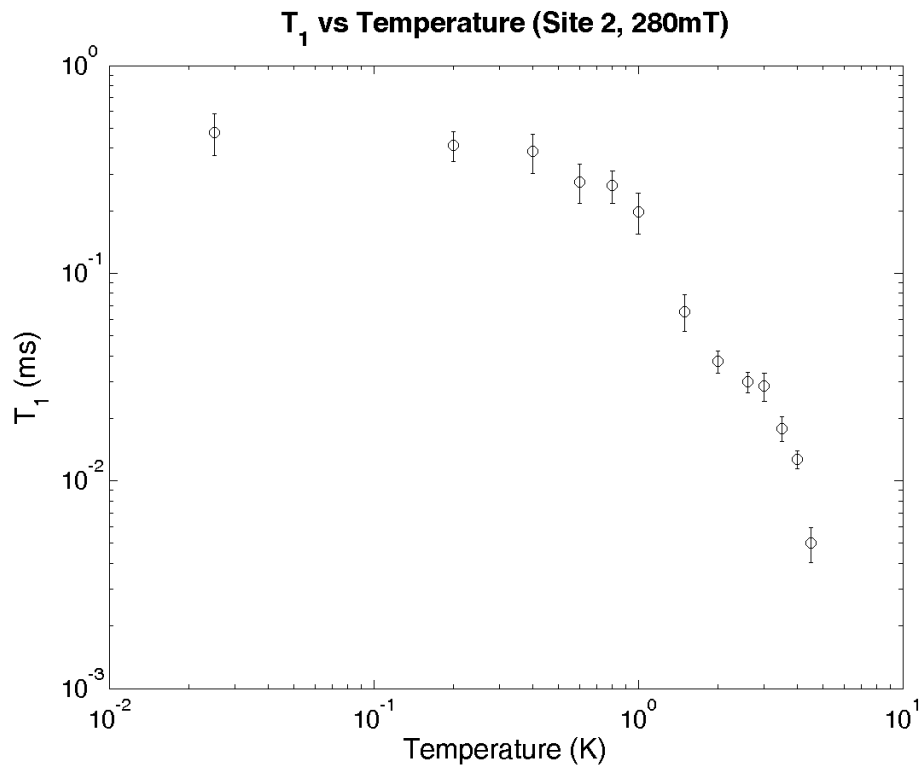


Figure 4.12: T_1 is only around 0.5 ms below 600 mK. Above that, it decreases rapidly until it reaches 50 μ s at 4.5 K due to phonon interactions.

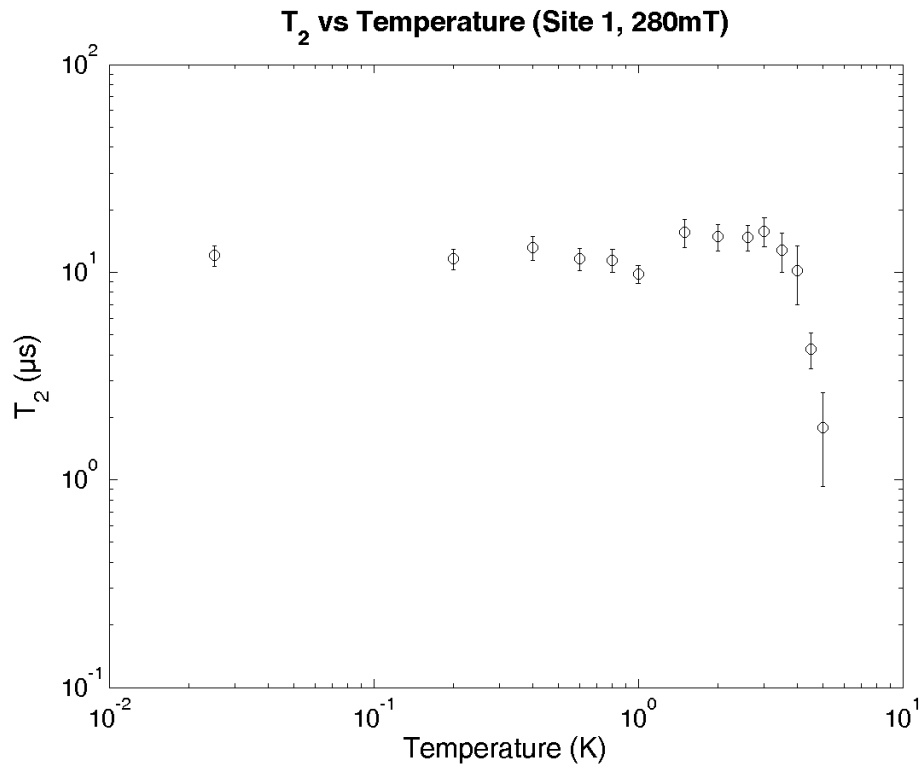


Figure 4.13: For T_2 the temperature dependence looks quite similar to T_1 . At site 1 it is relatively constant at around $10 \mu\text{s}$ to $15 \mu\text{s}$. However, at 3 K T_2 drops very quickly down to $2 \mu\text{s}$ at 5 K. This is because the T_1 limitation kicks in as T_1 decreases due to the coupling to phonons.

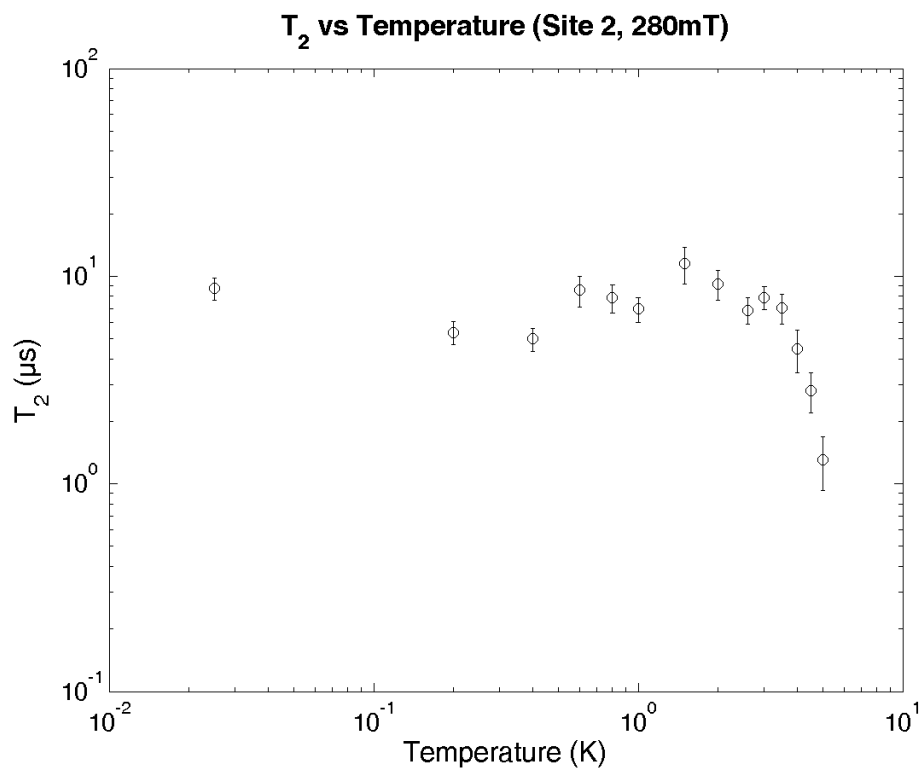


Figure 4.14: For site 2, T_2 is stable at around $5 \mu\text{s}$ to $10 \mu\text{s}$ below 3 K. Then, it drops down to $2 \mu\text{s}$ at 5 K because it is T_1 limited.

5 | Summary

Finally, let us recap what the purpose of this thesis is, how we tried to achieve it here and what the results showed. The aim of this project is to construct a coherent quantum converter which would be of great benefit to quantum computation and quantum communication. Qubits are generally considered promising candidates for quantum processing units. They are quantum two level systems and work in the microwave (MW) regime. However, in order to transmit quantum information over long distances to connect several of such processing units, microwave photons are badly equipped since the transmission losses are quite high. Near-infrared (NIR) photons are much superior in that regard and are already widely-used for classical optical communication in optical fibers, e.g., for web and telephone communication across the Atlantic. The idea is to use $\text{Er}^{3+}:\text{Y}_2\text{SiO}_5$ because it couples to both energy regimes. The first electronic excitation lies in the NIR regime and through Zeeman splitting we can tune the ground state to an arbitrary MW energy.

First, we probe the electron transitions optically. Assuming that the g-factors for ground and excited state are not identical, we expect four optical transitions when we apply a magnetic field. However, erbium is located at two different crystallographic sites with the transition energies of 1536.48 nm and 1538.90 nm. On top of that there are two nonequivalent magnetic subclasses, which means that we should actually see eight optical transitions at each site; four transitions per magnetic subclass and crystallographic site.

The experimental setup to measure the Zeeman splitting includes one of our NIR diode lasers by Toptica. The laser frequency can be swept back and forth by a piezo element. The maximum sweeping range is about 15 GHz, which is enough to detect all transitions at one site. The light is first coupled into optical fibers by means of a beam collimator to guide the beam to the optical table around the cryostat. There the light passes a polarization filter before it is directed through the optical windows of our cryostat with a base temperature of around 25 mK. It is focused on the crystal inside a sample holder, which is situated in the center of a pair of Helmholtz coils. We can generate magnetic fields of up to 280 mT with those Helmholtz coils. Afterwards, we detect the signal with a ThorLabs photo detector.

We see six absorption lines at site 1 and seven at site 2. By assigning the proper transitions to each absorption line for at least the first magnetic subclass, we can calculate the g-factors for the ground and the excited state. For site 1 we find $g_{\text{ground}} = 1.79 \pm 0.20$ and $g_{\text{excited}} = 0.69 \pm 0.08$, while for site 2 they are a bit smaller; $g_{\text{ground}} = 1.13 \pm 0.13$ and $g_{\text{excited}} = 0.57 \pm 0.06$. The errors stem mainly from the

uncertainty of the laser sweeping frequency range and the applied magnetic field.

The next step is to measure the actual coherence times of the optical quantum states in the erbium crystal. This is crucial for the development of a quantum converter as it limits the pulse sequence time for the coherent quantum conversion. To do this, we excite so called photon echoes. They are also used in a similar fashion for electron spins and nuclear spins, e.g., in magnetic resonance imaging (MRI). The photon echo intensity amplitude depends on the waiting time and the delay time of the 3PE and 2PE pulse sequences, respectively. By fitting an exponential decay to the data, we can determine the coherence times T_1 and T_2 . To realize this we use acousto-optic modulators (AOM) in order to generate the laser pulses.

We measured T_1 and T_2 at both crystallographic sites for the main transition (lower ground level to lower excited level) at 25 mK and 280 mT. For site 1 we have $T_1 = 0.836 \text{ ms} \pm 0.096 \text{ ms} \pm 0.043 \text{ ms}$ and $T_2 = 12.10 \mu\text{s} \pm 1.38 \mu\text{s} \pm 0.44 \mu\text{s}$. For site 2 it is a bit smaller with $T_1 = 0.755 \text{ ms} \pm 0.052 \text{ ms} \pm 0.041 \text{ ms}$ and $T_2 = 8.71 \mu\text{s} \pm 0.38 \mu\text{s} \pm 0.31 \mu\text{s}$. Spin-spin interactions limit T_2 and cause the high coherence time difference compared to T_1 . We notice strong oscillations in the exponential dephasing T_2 at site 1, and less strong at site 2. These correspond to interactions with the nuclear spins of neighbor atoms, mostly yttrium and oxygen. The prevalent frequencies are 152 kHz, 271 kHz and 372 kHz. In the double-logarithmic plots of T_1 and T_2 over temperature we see that the coherence times are rather stable at first, but drop drastically for higher temperatures. For T_1 the threshold temperature is around 600 mK for both sites. At this point coupling to phonons starts playing a role and causes much smaller T_1 times. T_2 drops at around 3 K due to the T_1 limitation.

Additionally, we intend to demonstrate coupling of an integrated waveguide to the erbium crystal. Therefore, we fabricate an integrated meander-like waveguide in a Si_3N_4 chip and place the crystal on top of that waveguide. The light in the waveguide should then couple to the erbium electrons by means of evanescent field coupling. The positive photo resist ZEP 520A is used to create an etching mask for reactive ion etching by electron beam lithography. The light is coupled into the integrated waveguide through grating couplers on which we glued a fiber array to ensure good alignment. Transmission is about $T = 2.5 \cdot 10^{-5}$.

The glue seems to have crept during drying. Alas, we do not see any transmission after having installed the sample holder in the cryostat. The gluing will be tried again to demonstrate the coupling to an integrated waveguide.

6 | Conclusions

In conclusion, we successfully measured the optical transitions of $\text{Er}^{3+}:\text{Y}_2\text{SiO}_5$ introduced by Zeeman splitting. We found the g-factors for the first magnetic subclass to be around $g_{ground}^1 = 1.79$, $g_{excited}^1 = 0.69$ for the crystallographic site 1 and $g_{ground}^2 = 1.13$, $g_{excited}^2 = 0.57$ for site 2. Furthermore, we determined the optical coherence times for the main transitions via photon echo at 25 mK and 280 mT, which are about $T_1 = 0.836$ ms, $T_2 = 12.10$ μs for site 1 and $T_1 = 0.755$ ms, $T_2 = 8.71$ μs for site 2. T_2 is limited by spin-spin interactions at low temperatures. At site 1 there are heavy oscillations in the T_2 dephasing due to interaction with the nuclear spins of neighboring atoms, mainly yttrium and oxygen. The main frequencies are 152 kHz, 271 kHz and 372 kHz. The temperature dependence of the coherence times is such, that at around 600 mK T_1 drops drastically due to the coupling to phonons. T_2 drops at 3 K due to the T_1 limitation, which is then dominant over the spin-spin coupling. The limiting factor for the coherent conversion scheme is the optical T_2 dephasing time of around 10 μs . It may therefore be possible to work at temperatures up to 3 K.

The coupling between an integrated waveguide and the erbium crystal should work in principle. Our first attempt to glue a fiber array onto the integrated couplers was unsuccessful as the glue crept during drying. This will be pursued further by repeating the gluing process. The end-fire approach might also be considered as a solution because the alignment is permanent and the coupling efficiency is better.

The next steps are to actually demonstrate coupling between the MW and the NIR regime. In order to demonstrate quantum conversion we need to be able to prepare a MW photon in an arbitrary quantum state and then be able to measure the converted NIR photon to proof the conservation of that state. A solution for the emission of the NIR photon needs to be implemented. One idea is to use an atomic frequency comb. Eventually, we would like to build an integrated quantum converter using the integrated optical waveguide and an additional layer on the chip containing a superconducting MW resonator. The difficulty is to get the same modal volume for the MW and the NIR fields in order to excite the same erbium atoms in the crystal.

It is quite possible that the intense international research interest on quantum computation bears fruit in the next couple of years and that some major breakthroughs allow the realization of the first real quantum computer. This field yields enormous potential and may well lead to a whole new generation of computation technology with unpredictable possibilities.

Bibliography

- [1] M. Antelius, K. B. Gylfason, and H. Sohlström, *An apodized SOI waveguide-to-fiber surface grating coupler for single lithography silicon photonics*, Optics Express **19** (2011), 3592.
- [2] Brassard G. Vazirani U. Bennett C.H., Bernstein E., *The strengths and weaknesses of quantum computation*, SIAM Journal on Computing **26** (1997), 1510–1523.
- [3] T. Böttger and C. W. Thiel et al., *Spectroscopy and dynamics of $Er^{3+}:Y_2SiO_5$ at 1.5 μm* , Physical Review B **74** (2006), 075107.
- [4] T. Böttger, C. W. Thiel, and R. L. Cone et al., *Effects of magnetic field orientation on optical decoherence in $Er^{3+}:Y_2SiO_5$* , Physical Review B **79** (2009), 115104.
- [5] T. Böttger, C. W. Thiel, Y. Sun, and R. L. Cone, *Optical decoherence and spectral diffusion at 1.5 μm in $Er^{3+}:Y_2SiO_5$ versus magnetic field, temperature, and Er^{3+} concentration*, Physical Review B **73** (2006), 075101.
- [6] Thomas Böttger, *Laser frequency stabilization to spectral hole burning frequency references in erbium-doped crystals: Material and device optimization*, Ph.D. thesis, Montana State University, 2002.
- [7] W. K. Burns and G. B. Hocker, *End fire coupling between optical fibers and diffused channel waveguides*, Applied Optics **16** (1977), 2048.
- [8] P. Bushev, A. K. Feofanov, and H. Rotzinger et al., *Ultralow-power spectroscopy of a rare-earth spin ensemble using a superconducting resonator*, Physical Review B **84** (2011), 060501(R).
- [9] Félix Bussières Nicolas Sangouard Mikael Afzelius Hugues de Riedmatten & Nicolas Gisin Christoph Clausen, Imam Usmani, *Quantum storage of photonic entanglement in a crystal*, Nature **469** (2011), 508–511.
- [10] Claude Cohen-Tannoudji, Bernard Diu, and Frank Laloe, *Quantum mechanics*, John Wiley & Sons, 1996.
- [11] M. L. Dakss, L. Kuhn, P. F. Heidrich, and B. A. Scott, *Grating coupler for efficient excitation of optical guided waves in thin films*, Applied Physics Letters **16** (1970), 523.
- [12] David P. DiVincenzo, *Quantum computation*, Science **270** (1995), 255–261.

- [13] Jeongwan Jin Joshua A. Slater Daniel Oblak Félix Bussières Mathew George Raimund Ricken Wolfgang Sohler & Wolfgang Tittel Erhan Saglamyurek, Neil Sinclair, *Broadband waveguide quantum memory for entangled photons*, Nature **469** (2011), 512–515.
- [14] J. L. Doualan et al., *Energy levels of the laser active Er^{3+} ion in each of the two crystallographic sites of yttrium orthosilicate*, Journal of Physics: Condensed Matter **7** (1995), 5111.
- [15] K. Hennessy et al., *Quantum nature of a strongly coupled single quantum dot-cavity system*, Nature **445** (2007), 896–899.
- [16] Lian-Wee Luo et al., *High quality factor etchless silicon photonic ring resonators*, Optics Express **19** (2011), 6284.
- [17] M.D. Dramicanin et al., *Synthesis of $Y_2SiO_5:Eu^{3+}$ nanoparticles from a hydrothermally prepared silica sol*, Journal of Alloys and Compounds **464** (2008), 357–360.
- [18] R. M. Macfarlane et al., *Measurement of photon echoes in $Er:Y_2SiO_5$ at $1.5 \mu m$ with a diode laser and an amplifier*, Optics Letters **22** (1997), 871.
- [19] T. Böttger et al., *Controlled compositional disorder in $Er^{3+}:Y_2SiO_5$ provides a wide-bandwidth spectral hole burning material at $1.5 \mu m$* , Physical Review B **77** (2008), 155125.
- [20] Richard Feynman, *Simulating physics with computers*, International Journal of Theoretical Physics **21** (1982), 467.
- [21] Nicolas Gisin and Rob Thew, *Quantum communication*, Nature Photonics **1** (2007), 165–171.
- [22] M. Gorodetsky and V. Ilchenko, *Optical microsphere resonators: optimal coupling to high- q whispering-gallery modes*, Journal of the optical society of America B - Optical physics **16** (1999), 147–154.
- [23] S. Hübner, *Optical spectra of transparent rare earth compounds*, Academic Press, 1978.
- [24] T. J. Kippenberg and K. J. Vahala, *Cavity opto-mechanics*, Optics Express **15** (2007), 17172.
- [25] H. A. Kramers, *Théorie générale de la rotation paramagnétique dans les cristaux*, Proc. Amsterdam Acad. **33** (1930), 959.
- [26] L. D. Landau and L. M. Lifshitz, *Quantum mechanics*, Elsevier LTD, Oxford, 1981.
- [27] M. D. Levenson and S. S. Kano, *Introduction to nonlinear laser spectroscopy*, Academic Press, New York, 1988.
- [28] G.K. Liu and R.L. Cone, *Energy transfer and instantaneous spectral diffusion processes in Tb^{3+} compounds as probed in photon echo experiments*, Journal of Luminescence **45** (1990), 387–391.
- [29] J.-M. Liu, *Photonic devices*, 1 ed., Cambridge Univ. Press, 2005.

- [30] Grover L.K., *From schrödinger's equation to quantum search algorithm*, American Journal of Physics **69** (2001), 769–777.
- [31] Daniel E.; Yang Tao & Pan Jian-Wei Lu, Chao-Yang; Browne, *Demonstration of a compiled version of shor's quantum factoring algorithm using photonic qubits*, Physical Review Letters **99** (2007), 250504.
- [32] S. Mahdi, M. Grehnand, A. Al-Saadi, M. Höfner, S. Meister, and H. J. Eichler, *Facet preparation of silicol nano-waveguides by cleaving the soi chip*, Journal of Nonlinear Optical Physics & Materials **20** (2011), 509–523.
- [33] Leonard Mandel and Emil Wolf, *Optical coherence and quantum optics*, Cambridge: Cambridge University Press, 1995.
- [34] A. B. Matsko, *Practical applications of microresonators in optics and photonics*, CRC Press, 2009.
- [35] Philip Krantz Martin Sandberg Michaël Simoen Pavel Bushev Nicolas Sangouard Mikael Afzelius Vitaly S Shumeiko Göran Johansson Matthias U Staudt, Io-Chun Hoi, *Coupling of an erbium spin ensemble to a superconducting resonator*, J. Phys. B: At. Mol. Opt. Phys. **45** (2012), 124019.
- [36] S. McNaban, N. Moll, and Y. Vlasov, *Ultra-low loss photonic integrated circuit with membranetype photonic crystal waveguides*, Optics Express **vol. 11** (2003), 2927.
- [37] S. E. Miller, *Coupled wave theory and waveguide applications*, vol. v33, Bell System Technical Journal, May 1954.
- [38] W. B. Mims, *Phase memory in electron spin echoes, lattice relaxation effects in CaWO₄: Er, ce, mn*, Physical Review **168** (1968), 370.
- [39] J. J. L. Morton, *Solid-state quantum memory using the 31p nuclear spin*, Nature **455** (2008), 1085–1088.
- [40] Michael Nielsen and Isaac Chuang, *Quantum computation and quantum information*, Cambridge: Cambridge University Press, 2000.
- [41] E. M. Purcell, *Spontaneous emission probabilities at radio frequencies*, Physical Review **69** (1946), 681+.
- [42] T. P. Purdy K. Cicak R. W. Simmonds C. A. Regal K. W. Lehnert R. W. Andrews, R. W. Peterson, *Reversible and efficient conversion between microwave and optical light*, arXiv:1310.5276, 2013.
- [43] D. G. Rabus, *Integrated ring resonators: the compendium*, Springer, 2007.
- [44] S. Wünsch P. Jung M. Jerger M. Siegel A. V. Ustinov S. Probst, H. Rotzinger and P. A. Bushev, *Anisotropic rare-earth spin ensemble strongly coupled to a superconducting resonator*, Physical Review Letters **110** (2013), 157001.
- [45] J. J. Sakurai, *Modern quantum mechanics*, Addison Wesley Pub Co Inc, 2010.
- [46] Bahaa E. A. Saleh and Malvin Carl Teich, *Fundamentals of photonics*, New York: John Wiley & Sons, 1991.
- [47] D. Scharid, *High efficiency input-output prism waveguide coupler: an analysis*, Applied Optics **18** (1979), 2921.

- [48] B. Schumacher, *Quantum coding*, Physical Review A **51** (1995), 2738–2747.
- [49] Y. Sun and T. Böttger et al., *Magnetic g tensors for the $^4I_{15/2}$ and $^4I_{13/2}$ states of $Er^{3+}:Y_2SiO_5$* , Physical Review B **77** (2008), 085124.
- [50] Orazio Svelto, *Principles of lasers*, Springer, 2010.
- [51] K. J. Vahala, *Optical microcavities*, Nature **424** (2003), 839–846.
- [52] Matthias; Breyta Gregory; Yannoni Costantino S.; Sherwood Mark H. & Chuang Isaac L. Vandersypen, Lieven M. K.; Steffen, *Experimental realization of shor’s quantum factoring algorithm using nuclear magnetic resonance*, Nature **414** (2001), 883–887.
- [53] Y. Yamamoto, F. Tassone, and H. Cao, *Semiconductor cavity quantum electrodynamics*, Springer, 2000.

Acknowledgments

At this point it is past time for me to list a number of people who's support in one way or another was crucial for this work. First I shall thank Professor Alexey Ustinov who allowed me to work on this topic by inviting me into his group in the first place. I imagine it is not always easy to teach and administer new students quite uninitiated to most concepts in today's research. Even more so when knowing that most will leave just when they have learned the basics. The task that falls to the second reviewer may in some ways be even more frustrating due to the lack of genuine involvement or benefit. Nonetheless, Professor Martin Wegener accepted it without hesitation.

Much of the credit for the success of this work must go to Professor Pavel Bushnev. His oversight, direction and support allowed me to concentrate on the task at hand without having to worry overly much on the next fifteen steps. Yet it is his humor and happy nature which makes working with him such a pleasure. I spent my first couple of months working on the integrated waveguide in Dr. Wolfram Pernice's group. Just as knowledgeable in his field as Pavel and quite the sympathetic person in his own right, he introduced me to the fabrication side and enabled me to work with seven hundred sixty-four different instruments and chemicals. I cannot quite imagine to have learned and seen more anywhere else this year than I did in these two groups.

In addition, I would like to express my gratitude towards several people who helped me time and again by introducing me to instruments, by walking me through some theory (you wouldn't believe how much I suddenly appreciated some of the theory lectures) or simply by having a good old fashioned discussion. Sebastian and Andrej, most notably among the people of Professor Ustinov's group, were always lending a hand, explaining stuff and ending any motivational lapses (they got pretty good at the latter, no thanks to the omnipresent news coverage on the web). In Wolfram's group Nico, Matze, Oli, Svetlana, Vadim, and most recently (with the fiber array, oh what a twiddle) Patrik got me started on the instruments and the design and simulation tools. Wladick, Martin and Tobi provided the (not so much needed as sought after) recreational moments by means of coffee break and lunch and coffee break and cake and, oh, did I mention the coffee break?

Naturally, there are tons of other people who helped me considerably, as well. I stand ashamed for not naming everyone, however, I have decided that I must now, at 11pm on a Sunday, go to bed soon (although I shall try to buy their high regards with cake & jokes, lest they think me a barbarian instead of, as I like to view myself,

a social superhero à la Oscar Wilde, possibly only comparable to one of the great victors of the ancient roman empire */sarcasm off*).

Last but not least, and most importantly, I will thank my family for perpetual love and support. To my friends I say let us continue the journey, may the next game commence!